

**BIOMIMETIC NANOREACTORS:  
AN INVESTIGATION OF CONFINED  
POLYMER-METAL NANOSYSTEMS**

**NANORÉACTEURS BIOMIMÉTIQUES:  
UNE ETUDE SUR DES NANOSYSTÈMES  
DE TYPE POLYMÈRE-MÉTAL FAVORISANT  
L'EFFET DE CONFINEMENT**

A Thesis Submitted to the Division of Graduate Studies  
of the Royal Military College of Canada by

Matthew Robert McTaggart, CD, BSc, rmc  
Lieutenant

In Partial Fulfillment of the Requirements for the Degree of  
Master of Science

August, 2015

© This paper may be used within the Department of National Defence but  
copyright for open publication remains the property of the author

Marco Polo describes a bridge, stone by stone.  
But which is the stone that supports the bridge?  
Kublai Khan asks.

The bridge is not supported by one stone or  
another, Marco answers, but by the line of the arch  
that they form.

Kublai Khan remains silent, reflecting. Then he  
adds: Why do you speak to me of the stones? It is  
only the arch that matters to me.

Polo answers: Without stones there is no arch.

— Italo Calvino *Invisible Cities*

## Acknowledgements

My sincere and lasting thanks to the many people whose help assisted in this research. Primarily I would like to acknowledge the efforts of Dr. Cecile Malardier-Jugroot. Her guidance and inspiration has been, and remains, invaluable. Thank you to Dr. Michael Groves and Dr. Manish Jugroot for instigating this work and for instructive early conversations. Thank you also to Ms. Xia Li for sharing her expertise and support, and to the other members of Dr. Malardier-Jugroot's research group Dr. Deborah Durbin and Ms. Vishva Shah for their valuable contributions.

I am grateful for funding support provided by Defence Research and Development Canada and the Natural Sciences and Engineering Research Council.

I would also like to acknowledge the excellent instrument support I received from Mr. Bob Whitehead and Dr. Jenn Snelgrove at the Royal Military College of Canada, Dr. Boualem Hammouda at the NIST Center for Neutron Research, and Dr. Andreas Korinek at the Canadian Centre for Electron Microscopy, McMaster University.

Thank you to Dale and Carolyn McTaggart for the wisdom that set me on this path and assured its completion. Finally, and with emphasis, thank you to Mrs. Danielle McTaggart for alleviating the numerous and inevitable difficulties of life, and to Eleanor and Moira for providing them.

## Abstract

Biomolecular reactors enable life-sustaining chemical processes through the complementary effects of catalysis and confinement. Innovations in polymer science and supramolecular chemistry have led to the discovery of materials that mimic these effects to increase reaction efficiency while simultaneously decreasing ecological impact. This was recently demonstrated using poly(styrene-alt-maleic anhydride)–platinum (SMA-Pt) nanoreactors that combine nanoscale hydrophobic domains with high surface area nanocrystals to initiate and catalyze an otherwise energetically unfavourable reaction in neutral water at room temperature and pressure.

This thesis marks a significant expansion of that initial finding. First, a new self-assembling morphology of SMA is characterized by quantum theoretical modeling coupled with transmission electron microscopy and small-angle neutron scattering. The polymer is shown to associate into highly organized bi-layer sheets through  $\pi$ - $\pi$  stacking between styrene groups of adjacent chains. The supramolecular structure houses a 2-3 nm hydrophobic inner cavity capable of producing the reactive environment that defines the confinement effect.

Second, the reductant-free decomposition of platinum and gold chloride salts into metal nanoparticles through interaction with the SMA template is described, including the first reported observation of stable atomically-thin gold nanoplates. The complete structural characterization of SMA-Pt, SMA-Au, and combined SMA-metal systems is established through electron microscopy, light and neutron scattering, and quantum theoretical methods. Platinum reduction is reproduced in poly(isobutylene-alt-maleic anhydride) to demonstrate the critical role of confinement to the reaction mechanism.

Lastly, further progress towards artificial nanoreactors with activity comparable to their biological counterparts will require the ability to predict outcomes of confined reactions. The outline of a theory is advanced that is consistent with existing evidence and suggests a new approach incorporating thermodynamics. Their facile synthetic method, environmentally friendly reaction conditions, and structural stability make biomimetic nanoreactors a fundamental advancement in science and technology applications from detoxification to nanoelectronics, medicine, and sustainable energy.

## Résumé

Les réacteurs biomoléculaires favorisent des procédés chimiques permettant le maintien de la vie à travers les effets complémentaires de la catalyse et du confinement. Des innovations dans la science des polymères et la chimie supramoléculaire ont conduit à la découverte de matériaux qui imitent ces effets pour accroître l'efficacité de réactions tout en diminuant simultanément leur impact écologique. Cela a été récemment démontré en utilisant des nanoreacteurs composés du polymère poly(styrène-*alt*-maléique anhydride) et de nanoagrégats de platine (SMA-Pt) qui combinent des domaines hydrophobes nanométriques avec des nanocristaux ayant une grande surface de contact afin d'initier et de catalyser une réaction énergétiquement défavorable dans l'eau neutre à température et pression ambiante.

Cette thèse décrit une étude approfondie de cette constatation initiale. Tout d'abord, une nouvelle morphologie de l'auto-assemblage de SMA est caractérisée par la modélisation théorique quantique couplée avec la microscopie électronique à transmission ainsi que la diffraction de neutrons aux petits angles. Les chaînes de polymère s'associent en feuillets bi-couche hautement organisés grâce à des interactions  $\pi$ - $\pi$  entre les groupements styrène de chaînes adjacentes. La structure supramoléculaire abrite une cavité interne hydrophobe de 3.2 nm capable de produire l'environnement réactif qui promeut l'effet de confinement.

D'autre part, la décomposition, sans agent réducteur, de sels de chlorure de platine et de d'or en nanoparticules métalliques à travers l'interaction avec la nanostructure de SMA est décrite, y compris la première observation rapportée de nanoplaques d'or atomiquement minces et stables. La caractérisation structurale complète de SMA-Pt, SMA-Au, et des systèmes combinés SMA-métal est établie par microscopie électronique, diffusion de rayons-X et de neutrons, et des méthodes théoriques quantiques. La réduction du Platine reproduite dans le poly (isobutylène-*alt*-maléique anhydride) a démontré le rôle critique du confinement pour le mécanisme de réactionnel.

De plus, une meilleure compréhension des nanoréacteurs artificiels ayant une activité comparable à leurs homologues biologiques exigera la capacité de prédire les réactions en milieu confiné. L'esquisse d'une théorie est avancée qui est compatible avec les preuves expérimentales existantes et suggère une nouvelle approche incluant la thermodynamique. La combinaison d'une méthode synthétique facile, de conditions de réaction respectueuses de l'environnement, ainsi que de la stabilité structurale font de ces nanoréacteurs biomimétiques un progrès fondamental dans des applications scientifiques et technologiques allant de la désintoxication à la nanoélectronique, de la médecine et à l'énergie durable.

# Table of Contents

<b>Acknowledgements</b> .....	<b>iii</b>
<b>Abstract</b> .....	<b>iv</b>
<b>Résumé</b> .....	<b>v</b>
<b>List of Tables</b> .....	<b>viii</b>
<b>List of Figures</b> .....	<b>ix</b>
<b>1 Biomimetic nanomaterials</b> .....	<b>12</b>
1.1 Introduction .....	12
1.2 Structures from 100-1000nm .....	13
1.3 Structures from 10-100nm.....	17
1.4 Structures from 1-10nm.....	24
1.5 Objectives .....	35
<b>2 Methods</b> .....	<b>37</b>
2.1 Quantum Theoretical Methods.....	37
2.1.1 Survey of Quantum Methods .....	37
2.1.2 Wavefunction Approximations .....	39
2.1.3 Hartree-Fock Theory .....	42
2.1.4 Density Functional Theory .....	44
2.1.5 Methods used in this study.....	48
2.1.6 Conclusion and outlook .....	51
2.2 Ultraviolet/visible light spectroscopy .....	51
2.2.1 UV/vis spectroscopy theory.....	51
2.2.2 Surface plasmon resonance.....	52
2.3 Small Angle Neutron Scattering .....	52
2.3.1 Neutron v. photon spectroscopy .....	53
2.3.2 Operation of the NIST CNR spectrometer.....	54
2.3.3 Neutron scattering theory .....	55

2.3.4	Data reduction and analysis .....	57
2.4	Electron microscopy.....	59
2.4.1	Scanning electron microscopy (SEM).....	59
2.4.2	Transmission electron microscopy .....	60
<b>3</b>	<b>The SMA polymer template .....</b>	<b>63</b>
3.1	Introduction .....	63
3.2	Experimental.....	64
3.3	Results and Discussion.....	65
3.4	Conclusion.....	72
<b>4</b>	<b>Noble metal active centres.....</b>	<b>73</b>
4.1	Introduction .....	73
4.2	Experimental.....	73
4.3	Results and Discussion.....	74
4.3.1	Platinum .....	74
4.3.2	Gold.....	84
4.3.3	Platinum-gold combined system.....	92
4.3.4	IMA.....	95
4.4	Conclusion.....	100
<b>5</b>	<b>Implications for Theory .....</b>	<b>102</b>
5.1	Confined water dynamics.....	102
5.2	The mechanism of confinement.....	104
5.3	Confinement thermodynamics.....	107
5.4	Application to experiment.....	110
5.5	Conclusion.....	111
<b>6</b>	<b>Conclusion and outlook.....</b>	<b>112</b>
<b>7</b>	<b>Consolidated references.....</b>	<b>114</b>

## List of Tables

<b>Table 1.</b> Neutron scattering length density for materials used in this study.....	57
<b>Table 2.</b> SANS model fitting parameters. ....	67
<b>Table 3:</b> Experimental samples for central composite design. ....	78
<b>Table 4.</b> SANS model fitting parameters for gold-SMA system in D <sub>2</sub> O.....	82
<b>Table 5.</b> EDAX elemental analysis of Gold-SMA thin film .....	86



## List of Figures

<b>Fig. 1</b>	Viability of PC-12 cells cultured on polypyrrole films .....	14
<b>Fig. 2</b>	Images of PC-12 cell growth on polypyrrole-coated poly(lactic-co-glycolic acid) fibres.....	15
<b>Fig. 3</b>	Responsive polymer gating materials .....	16
<b>Fig. 4</b>	Chemically etched nanochannel modified with GO <sub>x</sub> and HRP.....	18
<b>Fig. 5</b>	<b>a)</b> Dose response of bare and functionalized nanochannels. <b>b)</b> Selectivity analysis for glucose response.....	19
<b>Fig. 6</b>	Kinetics of PalB encapsulation. ....	21
<b>Fig. 7</b>	The chemoluminescent (CL) emission spectra of the 0.025 mm luminol and 0.0375 mm Hb .....	22
<b>Fig. 8</b>	Schematics of <b>a)</b> natural and <b>b)</b> artificial photocatalysis .....	23
<b>Fig. 9</b>	Schematics of <b>a)</b> natural photosynthesis in photosystem I and <b>b)</b> biomimetic photosynthesis.....	24
<b>Fig. 10</b>	Simplified reaction profiles of a reaction.....	26
<b>Fig. 11</b>	Illustration of $\beta$ -Ga <sub>2</sub> O <sub>3</sub> growth mechanism .....	28
<b>Fig. 12</b>	Formation of 1,2-dihydropyridine from pyridine .....	29
<b>Fig. 13</b>	Conversion of CO <sub>2</sub> to CH <sub>3</sub> OH and H <sub>2</sub> O by PyH <sub>2</sub> .....	30
<b>Fig. 14</b>	The pH sensitivity of poly(styrene-alt-maleic acid) .....	31
<b>Fig. 15</b>	SMA chain linearity, and therefore its self-assembly, is pH dependent due to internal hydrogen bonding.....	32
<b>Fig. 16</b>	HR-TEM image of platinum nanocrystals synthesized in the SMA supramolecular nanostructure.....	34
<b>Fig. 17</b>	Pyrrole polymerization in solution with SMA (left) and Platinum-SMA (right) nanostructures. ....	35
<b>Fig. 18</b>	Because they form a cusp at $r = 0$ and trend to 0 as $r \rightarrow \infty$ , Slater-type orbitals (STO) accurately describe atomic orbitals. Gaussian-type orbitals (GTO) better approximate STOs as the number of primitive Gaussians $n$ increases.....	41
<b>Fig. 19</b>	A surjective function $f$ maps at least one element of $X$ to every element of $Y$ ; an injective function $g$ maps at most one element of $X$ to a unique $Y$ ; a function $h$ that is both surjective and injective maps one and only one element of $X$ to each and every element of $Y$ . ....	46
<b>Fig. 20</b>	Representation of x-ray v. neutron scattering cross-sections.....	54
<b>Fig. 21</b>	A schematic representation of the relationships described in Equations 2.3.4 through 2.3.6. ....	56
<b>Fig. 22</b>	Schematic of elliptical shapes that could produce a SANS spectra described by Equation 2.3.8. ....	58

<b>Fig. 23</b>	Map of electron diffraction points of the (111) crystal plane. ....	62
<b>Fig. 24</b>	Map of Miller indexed electron diffraction points for hexagonal close packed crystal structure. ....	62
<b>Fig. 25</b>	Crystalline lamella model (line) fitted to SANS data of 1% SMA. ....	66
<b>Fig. 26</b>	Close up of TEM image, SMA-Pt system at pH 7 showing SMA supramolecular association into a bi-layer nanosheet .....	68
<b>Fig. 27</b>	TEM image of SMA-Pt system showing Pt nanocluster confinement to SMA sheets and their top-level organization. ....	69
<b>Fig. 28</b>	Bi-layer model of SMA. ....	71
<b>Fig. 29</b>	Schematic representation of the unsupported polymeric nanoreactor in aqueous environment. ....	72
<b>Fig. 30</b>	UV/vis spectra of PtCl <sub>2</sub> in 1%wt SMA solution. ....	75
<b>Fig. 31</b>	Dissociation of chlorine from platinum. ....	76
<b>Fig. 32</b>	Optimized molecular simulation of a platinum atom bonding to the styrene ring of a SMA trimer. ....	76
<b>Fig. 33</b>	HR-TEM images of SMA-Pt systems prepared at pH levels shown. ....	79
<b>Fig. 34</b>	Diameter distribution of platinum nanoparticles. ....	80
<b>Fig. 35</b>	Diameter distribution of all platinum nanoparticles measured. ....	80
<b>Fig. 36</b>	Truncated cubic progressing to cuboctahedral solids. ....	81
<b>Fig. 37</b>	Lamella-ellipsis fit (line) to SANS data of PtCl <sub>2</sub> in 1% SMA. ....	83
<b>Fig. 38</b>	UV/vis spectra of AuCl in 1% SMA solution. ....	84
<b>Fig. 39</b>	Optimized ONIOM model of a gold atom co-ordinated to the oxygen- rich maleic acid group of SMA. ....	85
<b>Fig. 40</b>	2.6 μm <sup>2</sup> gold monolayer. ....	88
<b>Fig. 41</b>	SAED consistent with hexagonal close-packing crystal structure. ....	89
<b>Fig. 42</b>	Two discrete gold nanosheets producing a 1 nm Moiré fringe pattern by their overlap. ....	90
<b>Fig. 43</b>	SEM image of 500nm gold crystal. ....	91
<b>Fig. 44</b>	Lamella-ellipsis model fitted to SANS data of AuCl in 1% SMA. ....	92
<b>Fig. 45</b>	UV/vis spectra of AuCl and PtCl <sub>2</sub> mixed in SMA by method 1. ....	93
<b>Fig. 46</b>	UV/vis spectra of AuCl and PtCl <sub>2</sub> mixed by method 2. ....	94
<b>Fig. 47</b>	Schematic of IMA and its response to changes in solution pH. ....	95
<b>Fig. 48</b>	Simulation of the alignment of two IMA chains. ....	96
<b>Fig. 49</b>	UV/vis spectra of platinum reduction in IMA .....	97
<b>Fig. 50</b>	HR-TEM image of platinum nanocrystals in poly(isobutylene-alt-maleic acid) superstructure. ....	98
<b>Fig. 51</b>	Fast fourier transform of Figure 52. ....	100
<b>Fig. 52</b>	HR-TEM image of platinum nanocrystals synthesized in 1% IMA. ....	99

<b>Fig. 53</b>	Water translational dynamics.....	103
<b>Fig. 54</b>	The probability of finding a water molecule.....	104
<b>Fig. 55</b>	Schematic representation of a) water molecules in a confined hydrophobic space b) formation of the vapour tube joining the surfaces and nucleating c) complete drying..	105
<b>Fig. 56</b>	Diffusion on a flat surface vs. diffusion on a curved surface. ....	108
<b>Fig. 57</b>	Initially parallel paths remain parallel on a flat surface but converge on a curved surface.....	109
<b>Fig. 58</b>	The presence of an immobilized ion affects the compression of nearby non-polar polymers.....	111

# 1 Biomimetic nanomaterials

Portions of this section were originally published as: McTaggart, M., Jugroot, M., Malardier-Jugroot, C. (2015) Biomimetic soft polymer nanomaterials for efficient chemical processes. In Basiuk, V.A. and Basiuk, E.V. (Eds.) *Green Processes for Nanotechnology* (pp. 277-301). Springer International Publishing.

*M.R.M. completed the literature review and prepared the manuscript*

## 1.1 Introduction

Nearly every biological process depends on soft, self-assembling nanostructures that sense or alter the local environment to ensure efficient and selective action. Living organisms routinely produce highly structured macromolecules to accomplish functions that humanity performs through industry: energy collection, fuel production and storage, material transport, and detoxification of waste products among them<sup>1</sup>. Soft matter in nature, ranging from tissues through cellular membranes to proteins, is therefore an obvious source of inspiration for addressing the technological challenges that arise as we seek to improve the efficiency of industrial processes. Although the effectiveness of natural materials has long been recognized, it is only in recent decades that we have developed the methods needed to measure their structure and dynamics or indeed to begin to reproduce them synthetically<sup>2</sup>. Biomimicry, whether by adapting natural molecules to new purposes or by recreating the chemical and physical properties of biological systems in new materials, is an emerging area in material science<sup>3</sup>. Biomimetic soft materials represent a fundamental advancement in fields as far reaching as medicine, energy, and chemical catalysis towards efficient and environmentally-friendly processes.

Because of their simple synthesis, low cost, tunable mechanical properties, and generally inert reactivity, polymers are ubiquitous as macroscopic structures, but lately new nanoscale structural and functional properties have been discovered<sup>4</sup>. Conductive polymers permit electrochemical processes to occur in disperse networks free from metals<sup>5</sup>, both important considerations for maximizing efficiency and minimizing toxicity<sup>6</sup>. Copolymer arrangements of charged, hydrophobic, or hydrogen-bonding monomers interact in solution to produce specific effects similar to those of proteins – complex natural polymers of amino acids. Like their biological counterparts, the conformation of synthetic polymers containing surface active groups can be very sensitive to changes in the physical environment<sup>7</sup>. Polymers can be finely tuned to adsorb or shed solvent molecules through changes in temperature or light, to alter electrostatic bonds by changes to ionic strength, and to change conformation of

weak acid or base containing polymers in relation to pH<sup>8</sup>. Both naturally occurring and synthetic soft nanomaterials can produce very precise nanoarchitectures through the self-assembly of small molecules<sup>9</sup>. Amphiphilic surfactants may be similarly used to build micelles of varying shapes from tens to hundreds of nanometers in radius through a process that mimics self-assembly of the lipid bi-layer that composes cellular membranes<sup>10</sup>.

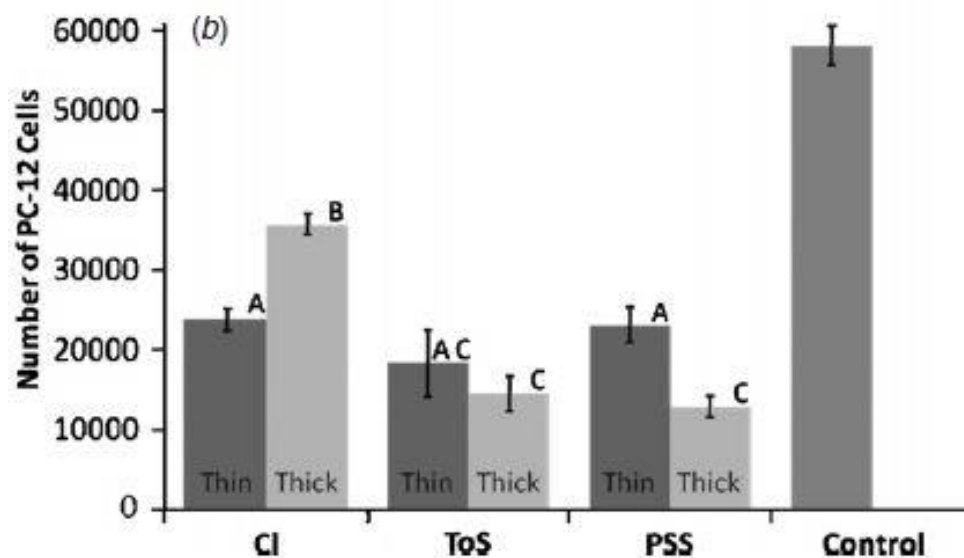
It is obvious to say but bears mentioning that the size of individual components, as well as their proportional contributions, becomes increasingly important as the size of the system decreases. At the microscale, materials in applications such as tissue scaffolding and sensing actuators may express dramatic statistical effects on the performance of the system by the random inclusion of a small percentage of functional polymer fibres. Systems in the 10-100 nanometer size regime, such as selective membranes and encapsulating reaction vessels, contain highly organized functional elements and have precisely determined functions. With dimensions less than 10 nanometers, self-assembling materials composed of single molecules or supramolecular structures can produce emergent properties that mimic functional proteins or enzymes. This review will survey applications in each of these three size regimes to illustrate the advantages of using soft nanomaterials to sense and alter their local chemical and physical environment to improve the efficiency and sustainability of processes.

## **1.2 Structures from 100-1000nm**

Nanostructured materials near the micrometer range are able to influence or respond to environmental conditions such as temperature, pH, light, and electrical stimulation. The specific mechanical and electrical response of polymer-based materials in this regime can be tailored according to application.

### **1.2.1 Tissue engineering**

Inherently conductive polymers have been subject to intense study in recent decades for application in microelectronics, optics, and fuel cells among others. Given the crowded and conductive nature of the extracellular matrix (ECM) in living organisms, conductive polymers were tested as a scaffold for tissue regeneration and engineering<sup>11</sup>. In addition to conduction, in vivo applications have specific toxicity, inflammatory, and mechanical demands that must be met. Due to its high conductivity, polypyrrole is of particular interest although poor solubility, degradability, and elasticity limit its usefulness.

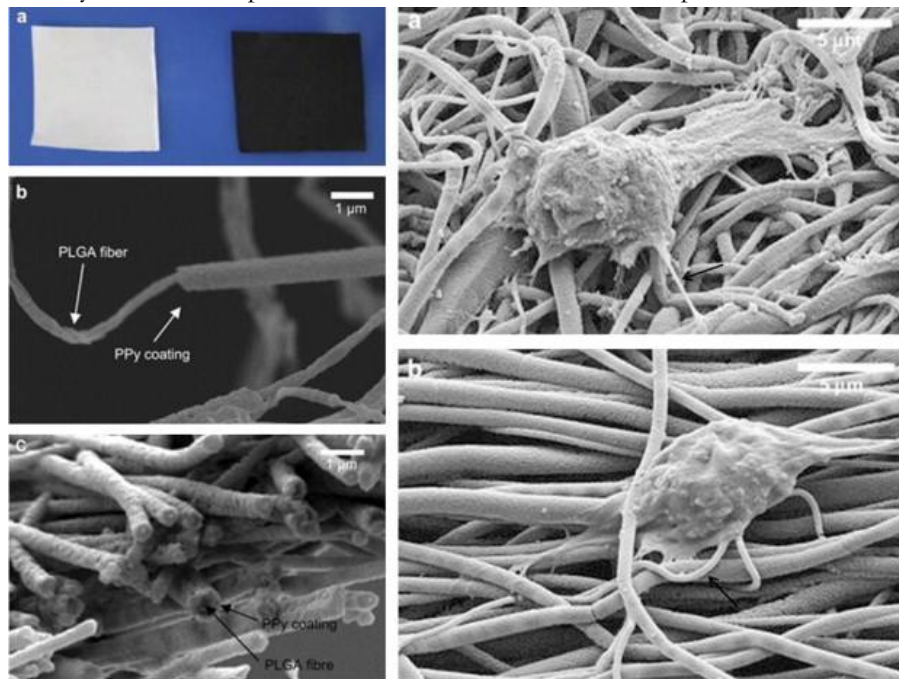


**Fig. 1** Viability of PC-12 cells cultured on polypyrrole films of 150 nm (thin) and 650 nm (thick) using three different counter ion dopants. The A, B, and C labels mark distinct significant values ( $p < 0.05$ ); bars labelled by the same letter are not significantly different. (Reproduced from Ref. 12)

Fonner *et al.* examined the effect of polypyrrole's synthesis method on its morphology, conduction, and suitability for medical implant<sup>12</sup>. They found that surface roughness and choice of counter ion play important roles in cell adhesion and long-term viability; changing the dopant allows the material to be altered to suit the application. For example, tosylate (ToS) produces a more conductive polymer than doping with chloride (Cl) or polystyrene sulfonate (PSS) and so is better suited for electrochemical coatings. PSS treated polypyrrole films are more stable in aqueous environments making it the preferred choice for long-term *in vivo* implantation. Enhanced surface roughness improved cell viability on thicker chloride counter ion films than on thin films due to, as presented in Figure 1.

By coating a polymer exhibiting more desirable mechanical properties with polypyrrole researchers have improved cell development and adhesion to tissue engineering scaffolds. Polypyrrole-poly lactide blends from 5-10% have been used for electrical stimulation-enhanced tissue regeneration, the results of which are shown in Figure 2<sup>13</sup>. Cell size, adhesion, viability, and cytokine release were all improved in the presence of mild electrical stimulation. Because of its non-degradability *in vivo*, it is preferable to minimize the amount of polypyrrole per supporting polymer structure.

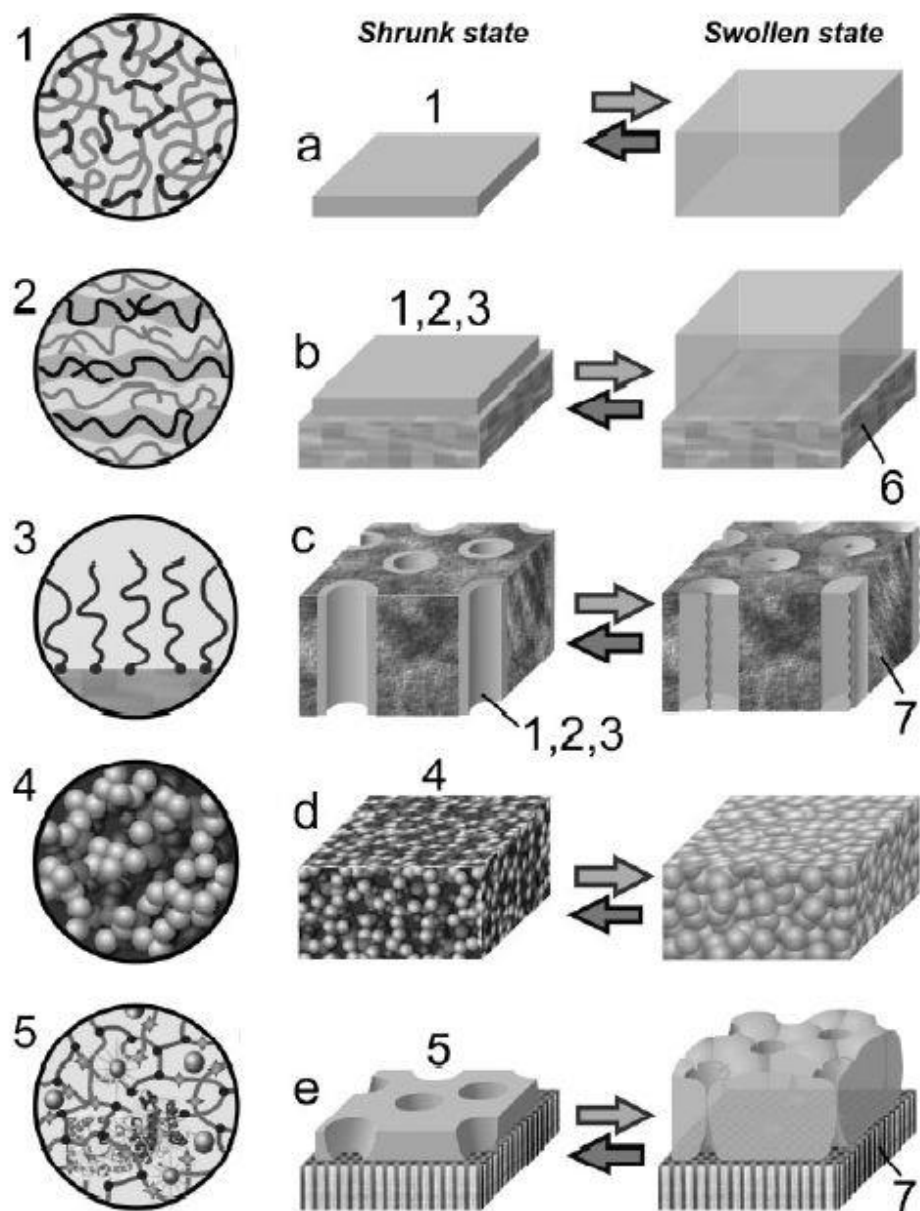
Fibres containing as little as a 1:39 ratio of polypyrrole to chitosan were found to sufficiently maintain the positive mechanical and conductive aspects of each.



**Fig. 2** Images of PC-12 cell growth on polypyrrole-coated poly(lactic-co-glycolic acid) fibres. A potential of 10mV/cm stimulated increased neurite formation and length by 40-90% and 40-50% respectively (neurites indicated by black arrows). Fibre alignment (**b**, lower right) also improved these factors over a random mesh (**a**, upper right). (Reproduced from Ref. 13)

### 1.2.2 Sensing membranes

Reactive polymers can sense changes in their environment such as pH, temperature, and ionic concentration<sup>14</sup>. Figure 3 shows examples of thin films of responsive polyelectrolyte hydrogels. Light or thermoresponsive polymer can be produced by tuning its relationship with its solvent so that its conformation changes in response to transition through the critical solution temperature<sup>15</sup>. As the polymer's relative affinity to itself and its solvent changes, solvent molecules will be either drawn into the polymer matrix or expelled from it. The volume and permeability of the matrix will change accordingly. The rate of responsiveness is limited by diffusion so thin layer depositions are ideal.



**Fig. 3** Responsive polymer gating materials: a) self-standing bulk gel film, b) surface-attached planar thin film, c) thin film immobilized on the walls of a porous substrate, d) self-standing composite film with inclusions of stimuli-sensitive polymer, and e) thin-film gel membrane on top of a porous substrate. (Reproduced from Ref. 8)



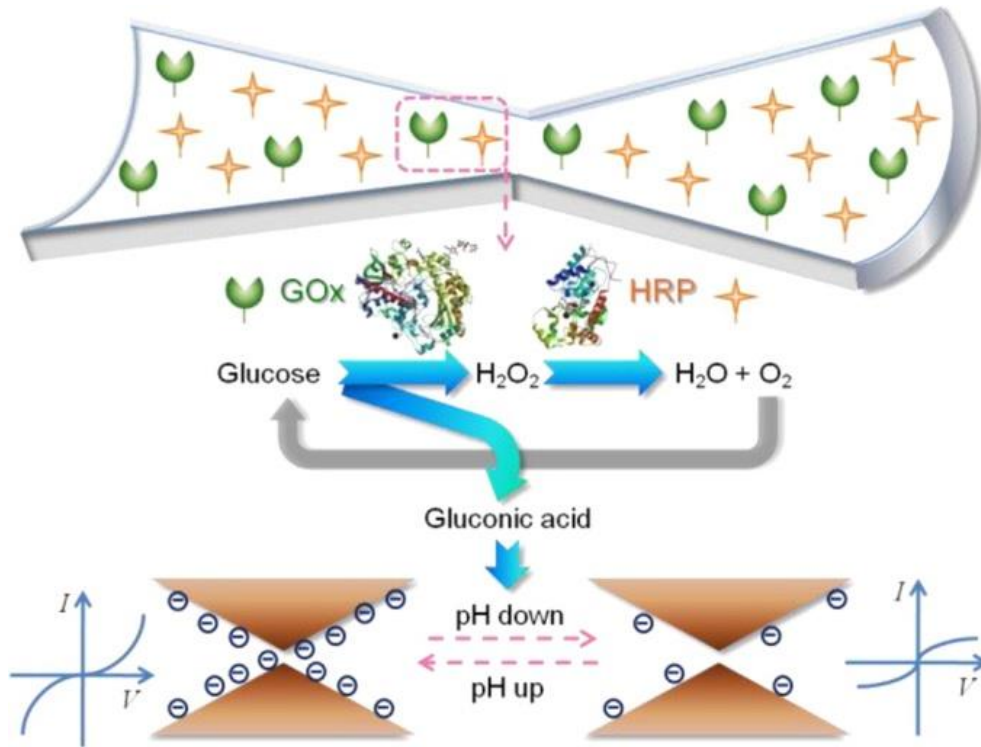
Similarly, polymer affinity for a specific solute can produce a measurable response in the material and act as a reusable sensor for that molecule. An example of this is a 200 nm electropolymerized m-acrylamidophenyl-boronic acid with acrylamide reported by Gabai *et al.*<sup>16</sup>. The film acts as an ion gate governed by the presence of glucose: boronic acid sites will bond preferentially to glucose and swell the polymer matrix, increasing permeability to a redox couple that is readily measured. The selectivity of sensing and switching mechanisms near the microscale suffers due to the random nature of its matrix. As permeability increases in the above sample, more and more varied chemical species are able to traverse the membrane. In addition, glucose may not be the only molecule, nor indeed the only sugar, capable of bonding to boronic acid, leaving open the possibility for false positives or mismanagement of cross-membrane exchange.

### **1.3 Structures from 10-100 nm**

As in nature, polymer or amphiphilic monomer membranes can enclose a volume and isolate it from interaction with bulk solvent<sup>17</sup>. Membranes of cells and cellular organelles perform this function and incorporate selective and responsive pores in the membrane to precisely control traffic into and out of the enclosed space. If a catalytic centre is included in the membrane or enclosed within it, the reactions it promotes will be enhanced by confinement. In fact, confinement can be a determining factor for reaction energetics and major products depending on the size of the system under study. Integration into a membrane, whether enclosed or porous, can also enhance the rate of multi-step reactions by coordinating the placement of catalysts, co-factors, and substrates.

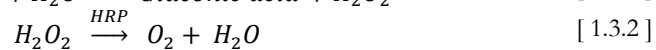
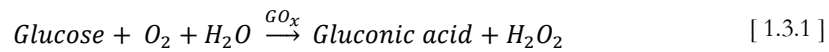
#### **1.3.1 Selective membranes**

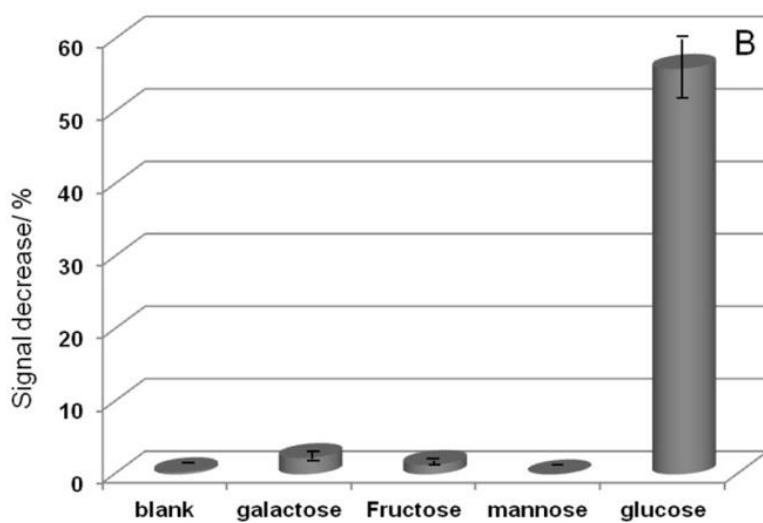
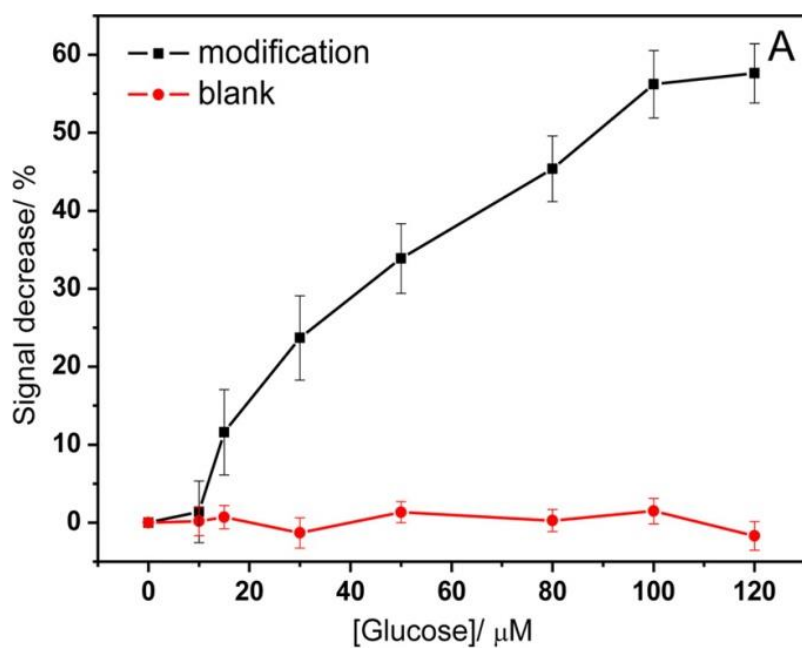
Membranes enclosing nanoscale volumes can control the flow of solutes by the inclusion of pores. Active and passive gate proteins in the cellular membrane are critical for the functioning of biological processes by ensuring the appropriate concentration balance of ions and reaction substrates in and outside of the cell. Unlike the sensing membranes described above, the membranes themselves remain impermeable but selective gates at nanopores selectively control solute exchange in response to environmental conditions.



**Fig. 4** Chemically etched double-conical nanochannel modified with GOx and HRP. Presence of glucose in the test produced gluconic acid and  $H_2O_2$  by GOx catalysis;  $H_2O_2$  was then decomposed into  $H_2O$  and  $O_2$  by HRP. Accumulation of gluconic acid decreased channel pH and negative charge density leading to a current decline. (Reproduced from Ref. 18)

Lin *et al.* describe a method for monitoring glucose according to ion current through an enzyme decorated nanochannel<sup>18</sup> (Fig. 4). Ion track etching was used to produce a 20 nm hourglass-shaped channel in a 12  $\mu\text{m}$  polyimide membrane. Using NaOCl as the chemical etching agent produces carboxyl groups along the channel whose negative charges maintain the channel aperture and create high cation selectivity. Functionalizing the channel with glucose oxidase (GOx) and horseradish peroxidase (HRP) produces the following reaction to the presence of glucose:





**Fig. 5** a) Dose response of bare and functionalized nanochannels. Monitored signal produced by ion flow through the membrane; decrease indicates nanochannels closing. b) Selectivity analysis for glucose response. The galactose, fructose, and mannose molarity were 1 mM each; the strongly selective glucose response was achieved with only 0.1 mM. (Reproduced from Ref. 18)

The reduction of pH in the channel produced by the local concentration of gluconic acid neutralizes the carboxyl groups, narrowing the channel and reducing its cation affinity in proportion to the amount of glucose present. Therefore the diameter of the channel opening depends on the local pH which, in turn, depends on the concentration of glucose. Since the glucose oxidase enzyme is known to be highly selective for glucose, as demonstrated in Fig. 5b, the current produced by the movement of ions through the channel cation passage serves as an equally selective glucose sensor.

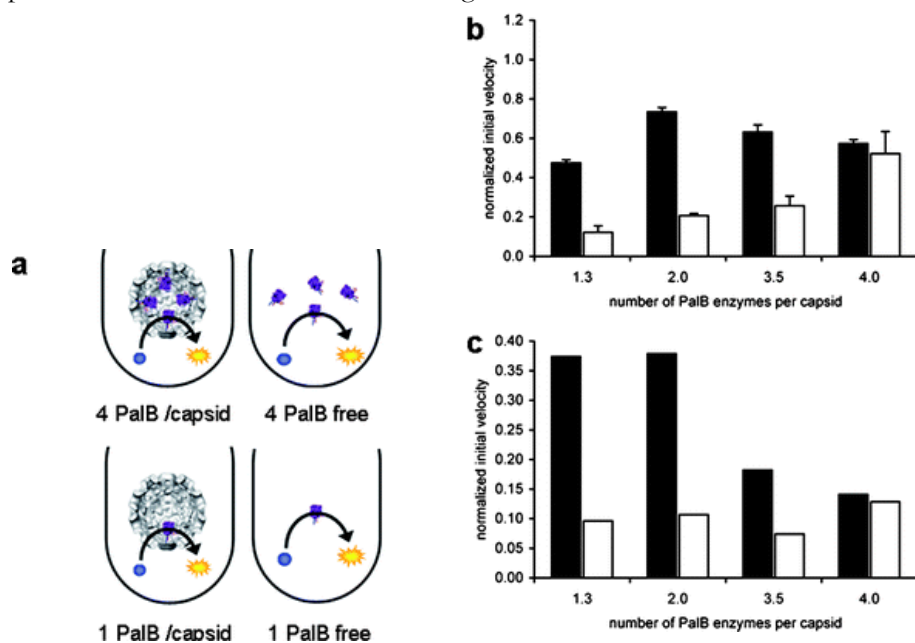
### 1.3.2 Vesicle-like confinement

Reaction sites within a cell are located in crowded, confined spaces. Confinement in a small volume improves the reaction rates and efficiency of catalyzed reactions by restricting diffusion, reducing rotational and translational energy loss, and increasing the effective molarity of the catalyst's local environment.

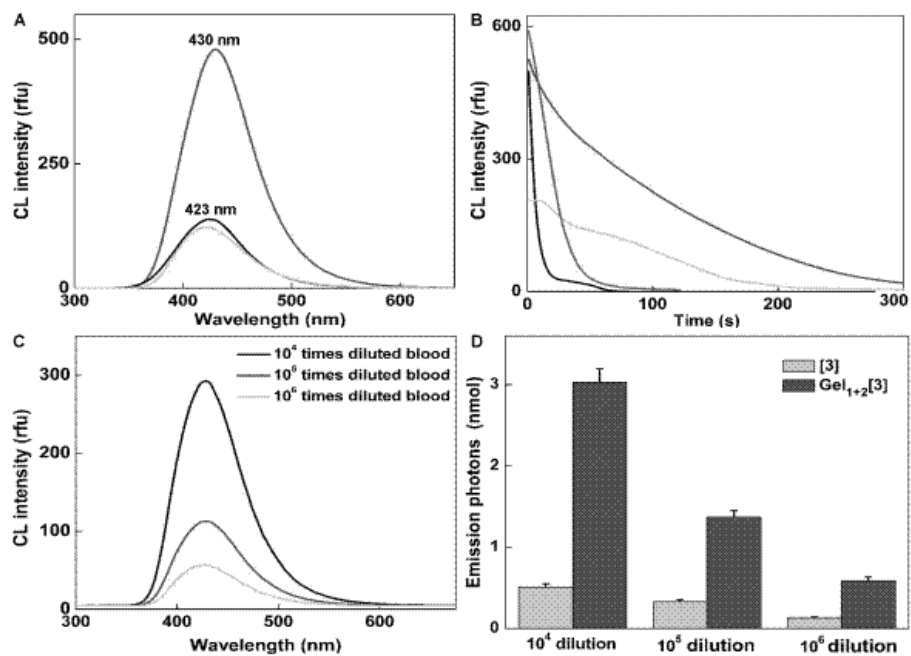
Minten and co-workers used the capsid of the Cowpea Chlorotic Mottle Virus (CCMV) to encapsulate enzymes and investigate the role of confinement on enzyme reaction rates<sup>19</sup>. The CCMV capsid comprises 180 identical proteins which separate into 90 dimers at pH 7.5 and self-assemble when returned to pH 5. This reversible association permits the simple removal of viral RNA and its replacement with a molecule of interest, in this case the acid-tolerant enzyme PalB. Figure 6 shows the results from testing enzymatic catalysis in saturating substrate concentrations and demonstrates that the encapsulated enzymes outperform their unconfined counterparts. Furthermore, the molarity within confinement spaces containing a single substrate molecule was increased by a factor of  $10^4$  and enzyme concentration was effectively 25 times greater than the bulk. Consequently, the likelihood of finding more than one substrate molecule within a given capsid was negligibly low, removing any advantage of including more than one enzyme in the confinement space. Minten did, however, show that different enzymes could be encapsulated in a single capsid, opening the potential for highly co-ordinated cascade reactions.

The effect of confinement can also be significant on the sensitivity and efficiency of physical processes like photon emission. Chemoluminescence is used for many analytical applications due to its high sensitivity to dilute samples. Luminol fluoresces in the presence of hemoglobin but generally achieves no better than 1% quantum yield in solution. The quantum yield of bioluminescent systems, alternately, is much higher: 88% of the light-generating reactions in fireflies are reported to successfully produce photon emission. Wang *et al.* were able to significantly increase the quantum yield of luminol reactions while extending their half-life by mimicking the intercellular environment with supramolecular hydrogels<sup>20</sup> (Fig. 7). For example, the quantum yield of the light producing reaction of 9-fluoroethylmethyl carbamate peptides mixed with

luminol and met-hemoglobin in water was 11.22%, a significant increase from a yield of 1.02% without the hydrogel. Likewise, emission time and intensity were raised by 4-6 times with hydrogel in solution over water alone. Confinement within the hydrogel reduces diffusion and rotation, thereby minimizing radiationless decay to increase reaction efficiency. The biomimetic environment produced by the polymeric gel also increased sensitivity of a  $10^6$  diluted hemoglobin solution to match the response from a solution two orders of magnitude more concentrated.



**Fig. 6** Kinetics of PalB encapsulation. The capsid concentration is the same in all encapsulated samples. **a)** Schematic representation of the experimental setup. **b)** Normalized initial reaction rates with respect to 1.3 PalB/capsid experiment. Black bars represent initial rates of samples with encapsulated PalB, white bars indicate the rate for free PalB. **c)** Normalized initial rates per PalB divided by the enzyme concentration, indicating the linearity of free PalB activity and the detrimental effect of crowding where multiple enzymes are inserted into a single capsid. (Reproduced from Ref. 19)



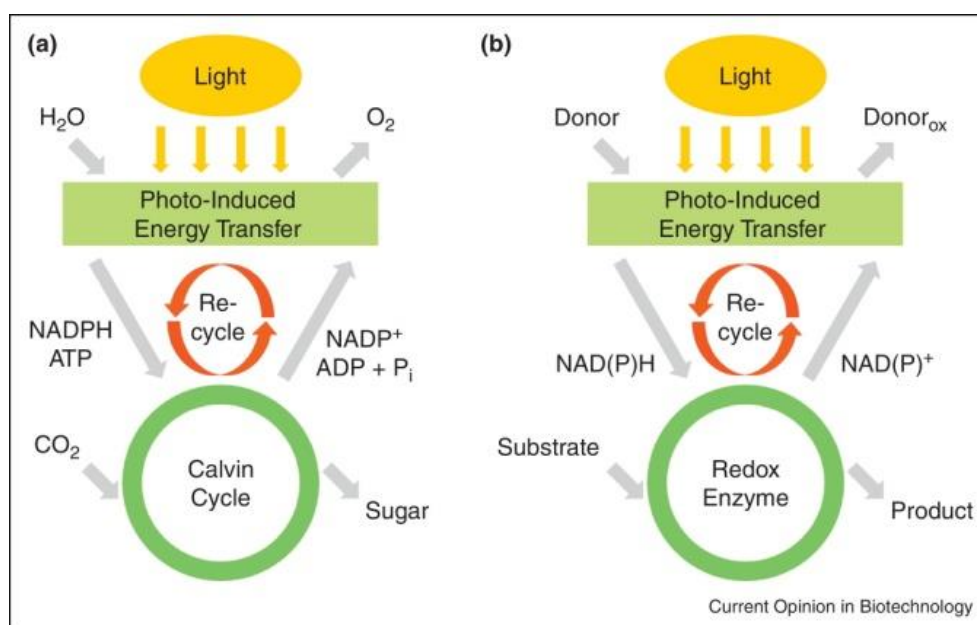
**Fig. 7** **a)** The chemoluminescent (CL) emission spectra of 0.025 mM luminol and 0.0375  $\mu$ M hemoglobin in the supramolecular hydrogel (at 430 nm) or solution initiated by adding 0.25 mM  $\text{H}_2\text{O}_2$  (at 423 nm); **b)** the time-dependant CL intensity curve of confined (low slope) and non-confined (high slope) solutions; **c)** the CL emission spectra catalyzed by rabbit blood at  $10^4$ ,  $10^5$ , and  $10^6$  dilution in descending intensity; **d)** the numbers of photons emitted from the CL reactions of luminol in hydrogel (dark grey) or in solution (light grey) with  $\text{H}_2\text{O}_2$  catalyzed by blood at dilutions from an initial hemoglobin concentration of  $11.9 \text{ mg}\cdot\text{mL}^{-1}$  (Reproduced from Ref. 20)

### 1.3.3 Multi-step reactions

Both photosynthesis and glucose metabolism depend on the proximity and separation of the cellular membrane. Synthetic analogues of these cellular processes can also benefit from compartmentalization across solid state nanostructures<sup>21</sup>.

Photocatalytic water splitting is an attempt to mimic hydrogenases, chiefly those of photosystem II, that employ visible light to drive the separation of protons from a donor species, ideally water<sup>22</sup>. PSII is a complex of protein subunits, co-factors, and electron donor and mediator molecules all operating in concert to achieve near quantum efficiency of photon capture. Natural photosynthesis incorporates light harvesting, charge stabilization, co-factor reduction, and the accumulation of oxidation equivalents for use by the oxygen evolving complex (water oxidizing complex). It is sufficiently complicated that in spite of intense research efforts the

exact structure and mechanism of key active areas remain hotly debated<sup>23</sup>; however, artificial systems may be able to model the critical aspects, as illustrated by Figure 8. As with their biomolecular counterparts, artificial photocatalysts use the energy captured from light to excite electrons for reduction-oxidation reactions.



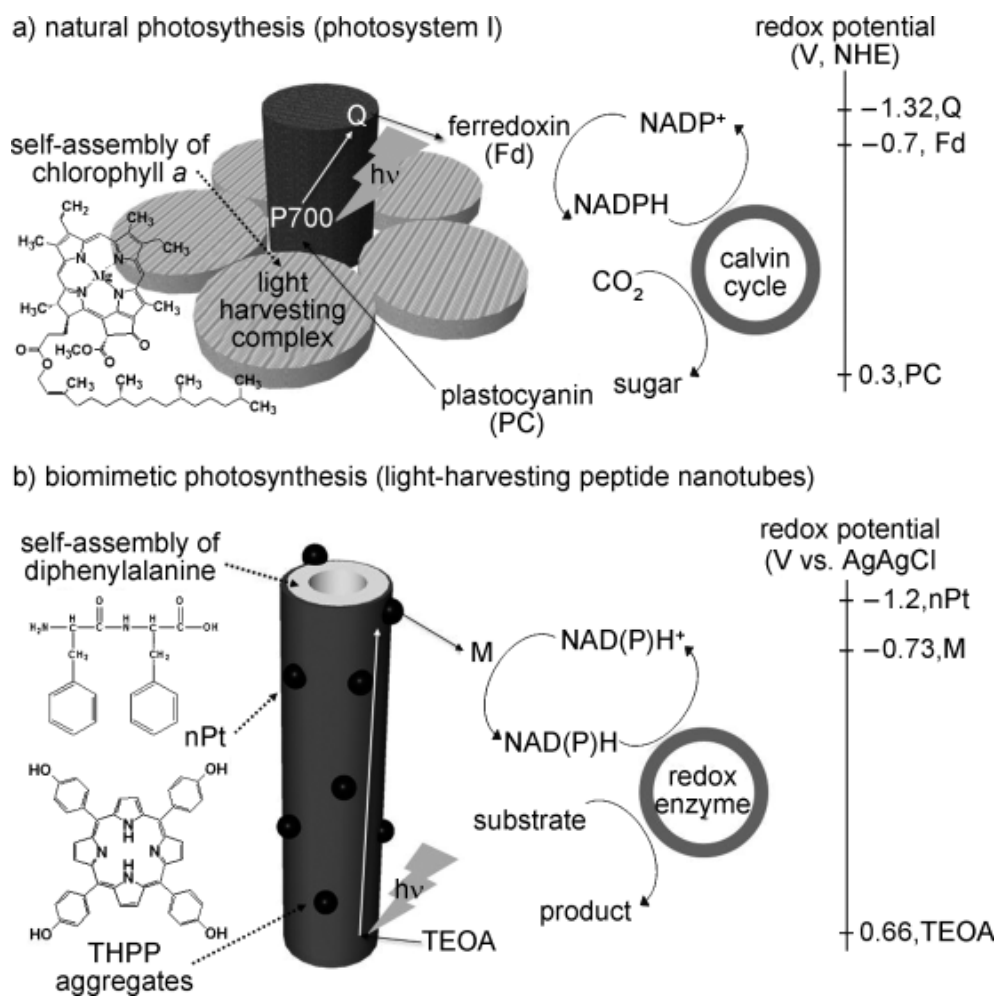
**Fig. 8** Schematics of **a)** natural and **b)** artificial photocatalysis using electron mediating cofactors. (Reproduced from Ref. 24)

The challenge of efficient water splitting lies in bridging single electron photochemistry with the four electron chemistry of water oxidation.



While the majority of photocatalytic research has focused on inorganic films and metal particles, there are some examples of self-assembling soft materials playing a functional role in photon capture and storage. Kim *et al.* describe a PSI mimic composed of a self-assembled diphenylalanine and tetra(p-hydroxyphenyl) porphyrin (THPP), shown in Figure 9<sup>24</sup>. Exciton coupling between THPP monomers accelerated light collection while platinum nanoparticles on the structure's surface accelerated charge separation between donor and mediator. On the platinum-porphyrin structure, a greater level of co-ordination between subunits leads to activity >40 times THPP alone. Like their biological counterparts, the efficiency of biomimetic systems at this

scale is highly dependent on the design of their subcomponents, which become a crucial element in the development of novel materials.



**Fig. 9** Schematics of **a)** natural photosynthesis in photosystem I and **b)** biomimetic photosynthesis supported by light-harvesting and conductive peptide nanotubes. White and black arrows indicate electron photoexcitation and transfer, respectively. (Reproduced from Ref. 24)

#### 1.4 Structures from 1-10 nm

Reactions that require organic solvents and metal catalysts only truly use the solvating molecules and surface metal atoms truly contribute. The development of



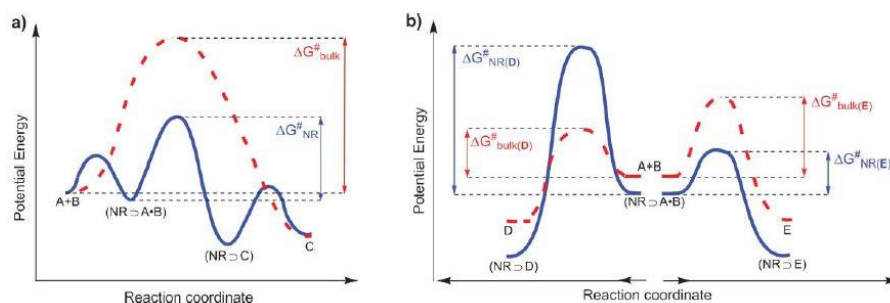
water soluble reaction vessels just large enough for the reaction to occur within could present an ideal solvent on its interior surface and contain surface-maximizing metal catalysts. Such a sustainable alternative sounds unlikely, yet enzymes operate in exactly this fashion. Enzymes are extremely efficient catalytic materials composed necessarily of organic macromolecules and the most common metals of the Earth's crust. Enzymes are not simply catalysts, or reaction vessels, or nanosensors, but all of these combined<sup>25</sup>. The active site is capable of bonding, catalyzing, and expelling substrates with phenomenal turnover.

They are not only able to recognize their specific precursors but in many cases they also sense and respond to the need for its reaction product and regulate its clearance rate accordingly. Enzymatic catalysis comprises substrate recognition and binding, geometric optimization, and catalytic binding of the transition state followed by efficient desolvation<sup>26</sup>. Broadly speaking, these phenomena fall into concerted thermodynamic and kinetic effects - confinement and catalysis. Putting a finer point on the effects either excludes too many enzymes to be general or includes properties too difficult to quantify to be of analytic use.

While there have been claims to the production of artificial enzymes, none match their biological counterparts for efficiency, specificity, and regulatory function<sup>27</sup>. That being said, the demands and constraints of natural and industrial products are very different. Enzymes in cytosol must separate their specific substrate from the variety of molecules present; synthetic reaction systems can be made to include only those molecules necessary for the desired product. Enzymes are also highly sensitive to environmental conditions and will lose conformation and effectiveness outside of tight boundaries of pH, radiation, temperature, ionic strength, and mechanical forces. An effective enzyme mimic should therefore incorporate the mechanisms of enzyme catalysis, though perhaps not their specificity, in a stable, confinement enhancing superstructure.

As Koblenz *et al.* note, the difference in reactivity in a confined nanospace or in the bulk will either alter  $\Delta G$  of activation ( $\Delta G^\ddagger$ ) or not<sup>28</sup>. A change indicates that the catalytic structure is able to stabilize the transition state. Enthalpic stabilization is achieved by the reduction in energy through covalent or non-covalent bonding of the transition state; entropic advantage is obtained by restricted rotational, vibrational, and translational motion in the confined nanodomain. A simplified profile of transition state stabilization within the nanoreactor is shown in Figure 10a. If  $\Delta G^\ddagger$  under confinement is equal to that of the bulk then the increased reaction rate is due only to the rise in effective molarity within the reaction vessel.

A confined microenvironment can also dictate whether one or another possible reaction product is optimized by blocking the pathway to others either by steric or energetic means. A schematic of this effect is shown in Figure 10b.



**Fig. 10** a) Simplified reaction profiles of a reaction in the bulk solution (dashed line) and within a nanoreactor (solid line). b) Simplified reaction profiles of a reaction leading to product D which is unfavoured within a nanoreactor (solid line) compared to the bulk solution (dashed line), and of a reaction leading to product E which is stabilized by the nanoreactor (solid line) compared to the bulk solution (dashed line). (Reproduced from Ref. 28)

#### 1.4.1 Confined catalysis

Enzymes in aqueous solution contain nanodomains lined by a combination of amino acid side groups that form a better solvation shell than the bulk solvent for substrate molecules but not for the reaction product. As described above, higher order confinement within vesicles or crowded cytosol contributes to the effectiveness of enzymes by increasing the probability of interaction with its substrate. Synthetic macromolecules can produce similar, though much less refined, nanodomains<sup>29</sup>.

In seeking to minimize interfacial energy, certain amphiphilic molecules in water will take conformations which produce internal hydrophobic regions. Interfacial tension between component molecules and water is fundamental for supramolecular self-assembly<sup>10</sup>. As a component molecule moves within the solvent, its sections with relatively high interfacial tension will tend to remain in contact with each other while more soluble, low interfacial tension areas will tend to remain in contact with the solvent.

This process of surface energy minimization stabilizes bonding by weak forces (van der Waals', electrostatic, hydrophobic, hydrogen) between components. Self-assembly can be said to occur if these associations produce an ordered structure at either thermodynamic equilibrium (static) or while dissipating energy (dynamic)<sup>30</sup>. This process is well understood for surfactant micelles and for morphological transitions by

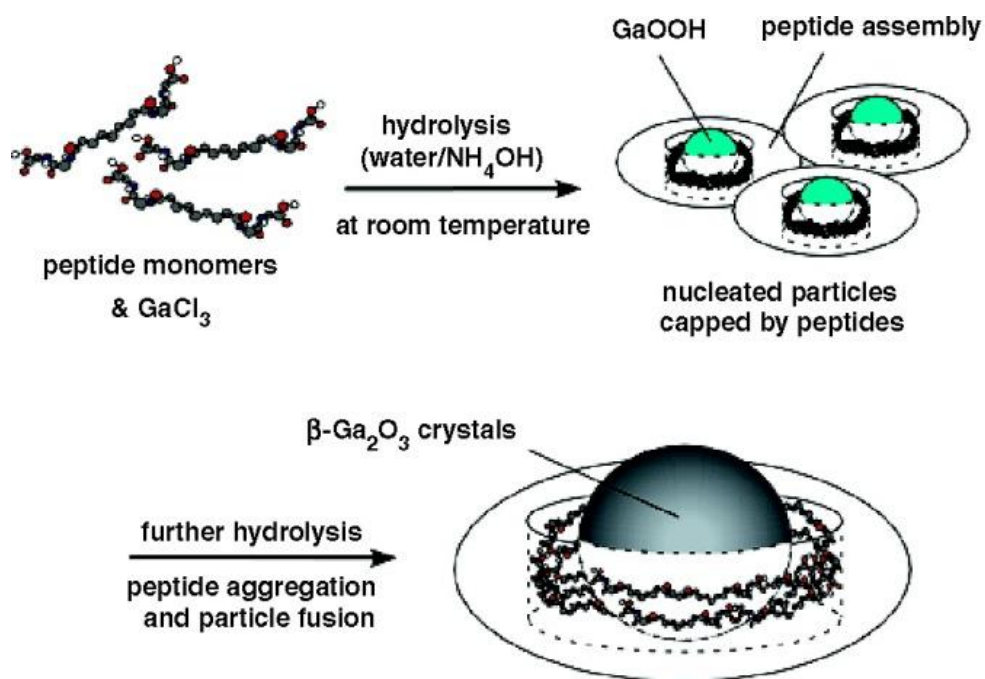
amphiphilic di-block copolymers<sup>31</sup>. If the resulting structure contains cavities lined with non-polar moieties these areas act as hydrophobic nanodomains. Accordingly, small molecules that are insoluble in water will accumulate within these cavities by a process similar to that which drove structural self-assembly.

Loading of the nanodomains will continue until reaching equilibrium with counteracting forces, most notably the electronic repulsion that determines the intrinsic density of the small molecule solute. To the extent that compressive forces are greater than repulsive forces, random movements by the solute molecules decrease and occupancy increases until reaching a stable packing conformation that minimizes global energy. In certain cases, the increased electronic excitation and lower entropy that result from the increased density and decreased degrees of freedom are sufficient to allow otherwise unfavourable reactions to be thermally initiated. It is the observation of molecular and reaction dynamics under nanoscale confinement which are inconsistent with bulk properties that define the confinement effect. The increase of reaction efficiency under confinement is often measured as effective molarity (EM), the ratio of the confined versus non-confined reaction rates<sup>32</sup>.

#### 1.4.2 Templated nanoparticle synthesis

An early biomimetic strategy for inorganic nanocrystal formation was to use the naturally occurring protein apoferritin as collector and cage for transition metals and metal oxides<sup>33</sup>. Because the cavity of apoferritin is 7 nm in diameter, monodisperse nanoparticles of iron, nickel, and chromium among others have been produced at that size<sup>34</sup>.

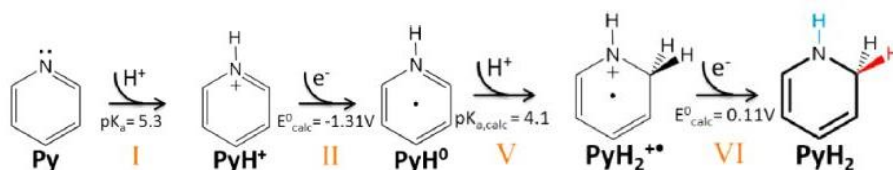
As well as promoting thermodynamically unfavourable reactions, effective molarity under confinement may also allow for reactions which are kinetically unfavourable in ambient conditions. Lee *et al.* observed that GaCl<sub>3</sub> in pH 10 solution with bolaamphiphile peptide could be hydrolyzed to  $\beta$ -Ga<sub>2</sub>O<sub>3</sub> at room temperature<sup>35</sup> (Fig. 11). They observed that without the peptide in solution, the reaction conditions could produce GaO<sub>2</sub>H but were too mild for further oxidation. Initial hydrolysis and size stabilization within the self-assembled peptide templates also produced GaO<sub>2</sub>H in monodisperse 10 nm crystals. In the second stage of the synthesis, the peptide containers aggregated and their contents fused into 50 nm metal oxide crystals. It is in this step that the peptide is thought to play the critical catalytic role leading from mixed phase clusters to pure -Ga<sub>2</sub>O<sub>3</sub> nanocrystals.



**Fig. 11** Illustration of  $\beta\text{-Ga}_2\text{O}_3$  growth mechanism via peptide capping and aggregation. (Reproduced from Ref. 35)

### 1.4.3 Solar fuel

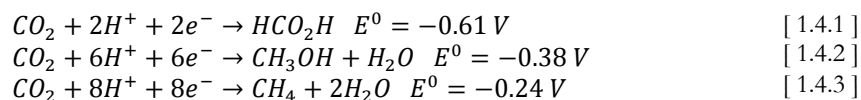
Solar fuels refer to the end products of photocatalyzed or photoelectrically-driven reactions that store the energy of collected solar radiation in chemical bonds. To be practical, the chemical products should be relatively easy to store, handle, and use; ideally no less so than current chemical fuels. Water splitting, as described above, produces a solar fuel in hydrogen gas. Its energy to mass ratio and clean combustion product, water, are excellent, but it becomes less attractive when considering the low energy to volume ratio and the accompanying difficulties in storage and distribution. Bearing in mind that nearly all of the energy humanity has ever used in our bodies and machines were sourced from plant-synthesized carbohydrates, and that the sun provides enough power in one hour to power human civilization for a year, photocatalytic fuel production is a high-value research goal<sup>36</sup>. The steady rise in atmospheric  $\text{CO}_2$  and its adverse effects since the industrial revolution makes the development of an industrial analogue to the Calvin cycle doubly attractive as it would provide a solution for energy and condensed carbon storage.



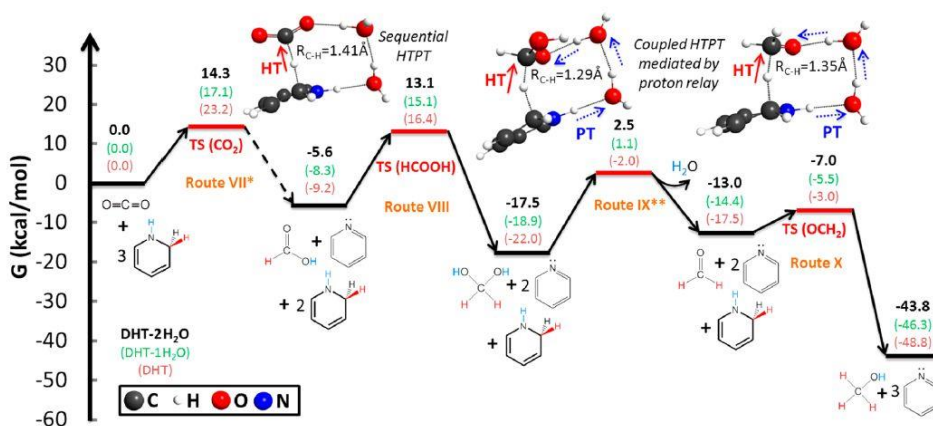
**Fig. 12** Formation of 1,2-dihydropyridine from pyridine (Reproduced from Ref. 39)

The simplicity of the concept belies the difficulty of the challenge: CO<sub>2</sub> is very stable and reducing it back to a useable fuel via light energy is a thus far intractable problem. Neither the enthalpic nor entropic components of reaction thermodynamics favour CO<sub>2</sub> reduction; reaction kinetics are likewise reduced by the need for multiple electron co-ordination. Kumar *et al.* cite the thermodynamic potentials listed in Equations 1.4.1 – 1.4.3 against a hydrogen electrode, pH 7, STP, 1M for other solutes<sup>37</sup>.

Naturally, the biological solutions are a source of inspiration. The extant literature on photoelectric or photocatalytic energy capture largely focuses on inorganic chemistry and as such lie outside the scope of this chapter. However, the transfer mechanism of protons and excited electrons from the cathode or semiconductor junction is typically dependent on organo-hydride molecules. Natural photosynthesis and nanobiosynthetic model systems use the nicotinamide adenine dinucleotide phosphate (NADP<sup>+</sup>) and NADPH redox couple as an electron mediator for CO<sub>2</sub> reduction. Barton *et al.* demonstrated 88-100% faradaic efficiency of CO<sub>2</sub> reduction to CH<sub>3</sub>OH using a p-GaP semiconductor electrode illuminated with light in the solar spectrum in pH 5.2 aqueous solution<sup>38</sup>. The presence of pyridine allowed for the reaction to occur at significant undervoltages but the catalytic mechanism was unknown.



Lim *et al.* used quantum mechanical methods to investigate pyridine's role in the transfer of two photoexcited electrons to CO<sub>2</sub><sup>39</sup>. The redox pathway from pyridine (Py) to 1,2-dihydropyridine (PyH<sub>2</sub>) and the reduction energies they found are shown in Figure 12. Density functional theory M06/6-31G\*\* was employed to map the reaction cycle and Møller–Plesset perturbation theory with aug-ccPVTZ basis sets were used to calculate point energies of the reaction and transition state energies to high precision. As Figure 13 illustrates, that study revealed that the Py-PyH<sub>2</sub> redox couple co-ordinates the reduction of CO<sub>2</sub> to formic acid HCO<sub>2</sub>H, methanediol



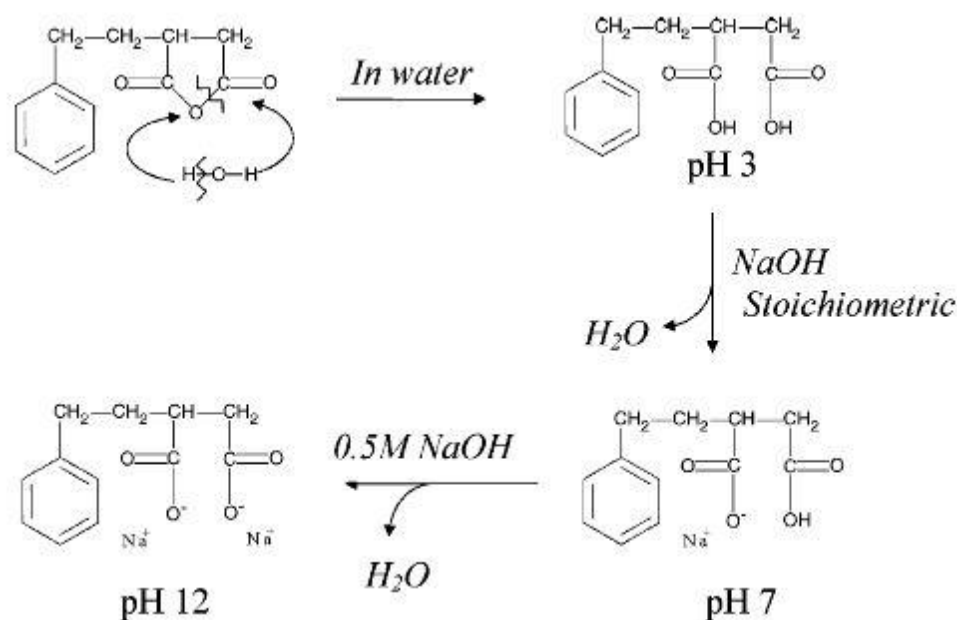
**Fig. 13** Conversion of CO<sub>2</sub> to CH<sub>3</sub>OH and H<sub>2</sub>O by PyH<sub>2</sub> proceeds through three hydride and proton transfer steps. The reported free energies correspond to stationary points along the reaction potential energy surface models, catalyzed by the PyH<sub>2</sub>/Py redox couple. (Reproduced from Ref. 39)

CH<sub>2</sub>(OH)<sub>2</sub>, and finally to methanol CH<sub>3</sub>OH by sequential hydride (2e<sup>-</sup> + H<sup>+</sup>) and proton (H<sup>+</sup>) transfers (HTPT).

Pyridine's function as a recyclable two electron mediator through HTPT makes it a small, stable synthetic analogue to NADP(H) for catalyzing the reduction of CO<sub>2</sub> into a usable fuel. The original experimental work was performed in bulk solution with a macro-scale semiconductor electrode. In combination with metal or semiconductor nanocrystals and a macromolecular confinement structure, the results of this theoretical study could be incorporated into an efficient and fully artificial mimic of the biological carbon reduction process.

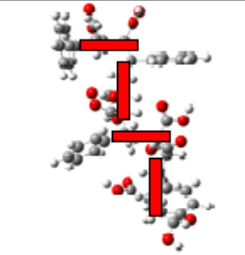
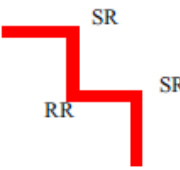
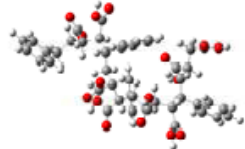

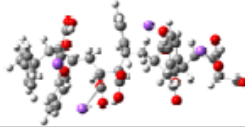

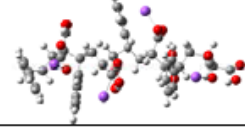

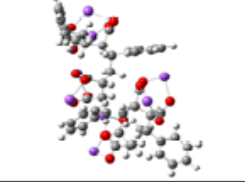

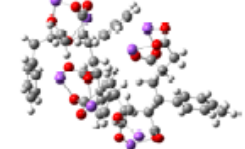

#### 1.4.4 Biomimetic nanoreactors

Polystyrene-*alt*-maleic anhydride is a particularly interesting polymer for the construction of soft nanoarchitectures that confine and support organic reactions in water<sup>40</sup> (Fig. 14). It is an amphiphilic alternating copolymer composed of styrene and maleic acid groups. Dynamic light scattering (DLS) experiments demonstrate that the aggregation of polymer chains into larger structures reaches a maximum at neutral pH<sup>41</sup>. Small-angle neutron scattering experiments (see §2.2 for details on SANS theory and operation) revealed that the polymer aggregates comprise a highly organized nanostructure<sup>42</sup>.



**Fig. 14** One repeating unit of the alternating styrene and maleic acid co-polymer. The pH sensitivity of poly(styrene-alt-maleic acid) is produced by the successive deprotonation of its maleic acid moiety. Supramolecular association is optimized in the monodeprotonated state. (Reproduced from Ref. 40)

Specifically, the polymer chains were found to form nanotubes with a 2.8nm inner and 4.0nm outer diameter. A quantum mechanical modeling study further determined that intramolecular hydrogen bonding induces rigidity and chirality (through directional rotation of styrene groups by  $120^\circ$  per monomer) which sufficiently reduce the entropic cost of association to benefit from the enthalpic advantages of minimizing styrene exposure to water. Hydrogen bonding, and hence its linear morphology, was shown to exist only for the monodeprotonated maleic acid group, as shown in Fig. 15<sup>43</sup>. The entropy associated with the randomly kinked, globular morphologies produced by the fully protonated or deprotonated polymer is greater than the styrene-water surface energy to overcome, fully explaining the pH sensitivity shown by DLS. Cryo-TEM images show that the nanotubes create secondary and tertiary structures as they align into crystalline sheets and stacks. The dimensions measurable by TEM exactly match those determined by SANS and predicted by simulation.

pH	Chirality	Optimised structure	Backbone
pH 3	SR RR SR		
	SR SR SR		
pH 7	SR RR SR		
	SR SR SR		
pH 12	SR RR SR		
	SR SR SR		

**Fig. 15** The electronic structure of quadrimers of SMA were modeled by quantum mechanical methods to show that its chain linearity, and therefore self-assembly, is pH dependent and but independent of chirality. (Reproduced from Ref. 40).

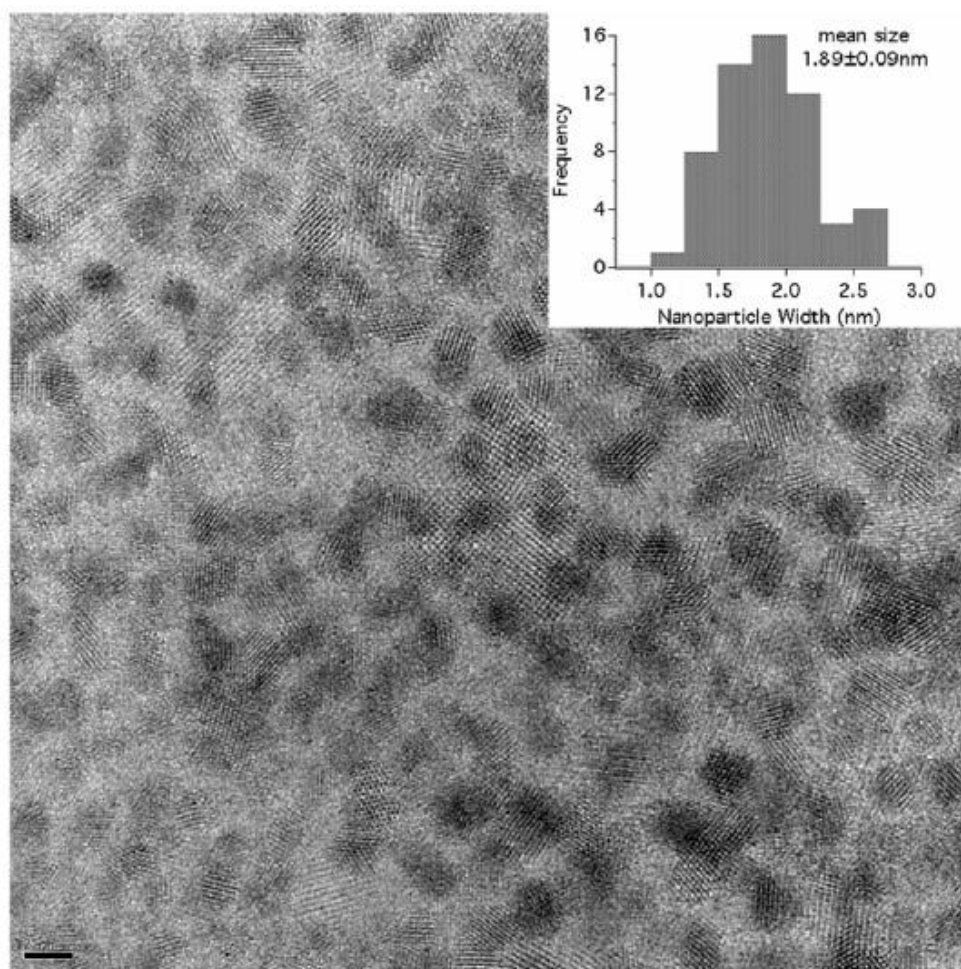
Self-assembly of SMA into nanotubes produces soluble hydrophobic nanodomains which, like larger micelles, can host small hydrophobic molecules. At less than 3 nm, the interior dimension is sufficiently small to exploit confinement for catalysis. This was shown by Li *et al.* through the spontaneous polymerization reaction of pyrrole



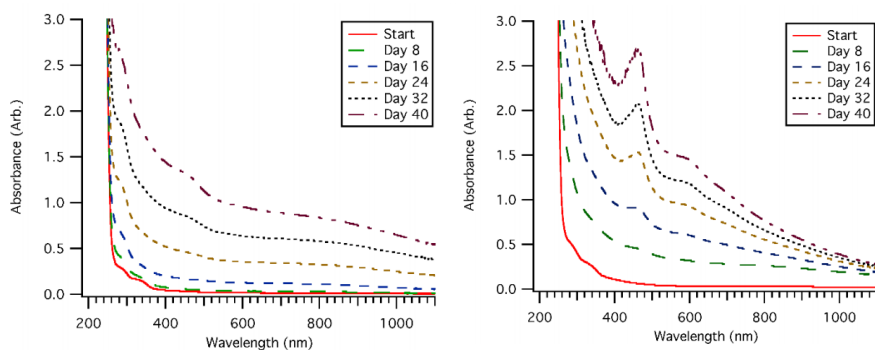
dissolved in aqueous 1% wt/wt SMA solution<sup>44</sup>. As a bulk liquid, electrochemical or strong oxidizing agents are necessary to induce polymerization but the reaction becomes spontaneous within the SMA confinement space, removing the requirement for electrical or chemical activation. Pyrrole polymerization is energetically favourable only for oligomers of six or more: where the bonding reaction of two is unlikely, the probability of six bonding simultaneously is effectively zero. The effective molarity is therefore difficult to calculate in this case since the reaction rate of pyrrole outside of confinement is too slow to be practicably quantified.

The assertion that spontaneity is a sole consequence of confinement was proven by attempting pyrrole polymerization inside larger styrene-maleic acid micelles up to 50 nm in diameter: no reaction was observed in the larger volume. However, attempting the reaction in poly(isobutylene-*alt*-maleic acid), a related polymer with 2 nm hydrophobic confinement spaces, did incite polymerization. As mentioned previously, polypyrrole is an increasingly important conductive polymer for a wide range of technological fields whose polymerization generally requires specialized reaction agents and association with a degradable polymer superstructure. The polypyrrole synthesis method developed by Li *et al.* both removes the need for chemical polymerization agents and incorporates the product into a biocompatible, biodegradable polymer nanoarchitecture.

The well-defined structure of the cavities of the SMA template also provides a controlled environment for the growth of metal nanoclusters. The hydrophobic metal salt platinum(II) chloride was added to SMA in aqueous solution with NaBH<sub>4</sub> reducing agent to produce nanoparticles through a process analogous to biotemplated crystal growth. Given the interstitial spaces, metal crystals under 3 nm were expected. Monodisperse platinum crystals were observed to form with or, surprisingly, without additional reducing agent<sup>45</sup>. Figure 16 shows HR-TEM micrographs of the SMA nanosheet and platinum-SMA nanoreactor system. By reproducing the pyrrole polymerization experiment in the SMA-Pt nanoreactor the reaction rate was three times faster than in SMA alone (Fig. 17). The SMA-Pt nanoreactor mimics enzymatic action by initiating and catalyzing an energetically unfavourable reaction through confinement and metal coordination. By promoting polymerization without harsh physical or chemical activation agents the nanoreactor offers an environmentally-friendly alternative to traditional synthetic processes.



**Fig. 16** HR-TEM image of platinum nanocrystals synthesized in the SMA supramolecular nanostructure without additional reducing agent. (Reproduced from Ref. 45)



**Fig. 17** Pyrrole polymerization in solution with SMA (left) and Platinum-SMA (right) nanostructures. The characteristic peak at 430 nm appears earlier and sharper with the platinum catalyst. (Reproduced from Ref. 45)

## 1.5 Objectives

As we have developed the tools that allow us to access the nanoscale it has become clear that millennia of biological evolution have resulted in dynamic, responsive molecular structures. Proteins are especially versatile self-assembling, supramolecular polymers whose construction and function continue to provide new insights for the development of advanced artificial materials. However, Nature and humanity have different design goals and constraints: living systems favour accessibility of raw materials and adaptability over hardness while human industry can afford more exotic, single-purpose components and harsher operating conditions. Industry, like Nature, benefits from energy efficiency. By understanding the mechanisms driving biological structures, artificial analogues might be developed that amplify their effects by their ability to function at substrate concentrations or environmental conditions toxic to the model organisms.

The primary purpose of this project was to study the platinum–poly(styrene-*alt*-maleic acid) system in order to gain an understanding of the platinum(II) chloride reduction mechanism particularly, and the effect of confinement generally. Reaction dynamics were probed by changing the solution pH, reactant concentrations, surface chemistry of the confinement cavity, and reactant identity. For the latter, the reaction was attempted with gold(I) chloride used in place of platinum(II) chloride in SMA solution, and poly(isobutylene-*alt*-maleic acid) replacing SMA for the platinum reduction reaction. The polymer template and metal nanocrystals were extensively characterized theoretically and experimentally. Over the course of this work, new

composite materials and phases of existing materials were discovered whose properties promise a rich area for ongoing research.

In Chapter Two the methods used to explore the polymer-metal nanosystems will be introduced. The range of scales and materials under investigation required an innovative mix of theoretical simulation and laboratory experiment to achieve a thorough characterization. Density functional theory provides high-accuracy quantum mechanical solutions for model systems at a lower demand on computational resources than alternative techniques. Light and matter scattering spectroscopic methods permitted analysis of both structural and reaction dynamics data. Finally, high resolution electron microscopy was used to confirm and clarify the polymer-metal nanostructures. As will be shown, each method is a powerful tool for nanotechnology whose limitations are overcome by application in concert with the others.

Presentation of the project's results begins with a discussion of the polymer superstructure in Chapter Three. A previously unknown correlation between molecular weight and supramolecular architecture is revealed. Chapter Four details the development of platinum- and gold-SMA composite nanosystems. The platinum chloride reduction method introduced above is explored and expanded to a wide pH range and to a second confinement-inducing polymer template. This chapter also includes a description of the first reported method for the synthesis of stable, ultrathin gold sheets featuring a hexagonal close packed crystal structure.

Chapter Five comprises a heuristic integration of the experimental results into a coherent theory. Noting that both thermodynamic and kinetic reaction characteristics are altered by confinement, a drastic and highly localized water phase change is proposed as a source for the potential energy needed to explain the metal salt reduction and increased organic reactivity observed. These conditions challenge the assumptions of classical thermodynamics and suggest a path for the expansion of theory to non-equilibrium systems.

The thesis concludes in Chapter Six with an aggregation of the main experimental and theoretical findings and an outlook on the future of confined nanosystems. It is hoped that the evidence and ideas presented herein will inform further research into the function of biological confinement and the development of fundamentally new nanomaterials.

## 2 Methods

### 2.1 Quantum Theoretical Methods

#### 2.1.1 Survey of Quantum Methods

Schrödinger's wave equation provides the theoretical foundation for the quantum chemical simulation methods. A brief survey of its own underpinnings shows it to be the culmination and capstone of the radical advances in physics during the first decades of the 20<sup>th</sup> century.

Max Planck's 1901 solution to the blackbody problem led to the quantization of energy and an expression for the energy of a photon<sup>46</sup>:

$$E = h\nu \quad [2.1.1]$$

where  $\nu$  is the frequency of light and  $h$  is what would become Planck's constant. Einstein's application of Planck's theory to the photoelectric effect in 1905 would lead him to recognize that quanta of light energy, photons, could be treated as particles as well as waves<sup>47</sup>. This realization would also inspire his discovery that energy is directly related to mass  $m$  through:

$$E = mc^2 \quad [2.1.2]$$

[2.1.1] and [2.1.2] can then be combined to give:

$$\lambda = \frac{h}{mc} \quad [2.1.3]$$

where  $\lambda$  is the wavelength equivalent of a given mass. Yet it was nearly twenty years later that Louis de Broglie proposed the inverse relationship: that particles might be treated as waves<sup>48</sup>. Generalizing [2.1.3] to velocities below the speed of light produces an equation for the wavelength of particles with momentum  $p$ :

$$\lambda = \frac{h}{p} = \frac{h}{mv} \quad [2.1.4]$$

which is to say that higher momentum particles carry a proportionally shorter wavelength. Given that kinetic energy  $K = \frac{m}{2}v^2$  and total energy is the sum of kinetic and potential energies  $E = K + V$ , the de Broglie wavelength of an object is:

$$\lambda = \frac{h}{\sqrt{2m(E - V)}} \quad [2.1.5]$$

Schrödinger's insight was to solve for standing de Broglie waves using a classical time-independent wave equation<sup>49</sup>:

$$\nabla^2\Psi = -\left(\frac{2\pi}{\lambda}\right)^2\Psi \quad [2.1.6]$$

which gives the time-independent Schrödinger equation:

$$\left[-\left(\frac{h^2}{8\pi^2m}\right)\nabla^2 + V\right]\Psi = E\Psi \quad [2.1.7]$$

The solution to every problem concerning the structure of matter, which is to say every problem in chemistry, is included in Schrödinger's equation. That is not to say that solutions are always accessible. The simplicity of the equation's form belies the difficulty in solving it; however, assumptions may be introduced to simplify the calculations. The Born-Oppenheimer approximation holds that electronic orbits adaptation to nuclear movement is so nearly instantaneous that the nuclei may be considered static and so dismisses as negligible a nuclear kinetic term from the total energy expression below.

For an isolated N-body system under the Born-Oppenheimer approximation, we begin with Schrödinger's equation in its most economical expression:

$$\hat{H}\Psi = E\Psi \quad [2.1.8]$$

where  $E$  is the electronic energy and  $\Psi = \Psi(\mathbf{x}_1, \mathbf{x}_2, \dots, \mathbf{x}_n)$  such that  $\mathbf{x}_i$  represents a position in spin-orbital space that includes the three-dimensional space co-ordinates  $\mathbf{r}_i$  and the binary ( $\pm 1/2$ ) spin coordinate  $s_i$ . The Hamiltonian operator comprises the three-dimensional kinetic energy of  $i$  electrons, the external potential field produced by system nuclei, and the inter-electron repulsion energy:

$$\hat{H} = \sum_{i=1}^N \left(-\frac{1}{2}\nabla_i^2\right) + \sum_{i=1}^N v(\mathbf{r}_i) + \sum_{i<j}^N \frac{1}{r_{ij}} \quad [2.1.9]$$

where the external potential on the electron  $i$  is proportional to its radius from each nucleus  $\alpha$  with charge  $Z$ :

$$v(\mathbf{r}_i) = - \sum_{\alpha} \frac{Z_{\alpha}}{r_{i\alpha}} \quad [2.1.10]$$

It is the many body problem implicit in the final term that precludes Schrödinger's equation from being solved exactly for any system larger than the hydrogen atom. Electron-electron interactions must account for classical electrostatic repulsion as well as non-classical correlation and exchange energies, concepts that are described in more detail in §2.1.3.

### 2.1.2 Wavefunction Approximations

Practical methods for extracting quantitative prediction of chemical phenomena from Schrödinger's equation require sound approximations of those elements which cannot be computed exactly. Chief among these is the wavefunction itself. The exact physical meaning of the wavefunction is unclear, but in his 1926 paper Max Born demonstrated that it multiplied by its complex conjugate,  $|\Psi|^2$ , corresponds to the probability distribution function for results of a given measurement<sup>50</sup>. Born's statistical method for extracting information from the wavefunction is foundational to the understanding of quantum mechanics laid out by Niels Bohr and Werner Heisenberg known as the Copenhagen Interpretation.

The idea that the wavefunction is directly related to the probability that an electron will be found within a given region of space suggests a method for constructing an unknown wavefunction based on the type and location of atoms in the system. In the method described below, the wavefunction of a system is approximated by the hierarchical optimization of the coefficients of simple probability functions in linear combination.

#### Basis Functions

The primary assumption of the mathematical models described below is that the probability distribution for the location of a single electron will be contained within the bounds of atomic orbitals and so can be calculated as a weighted sum of basis functions describing the orbitals involved. The first basis functions to be used were Slater-type orbitals (*STO*) in the form:

$$STO = Nr^{n-1}e^{-\zeta r} \quad [2.1.11]$$

where zeta  $\zeta$  is the orbital exponent governing the orbital's spatial extent,  $r$  is the radius in Angstroms,  $n$  is the principle quantum number, and  $N$  is a normalization constant. Because these functions form a cusp at 0 and decay exponentially towards zero for long-range solutions, Slater-type orbitals represent the real electron distribution and give good energy results for hydrogen-like systems<sup>51</sup>. Wavefunction approximation, that is the estimation of the probability of locating electrons within a given volume, for systems comprising more than one electron requires the integration of the basis functions for each electron, but the form of Slater functions makes their integral difficult to evaluate.

By contrast, gaussian functions,  $g$ , of the form

$$g = Nr^{n-1}e^{-\zeta r^2} \quad [2.1.12]$$

have no independent physical meaning but their integrals are readily computed. In the primary level of optimization, contracted gaussian basis functions can be built by linear combination of primitive gaussians to better resemble the orbitals they are meant to represent:

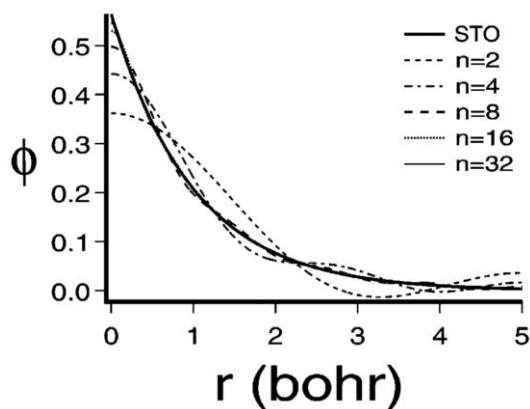
$$\varphi_\mu = \sum_s d_{\mu s} g_s \quad [2.1.13]$$

where the coefficients  $d_{\mu s}$  have been set to produce a basis function  $\varphi_\mu$  comparable to an STO for quality of representation while remaining easily handled (Fig. 18). A better orbital representation is produced by including more primitive gaussians in the contracted function but comes with accordingly greater computational cost<sup>52</sup>.

Individual basis functions may now be assembled into basis sets which adequately model the atomic orbitals of electrons of a given atom<sup>53</sup>. The atomic orbital  $\phi_n$  is built through a second level of optimization of the coefficients  $j_{n\mu}$  of  $\mu$  basis functions  $\varphi_\mu$  in linear combination:

$$\phi_n = \sum_\mu j_{n\mu} \varphi_\mu \quad [2.1.14]$$





**Fig. 18** Comparison of Slater-type (STO) and Gaussian (GTO) orbitals as a function of radius. Because they form a cusp at  $r = 0$  and trend exponentially to 0 as  $r \rightarrow \infty$ , STOs accurately describe both short and long range behaviour of atomic orbitals. GTOs better approximate STOs as the number of primitive Gaussians  $n$  increases.

### Molecular Orbital Theory

Molecular orbital (MO) theory describes the consequences of a third level of optimization in which electron distribution over a molecular orbital  $\psi$  is modeled as a linear combination of  $n$  atomic orbitals  $\phi$ :

$$\psi_k = \sum_n c_{kn} \phi_n \quad [2.1.15]$$

where  $c_n$  is the proportional contribution of its corresponding atomic orbital to the whole molecular orbital<sup>54</sup>. Like the wavefunction it approximates, the square of the molecular orbital determinant represents the probability distribution for the location of electrons in a field of stationary nuclei.

In the ideal case the determinant of the molecular orbital is exactly equal to the wavefunction and

$$\Psi = |\psi_k| \quad [2.1.16]$$

### Variational Method

Having shown that a linear combination of electronic and atomic orbitals may produce a function arbitrarily close to the true molecular wavefunction, what remains to be seen is a method by which the coefficients may be optimized, or indeed what is meant by 'optimized'. Schrödinger's equation tells us that every possible energy state of an atomic system is described by one and only one wavefunction. The energy state

most commonly sought is the most stable attainable for the system, called the ground state energy,  $E_0$ , and is accordingly described by the ground state wavefunction,  $\Psi_0$ . By definition, any wavefunction  $\Psi_k \neq \Psi_0$  must describe a less stable system configuration and therefore correspond to an energy  $E_k > E_0$ <sup>52</sup>.

By multiplying both sides of Equation 2.1.8 by  $\Psi$  we find that

$$\Psi^* \hat{H} \Psi = |\Psi|^2 E \quad [2.1.17]$$

Integrating both sides and solving for energy gives us an expression:

$$E[\Psi] = \frac{\int \Psi^* \hat{H} \Psi dx}{\int \Psi^2 dx} \quad [2.1.18]$$

Substituting Equations 2.1.15 and 2.1.16 into 2.1.18 gives the MO theory equivalent:

$$E[\psi_k] = \frac{\sum_k |c_k|^2 E_k}{\sum_k |c_k|^2} \quad [2.1.19]$$

Given the above assertion that any trial wavefunction not equal to the ground state will give a higher energy,  $E_k$  becomes an upper bound for approximation of  $E_0$ . The lower bound is found at the minimum,  $E_0$ , which for Equation 2.1.18 lies where  $dE[\psi_k]=0$ . Iterative adjustment of the trial coefficients to minimize energy successively lowers  $E_k$  with  $E_0$  as a limit and is therefore an algorithmic approach to the true ground state<sup>54</sup>. While the ground state might not be found exactly in practice, MO theory and the variational method allow us to come arbitrarily close.

### 2.1.3 Hartree-Fock Theory

Hartree-Fock theory is an application of the variational method for fixing coefficients of atomic orbitals in the expanded molecular orbital<sup>55</sup> (Equation 2.1.15). To determine the test energy  $E_k$  we must apply a Hamiltonian operator to the molecular orbital and to do so we return to the problem of electron-electron interactions introduced in §2.1.1.

Due to the equal and negative charge of every electron in a set, their location at a given moment ought to minimize repulsive energy within the set. The Coulomb energy  $J$  is a classical term for a pair of electrons separated by a distance  $\mathbf{r}_{12}$ ; sets larger than two create a many-body problem that motivated the development of the methods described in the following sections.

Two further electronic interactions are not classically explicable: exchange and correlation. First, exchange energy relates to the quantum mechanical postulate that

electrons are indistinguishable, *i.e.* their wavefunctions are equal apart from a change in spin sign (+ or - 1/2). Their repulsion according to Pauli exclusion affects the mean separation between electron pairs and so the total energy. Second, for the condition of repulsion energy minimization to be consistently met, the motion of each electron within its orbital must be highly correlated with that of every other. Calculation of the energetic cost of correlation over a large set of electrons is an unsolved problem in quantum chemistry.

### The Fock operator

To avoid the difficult calculations required to determine the energy of a system of more than two electrons, the Fock operator  $\hat{F}$  gives the energy for a single electron moving in an effective field composed by the forces generated by nuclei and the other electrons in the system<sup>56</sup>:

$$\hat{F}(\mathbf{x}_1) = \hat{h} + \sum_i^n (2\hat{J}_i(\mathbf{x}_1) - \hat{K}_i(\mathbf{x}_1)) \quad [2.1.20]$$

The operator  $\hat{h}$  accounts for the nuclear energy contribution while the remaining term is a sum single electron kinetic and potential energy operators. The first summation term captures the Coulombic repulsion for each electron in a mean charge field composed of the remaining electrons. It is described by the Coulomb operator  $\hat{J}_i$ :

$$\hat{J}_i(\mathbf{x}_1) = \int \frac{1}{r_{12}} \psi_i(\mathbf{x}_2) \psi_i^*(\mathbf{x}_2) d\mathbf{x}_2 \quad [2.1.21]$$

The second term in the summation  $\hat{K}_i$  is the exchange operator for each electron pair. Electron exchange energy has no classical equivalent. It is a purely quantum effect arising from Pauli Exclusion Principle<sup>57</sup>. It is constructed similarly to the Coulomb operator but exchanges a spin-orbital of  $\psi_j$  for one of  $\psi_i$ :

$$\hat{K}_i(\mathbf{x}_1) \psi_j(\mathbf{x}_1) = \left[ \int \frac{1}{r_{12}} \psi_j(\mathbf{x}_2) \psi_i^*(\mathbf{x}_2) d\mathbf{x}_2 \right] \psi_i(\mathbf{x}_1) \quad [2.1.22]$$

The independent particle approximation introduced by Fock provides a means to calculate the energy of each spin-orbital  $\psi_i$  through:

$$\hat{F}\psi_i = \varepsilon_i \psi_i \quad [2.1.23]$$

### The Hartree-Fock equation

John C. Slater showed that matrix mechanics could be used to ensure adherence to Pauli exclusion and electron anti-symmetry<sup>51</sup>. The Hartree method is an iterative variational method to calculate of atomic and molecular energies from the Slater determinant of a matrix composed of a set of independent orbitals. By adding explicit treatment of electron exchange energy, the Fock operator represented a considerable improvement on Hartree's original model. The Fock operator is generalized for matrix operations as:

$$\mathbf{F}\psi = \epsilon\psi \quad [2.1.24]$$

so that Equation 2.1.23 holds for every spin-orbital of the set and energy is an eigenvalue of the eigenfunction Equation 2.1.20. Likewise, the electronic energy of the system may be approximated by the sum spin-orbitals calculated by Equation 2.1.23:

$$\hat{H}_F\psi_i = \sum_i \hat{F}\psi_i = E_F\psi_i \quad [2.1.25]$$

The total energy is calculated by adding the nuclear potential energy to Equation 2.1.25. Additionally, the energy  $\epsilon_i$  of each spin-orbital also has physical meaning as an approximation of the energy required to remove an electron from its respective spin-orbital (its ionization energy).

In general, the Hartree-Fock method is capable of high-quality solutions but because it neglects correlation energy, the Hartree-Fock method will always return a total energy greater than the true value.

#### 2.1.4 Density Functional Theory

The method for constructing an approximate wavefunction presented in Section 2.1.2, integrating the probability functions for individual electrons, implies that the result is equivalent to a probability function for electron density<sup>58</sup>. Within a year of the publication of Schrödinger's equation, Llewellyn Thomas working in Britain and Enrico Fermi in Italy independently proposed similar methods to approximate electron distribution via electron density directly<sup>59,60</sup>. The Thomas-Fermi model proposes a uniform distribution of electrons into small cubic volumes such that each volume element  $\Delta V$  contains  $\Delta N$  electrons. Through a derivation that leads from the calculation of energy for a particle in an infinite well through the density of states at the Fermi level and the integral of all doubly-occupied states to arrive at a formula for kinetic energy as a functional of electron density  $\rho = \Delta N/\Delta V$ :

$$K_{TF}[\rho] = \frac{3}{10} (3\pi^2)^{\frac{2}{3}} \int \rho^{\frac{5}{3}}(\mathbf{r}) d\mathbf{r} \quad [2.1.26]$$

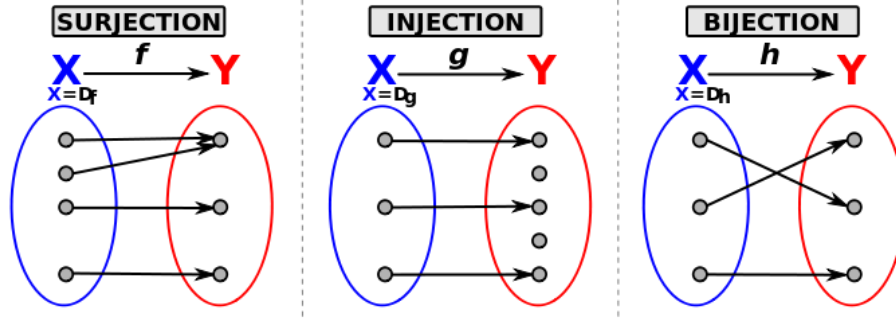
Neglecting the non-classical electron interaction terms, the total system energy can be formulated as a sole function of electron density:

$$E_{TF}[\rho] = K_{TF} - Z \int \frac{\rho(\mathbf{r})}{r} d\mathbf{r} + \frac{1}{2} \iint \frac{\rho(\mathbf{r}_1)\rho(\mathbf{r}_2)}{|\mathbf{r}_1 - \mathbf{r}_2|} d\mathbf{r}_1 d\mathbf{r}_2 \quad [2.1.27]$$

where the first term represents kinetic energy, the second the attractive nuclear potential, and the third term accounts for electron-electron repulsion. The Thomas-Fermi model, with modification, could adequately model atomic energies but failed at the molecular level since it could not account for the existence of chemical bonds.

### Hohenberg-Kohn

While the Thomas-Fermi model continued to be improved upon, its limitations were not overcome until 1964 when Hohenberg and Kohn re-examined the concept of electron density and its relationship to the system it describes<sup>61</sup>. Since, under the Born-Oppenheimer approximation, nuclear positions are set and unchanging, the external field acting on the electrons is similarly unchanging and so the other terms of the system, namely kinetic energy and electron interaction, are left to rearrange themselves to minimize total energy. As functions map variables to a scalar value, so functionals map functions to a scalar. To show that a functional of electron density is equivalent to the wavefunction, it would need to be both surjective, every permissible energy level being paired with exactly one electron density function, and injective, mapping each electron density function to only one energy level. Schematic representations of this requirement are shown in Figure 19. Since the electronic terms are plainly dependent on the number of electrons  $N$  and  $N = \int \rho(\mathbf{r}) d\mathbf{r}$ , it only remained to be shown whether  $\rho(\mathbf{r})$  could also determine the nuclear potential,  $v(\mathbf{r})$ .



**Fig. 19** A surjective function  $f$  maps at least one element of  $X$  to every element of  $Y$ ; an injective function  $g$  maps at most one element of  $X$  to a unique  $Y$ ; a function  $h$  that is both surjective and injective maps one and only one element of  $X$  to each and every element of  $Y$ .

Proceeding by *reductio ad absurdum*, the Hohenberg-Kohn proof began with the assumption that two external potentials  $v(\mathbf{r})$  and  $v'(\mathbf{r})$  with their associated wavefunctions  $\psi$  and  $\psi'$  could give rise to the same electron density function  $\rho(\mathbf{r})$ . Unless  $v(\mathbf{r}) = v'(\mathbf{r})$ ,  $\psi$  and  $\psi'$  satisfy different Schrödinger equations and give rise to Hamiltonians  $\hat{H}$  and  $\hat{H}'$  and system energies  $E$  and  $E'$  accordingly. The ground state is the lowest energy state for a given electronic system, defined as:

$$E_0 = \psi \hat{H} \psi \quad [2.1.28]$$

implying that

$$\begin{aligned} E_0 < \psi \hat{H} \psi &= E'_0 + (\psi, [\hat{H}' - \hat{H}] \psi) \\ &= E'_0 + \int \rho(\mathbf{r}) [v'(\mathbf{r}) - v(\mathbf{r})] d\mathbf{r} \end{aligned} \quad [2.1.29]$$

Exchanging the prime and non-prime values leads to the inconsistency:

$$E + E' < E + E' \quad [2.1.30]$$

so that one must conclude that  $v(\mathbf{r})$  is a unique functional of  $\rho(\mathbf{r})$ , *i.e.*  $V_{ext}[\rho]$ , to within a constant. Therefore the electron density function contains information equivalent to the wavefunction; ground state energy and all other properties may be determined from the function:

$$E[\rho] = K[\rho] + U_{ee}[\rho] + V_{ext}[\rho] \quad [2.1.31]$$

which is the central theorem of density functional theory.

### Kohn-Sham Method

Armed with the assurance of theoretic validity granted by Equation 2.1.31, Kohn and Sham sought to shed the limitations inherent to the Thomas-Fermi method and develop a density functional approach capable of providing exact solutions. Their method separates the kinetic energy term into an exactly calculable non-interacting term,  $K_s$ , and an electron-electron interaction correction,  $E_{xc}$ <sup>62</sup>.

In the special (and non-physical) case of a system of non-interacting electrons, Kohn and Sham were able to frame the exact electron density and expectation value of kinetic energy as:

$$\rho(\mathbf{r}) = \sum_i^N \sum_s |\psi_i(\mathbf{r}, s)|^2 \quad [2.1.32]$$

and

$$\langle K_s[\rho] \rangle = \sum_i^N -\frac{1}{2} \nabla^2 \psi_i \quad [2.1.33]$$

where  $N$  orbitals are occupied with an equal number of non-interacting electrons.

By logic similar to that invoked by Hartree-Fock, Kohn and Sham devised a Hamiltonian that neglects electron-electron interaction for which the ground state electron density is exactly  $\rho$  whose corresponding wavefunction is:

$$\Psi_s = \frac{1}{\sqrt{N!}} \det[\psi_1 \psi_2 \dots \psi_N] \quad [2.1.34]$$

which permits us to rewrite Equation 2.1.31 as

$$E[\rho] = K_s[\rho] + J_s[\rho] + \int \rho(\mathbf{r})v(\mathbf{r}) d\mathbf{r} + E_{xc}[\rho] \quad [2.1.35]$$

where  $K_s$  and  $J_s$  contain the non-interaction kinetic and potential energies respectively,  $v(\mathbf{r})$  is the external (nuclear) potential, and  $E_{xc}$  comprises the difference between those and the true energy. Setting the appropriate constraints on  $\rho$  or, equivalently, on the molecular orbitals  $\psi$ , leads to the Kohn-Sham equations for orbital energy:

$$\left[ -\frac{1}{2} \nabla^2 + v_{\text{eff}} \right] \psi_i = \varepsilon_i \psi_i \quad [2.1.36]$$

where

$$v_{\text{eff}}(\mathbf{r}) = v(\mathbf{r}) + \int \frac{\rho(\mathbf{r}')}{|\mathbf{r} - \mathbf{r}'|} d\mathbf{r}' + v_{xc}(\mathbf{r}) \quad [2.1.37]$$

and  $\rho(\mathbf{r})$  is defined as in Equation 2.1.32 and which, as a set, form the computational basis for current density functional methods.

Noting the similarity in the form of Equations 2.1.36 and 2.1.23, we can compare Kohn-Sham and Hartree-Fock theory. First, Hartree-Fock is approximate by definition while Kohn-Sham is exact in principle. Second, both methods are nonlinear and must be solved by serial iteration, though in many cases Kohn-Sham is more computationally efficient. Finally, a function to provide exact electronic exchange and correlation energies are unknown in both theories. Hartree-Fock provides for exact exchange energy, but neglects correlation entirely. The density functional treatment of electron-electron interaction is discussed in the next section.

### Electron-electron interaction energy

As with Hartree-Fock, the non-classical components of electronic energy, electron exchange and correlation, can be separated to two terms to be addressed separately:

$$E_{xc}[\rho^\alpha, \rho^\beta] = E_x[\rho^\alpha, \rho^\beta] + E_c[\rho^\alpha, \rho^\beta] \quad [2.1.38]$$

where the superscripts  $\alpha$  and  $\beta$  represent up and down spin. Further decomposition of Equation 2.1.38 to independently define  $\rho^\alpha$  and  $\rho^\beta$ , with parallels to Equation 2.1.31, the exchange energy can be closely approximated through spin density. Correlation energy, however, contains contributions from like and unlike spin electrons and is not so easily analysed<sup>58</sup>.

The local density approximation (LDA), local spin-density approximation (LSD), and generalized gradient approximation (GGA) are attempts to derive a density function to account for electron exchange and correlation energies. Conveniently, these approximations tend to underestimate exchange energy and overestimate correlation energy, cancelling the total error to a certain degree. Unlike Hartree-Fock, density functional approximations of  $E_{xc}$  introduce electron self-interaction error that must be excluded from the final result.

### 2.1.5 Methods used in this study

The theoretical results for molecular geometries and electronic structure included in the present work were completed using density functional theory through Gaussian 09 software<sup>63</sup>.



## Functionals

Due to the ongoing need for approximations to electron correlation and exchange, no single density functional is satisfactory in all cases, leading to the current state of the art in which the specific functional is chosen for a given calculation based on the atomic composition of the system in question.

Hybrid functionals combine weighted terms of one or more interaction energy approximations with the Hartree-Fock electron exchange term to best match experimental results<sup>64</sup>. These methods were developed by Becke and those noted by "B3" in the functional name represent the "Becke, 3 parameter" type. The three parameters determine the relative weighting of two exchange and one correlation mixing terms: DFT local spin-density approximation (LSDA) with Hartree-Fock exact exchange, LDA with a generalized gradient approximation (GGA, such as Becke88) exchange, and LDA with GGA correlation energy. It should be noted that optimizing the term coefficients by fitting to empirical observations makes them semiempirical parameters within the otherwise fully theoretical method.

### B3LYP

The B3LYP hybrid functional combines the Becke parametrized exchange energy with the Lee, Yang, and Parr correlation energy component<sup>64,65</sup>:

$$E_{XC} = E_{XC}^{LSDA} + a_0(E_x^{HF} - E_x^{LSDA}) + a_x(E_x^{B88} - E_x^{LSDA}) + a_c(E_c^{LYP} - E_c^{LSDA}) \quad [2.1.39]$$

where  $a_0 = 0.20$ ,  $a_x = 0.72$ , and  $a_c = 0.81$ .

This exchange-correlation functional is the most broadly used today due to its high accuracy of thermodynamic predictions (atomization energy, energy of formation, bond length, molecular geometry) for a broad range of salts and organic molecules. However, B3LYP, specifically its LYP correlation term, fails for metals and extended de-localized systems approaching the homogenous electron gas limit. An analysis of the B3LYP functional for metallic systems performed by Paier, Marsman, and Kresse demonstrated its limitations in that respect<sup>66</sup>.

### B3PW91

The B3LYP functional was preceded by and was modeled after B3PW91, the only difference being the correlation energy term. Although B3LYP has eclipsed B3PW91 for small molecules, the PW91 correlation function does not suffer from the particular limitations of LYP detailed above. For simulations containing regions of metallic or

extended delocalization character, B3PW91 is capable of greater accuracy than its later counterpart.

### **Basis sets**

As described in §2.1.2 the basis set composes the approximate wavefunction on which the functional acts to extract thermodynamic data. The quality of the basis set therefore in large part dictates the quality of the data. Two basis sets were used in the current work, 6-31G and Lanl2DZ: each explicitly models valence electronic wavefunctions but differ in their handling of core electron potentials<sup>67-69</sup>.

#### **6-31G**

The nomenclature of Pople-type split valence basis sets reads as X-ZYG where X is the number of gaussian primitive functions to model each core atomic orbital<sup>67</sup>. The two numbers Y and Z indicate a split-valence basis set where their sum is the number of primitives for each valence orbital. The two primitives differ in the value of  $\xi$ , the exponent in Equation 2.1.12 that defines the spatial extent of the orbital. By including a second function which permits a greater orbital volume, the optimization process is able to fit the extent of each orbital to the particular chemical environment under investigation. In the current case, the 6-31G basis set uses six gaussian functions for each core orbital plus four for each valence orbital: a three Gaussian contracted basis function using one value for  $\xi$  and a one Gaussian function using another. This allows for the production of a highly accurate wavefunction approximation although the computation time for optimization grows as  $\sim N^4$  for N explicitly modeled electrons.

#### **LANL2DZ**

The LANL2DZ basis set (Los Alamos National Laboratory 2 double- $\xi$ ) replaces explicit treatment of the core orbitals with an effective core potential (ECP). Since the core electrons of large atoms are not expected to be involved in bonding and these atoms contribute the most to computational cost, there is a time advantage to using an ECP-type basis set in these calculations.

An increasingly popular practice is to use mixed basis sets which allow a single calculation to make use of the strengths of each: main group elements treated explicitly with a Pople-type basis set and an ECP-type basis set for transition metals and high atomic number elements. Kryachko, Arbuznikov, and Hendrickx successfully applied such a mixed basis set method to model benzene-platinum complexes - a similar system to that currently under consideration<sup>70</sup>. The current work follows this trend by using the B3PW91 functional to treat a 6-31G basis set for organic structure and LANL2DZ for platinum and gold atoms.

### 2.1.6 Conclusion and outlook

The advances in knowledge made during the early decades of the 20th century, especially Schrödinger's wave equation, had profound effects on the practice and understanding of physical chemistry. Quantum methods permit the calculation of electronic energies which in turn allow for the calculation of system properties ranging from absorbance and emission spectra to molecular geometry and chemical reaction pathways. Density functional theory provides a means to compute sound and potentially exact solutions for quantum systems impossible through Schrödinger's original method. The range of functionals currently in use reflects the current need for approximation of the irreducibly quantum electron exchange and correlation energies. Even with these approximations, density functional methods can achieve accuracies within experimental error. As our models of quantum effects, as well as our computational capacity, continue to improve, so too will the power and benefit of density functional theory.

## 2.2 Ultraviolet/visible light spectroscopy

Measuring the absorbance of light in the ultraviolet and visible (UV/vis) band is a simple and accessible method for the identification of molecular species in solution and monitoring their changes over time.

### 2.2.1 UV/vis spectroscopy theory

To measure the wavelength-specific UV/visible light absorbance of molecules in solution, the sample is placed in the beam path between the radiation source, in this case deuterium arc ( $\lambda = 190\text{-}400\text{nm}$ ) and tungsten filament ( $\lambda = 300\text{-}2500\text{nm}$ ) lamps, and detector. Properly speaking, the intensity difference between the blank and sample spectra, or the transmittance, is measured by the spectrophotometer. The proportion of light not transmitted due to scattering interactions with sample molecules, known as absorbance, is related to transmittance as  $A = \log(T_0/T)$ . Light scattering by an organic molecule is determined by the HOMO-LUMO energy gap of non-bonding orbitals; the gap energy relates to a specific wavelength quantum mechanically (refer to §2.1.1). Where the light wavelength corresponds to an available energy gap in a sample molecule, the energy of that photon is absorbed to produce an excited electronic state in the molecule. A higher wavelength photon is subsequently released when the electronic state relaxes but not necessarily in the original direction, and is scattered.

Differences in electron density and chemical environment produce a specific absorbance per unit concentration for a given molecule,  $\epsilon$ , known as its extinction coefficient. This is the basis of the Beer-Lambert law<sup>71</sup>:

$$A = \ell \sum_i \varepsilon_i c_i \quad [ 2.2.1 ]$$

where the extinction coefficient of each molecule in the sample is multiplied by its molar concentration  $c$  over the path length through the solution  $\ell$  to arrive at the total absorbance.

### 2.2.2 Surface plasmon resonance

Metal nanoparticles may also scatter light in the UV/visible range due to coupling between the electromagnetic wavelength and the quantized oscillations of the metallic electron gas known as plasmons. The scattering cross section  $\sigma$  of an uncoated, spherical particle may be estimated as a function of its diameter  $d$  for a given wavelength  $\lambda$  in accordance with Mie's theory<sup>72</sup>:

$$\sigma = \frac{2\pi}{|\mathbf{k}|^2} (2L + 1) \text{Re}(a_L(d, \lambda) + b_L(d, \lambda)) \quad [ 2.2.2 ]$$

Where  $\mathbf{k} = 2\pi\sqrt{\varepsilon_m}/\lambda$  is the wavevector of the incident light in terms of the medium dielectric constant  $\varepsilon_m$  and wavelength  $L$ ;  $a_L$ , and  $b_L$  are terms of the Riccati-Bessel functions as described in Ref. 72. The diameter of gold nanoparticles from 5 to 120nm can be easily estimated based on their SPR peak through equations derived from Mie scattering theory. Unfortunately, for reasons that will be explained in §4.3.2, these relations are not applicable to the gold nanoparticles synthesized by the method presented in this study. The growth rate of the SPR amplitude observed by UV/vis spectroscopy is valuable nonetheless to monitor the nanoparticle formation process.

## 2.3 Small Angle Neutron Scattering

Electromagnetic spectroscopy is the typical choice for probing the nanoscale structure of materials; UV/visible light and X-ray spectroscopy were applied in the course of the present research. There are, however, limitations to photon-based methods in the study of polymeric structures, namely their low sensitivity to light elements and destructively high energy. Neutrons, an alternative probe beam particle, avoid these disadvantages while providing additional structure information through spectral analysis.

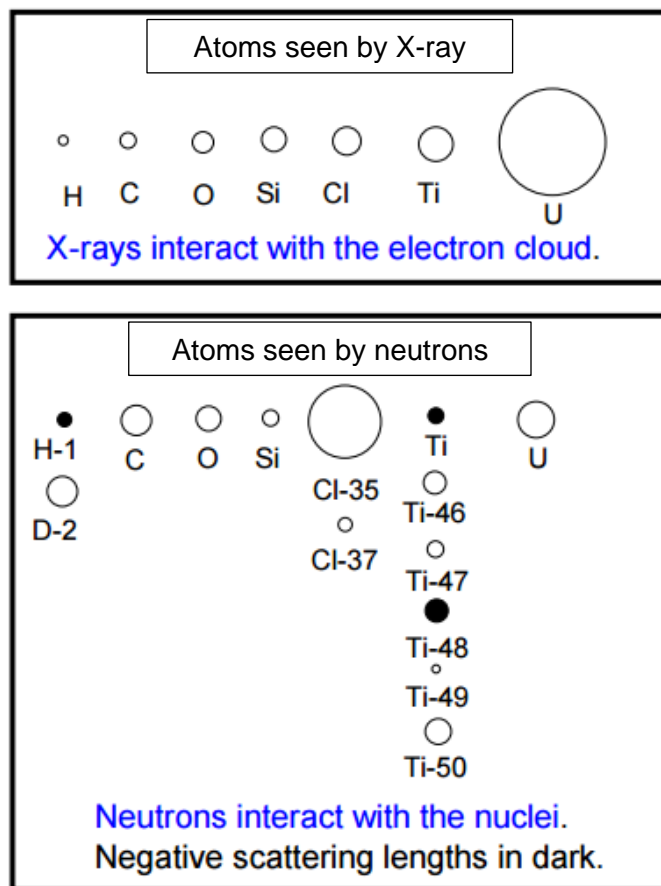
### 2.3.1 Neutron v. photon spectroscopy

First, while light interacts with the electrons of an atom, neutrons interact with the nucleus and so are insensitive to the conductivity, polarization, and magnetism of the material<sup>73</sup>. This also means that the scattering amplitude does not scale with the size of the electron cloud surrounding the atom, increasing the visibility of lighter elements<sup>74</sup>. Large variation in scattering length density (SLD) can also exist between isotopes, as seen in Figure 20. The difference between hydrogen and deuterium, for example, provides a simple method to differentiate the material or a section of the material under investigation from its background in solution<sup>75</sup>. In this study, contrast was achieved by dissolving hydrogenated polymers in D<sub>2</sub>O.

Second, the total energy of the beam relates to its wavelength according to  $E = hc/\lambda$  for massless particles and, by deBroglie's relation  $\lambda = h/mv$ ,  $E = mvc$  for particles with mass. However only the kinetic energy of the neutron is transferrable into the sample which relates to its wavelength by:

$$E_k = \left(\frac{h^2}{2m}\right) \frac{1}{\lambda^2} \quad [2.3.1]$$

So for neutrons with wavelength of 6Å, as were used in this study,  $E_k = 0.0027 \text{ eV}$  compared to an x-ray at the same wavelength whose kinetic energy is equal to its total energy,  $E_k = hc/\lambda = 2066.4 \text{ eV}$ , a  $\sim 10^6$  increase. Neutron scattering experiments can therefore achieve sub-nanometer resolution at significantly lower, and therefore less damaging, energies than their massless counterparts. Indeed one of the challenges of neutron spectroscopy is to increase the incident wavelength without sacrificing flux, as will be discussed in the following section.



**Fig. 20** Representation of x-ray v. neutron scattering cross-sections (Reproduced from <https://www.ncnr.nist.gov>)

### 2.3.2 Operation of the NIST CNR spectrometer

The neutron scattering experiments detailed below were all completed on the NC3 (now NC-B) 30 m small-angle neutron scattering (SANS) instrument at the NIST Center for Neutron Research (NCNR) located at the National Institute for Standards and Technology (NIST) campus in Gaithersburg, Maryland. The neutron source is a fission reactor that provides neutrons carrying 2 MeV kinetic energy<sup>76</sup>. These are too energetic and their corresponding wavelength too small for use and so are first collected through a moderator which reduces neutron energy to thermal levels by scattering against D<sub>2</sub>O held at 315 K. A second cold source chamber uses 20 K liquid hydrogen to further reduce neutron energy and achieve the desired wavelength.

Neutron cooling via scattering has the effect of reducing flux so that current scales with wavelength as  $1/\lambda^5$ .

Neutrons, like light, attenuate spherically and so the highest flux of any wavelength would be found closest to the source. To alleviate the crowding that this constraint might produce, guides lined with non-absorbing material maintain the current density through to the sample – 30 m away in this case. The guide also functions to resolve scattering angle  $\theta$  and wavelength  $\lambda$  of the beam through collimation and monochromation, respectively. Collimation is achieved by simple diaphragms clad in a neutron absorbing material such as cadmium spaced to shield the sample from bright areas of the beam tube as well as secondary neutrons produced by directly irradiated material. Monochromatic incident wavelength is also achieved through absorbance. Wavelength is resolved by passing the beam through two spinning disks each containing a window in an otherwise Cadmium clad surface. The polychromatic pulse passing through the first window will spread as the faster (shorter wavelength) outpace the slower (longer wavelength) neutrons. The phase of the second disk is timed to permit only the passage of the desired wavelength, now in a monochromatic pulsed beam.

### 2.3.3 Neutron scattering theory

Neutron scattering analytical methods capture structural information encoded in the neutron beam upon collision with sample nuclei. This process is completely analogous to electromagnetic diffraction and conforms to Bragg's law:

$$n\lambda = 2d \sin\left(\frac{\theta}{2}\right) \quad [ 2.3.2]$$

where  $n$  is any integer,  $d$  is the distance between scattering nuclei (more typically crystal layers), and  $\theta$  the scattering angle, revealing the rationale for sacrificing neutron flux for distinct, known values of  $\lambda$  and  $\theta$ .

A schematic of a neutron scattering experiment is shown in Fig. 21. The spectrum produced gives beam intensity intensity as a function of  $q$ , the difference in momentum between the incoming and outgoing particle<sup>73</sup>. More precisely,  $q$  is the absolute difference in wavevector  $\mathbf{k}$ , where

$$\mathbf{k} = \frac{2\pi}{\lambda} \quad [ 2.3.3]$$

in the direction of beam travel. We therefore may define the vector  $\mathbf{q}$  as

$$\mathbf{q} = \mathbf{k}_s - \mathbf{k}_i \quad [ 2.3.4]$$

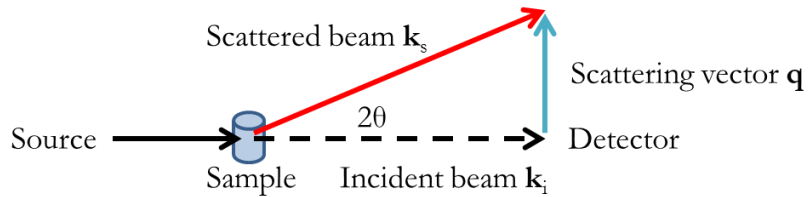
and so

$$q = |\mathbf{q}| = \frac{4\pi}{\lambda} \sin\left(\frac{\theta}{2}\right) \quad [ 2.3.5]$$

which can reduce to  $q = 2\pi\theta/\lambda$  at small values of  $\theta$  and the distance between scattering sites can be expressed in terms of  $q$  as

$$d = \frac{2n\pi}{q} \quad [ 2.3.6]$$

The distance between the sample and detector  $r$  can be varied to improve resolution over various ranges of  $q$ : the farther it is positioned the lesser the angle subtended. Longer detector distances will therefore provide greater resolution to larger sample structures (because  $q$  is inversely proportional to  $d$ ) although the experimental time interval  $\Delta t$  must be altered by  $\Delta t' = (r/r')\Delta t$  to compensate for flux density attenuation on the surface of the expanding sphere. The SANS experiments reported here were carried out at a sample-to-detector distance of 1.00, 6.00, and 13.00 m, corresponding to a scattering vector range of  $0.003 \leq q \leq 0.40 \text{ \AA}^{-1}$ .



**Fig. 21** A schematic representation of the relationships described in Equations 2.3.4 through 2.3.6.

Neutron scattering samples are not necessarily crystalline, and so a function relating spectrum intensity to  $q$  can reveal detailed structural information. The general form of this function is

$$I(\sigma, q) = f(\sigma)C(\sigma)P(q) \quad [ 2.3.7]$$



where  $f(\sigma)$  describes the nuclear scattering cross-sections and  $C(\sigma)$  the instrument-specific scattering profile, leaving the function  $P(q)$  that relates atomic arrangements within the sample to neutron scattering peaks.

### 2.3.4 Data reduction and analysis

Data reduction is the process of defining and stripping away instrument-specific information,  $C(\sigma)$ , from the scattering signal. Scattering data from blank sample cells are also collected and subtracted from the spectrum before structural analysis. For the SANS experiments reported in this work, data reduction was completed by the National Center for Neutron Research using Igor Macros package developed by NIST<sup>77</sup>.

A certain amount of precaution must be taken when undertaking to establish sample structure by fitting a form function  $P(q)$  to SANS data. The form functions are parametrized to account for the dimensions of scattering structures and so by granting too much freedom to the parameter values it is possible to fit a non-physical function to experimental data. When combined with other characterization methods, however, optimization of form factor parameters is a powerful tool for measuring the nanoscale dimensions of soft structures in solution. In the present case, the general shape of metal nanocrystals and their polymeric host is confirmed by transmission electron microscopy. SANS spectral analysis was performed by the author using the SasView 3.0.0 software.

Scattering length (SLD) is used to quantify the strength of neutron-nucleus interaction. A greater difference between the sample and its solvent produces a stronger contrast for analysis. For example, the high difference between hydrogen and deuterium noted earlier makes it possible to identify structural or dynamics information of organic materials in aqueous solution by deuterating one or the other. In the present case, contrast was achieved by dissolving the hydrogenated polymer in deuterium oxide. Scattering length is related to scattering cross section  $\sigma$  in the elastic limit as  $SLD = \sqrt{\sigma}/4\pi$ . SLD values for the materials used were taken from literature values<sup>74</sup> and are listed in Table 1.

**Table 1.** Neutron scattering length density for materials used in this study.

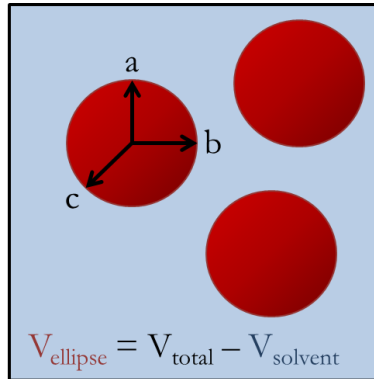
Material	Scattering length density ( $\text{\AA}^{-2}$ )
D <sub>2</sub> O	$6.38 \cdot 10^{-06}$
Poly(styrene-alt-maleic anhydride)	$1.87 \cdot 10^{-06}$
Platinum	$6.34 \cdot 10^{-06}$
Gold	$4.66 \cdot 10^{-06}$

TEM images of the precious metal nanocrystals show platinum as roughly spherical and gold as broad, flat disks. A triaxial ellipsoid form factor model was used because the radius of each axis is parametrized independently and can therefore accommodate spheres and disks and allow model consistency across samples<sup>78</sup>. The ellipsoid form factor is

$$P(q) = \frac{scale}{V_{ell}} \int_0^1 \int_0^1 \phi^2 \left\{ q \left[ a^2 \cos^2 \left( \frac{\pi x}{2} \right) + b \sin^2 \left( \frac{\pi x}{2} \right) (1 - y^2) + c^2 y^2 \right] \right\} dx dy \quad [2.3.8]$$

where  $scale/V_{ell}$  is a scaling factor defined by the fractional volume of the sample contained by the ellipses;  $a$ ,  $b$ , and  $c$  are the radii of the three axes where  $a \leq b \leq c$  (Fig. 22); and assuming random orientation of anisotropic ellipsoids in solution,  $\phi$  takes the average against the detector plane (x,y) by

$$\phi^2(x) = 9 \left( \frac{\sin x - x \cos x}{x^3} \right)^2 \quad [2.3.9]$$



**Fig. 22** Schematic of elliptical shapes that could produce a SANS spectra described by Equation 2.3.8.

The polymeric nanoarchitecture appeared laminar in TEM images; without access to a side-view the more general paracrystalline laminar form factor was used<sup>79</sup>. This model is able to account for scattering from a repeating stack of lamellae, if present, along with allowance for Gaussian polydispersity. Scattering intensity is given as a function of  $q$

$$P(q) = 2\pi\Delta\rho_m^2\Gamma_m \frac{P_{bil}(q)}{q^2} Z_n(q) \quad [2.3.10]$$

where  $\Delta\rho_m$  is the difference in scattering lengths between the laminar material and its solvent per unit of lamina mass;  $\Gamma_m$  is the mass per unit area of bilayer;  $Z_n(q)$  accounts for scattering from  $n$  stacked bilayers, and the laminar bilayer form factor is given by

$$P_{bil}(q) = \left( \frac{\sin(q t/2)}{q t/2} \right)^2 \quad [ 2.3.11 ]$$

which is a function of layer thickness  $t$  as well as  $q$ , assuming an infinitely large sheet.

For sample systems containing a mixture of laminar and ellipsoid structures, the above models were applied in linear combination scaled to match their respective contribution to the final scattering spectrum.

## 2.4 Electron microscopy

Human vision is sensitive to a narrow band of the electromagnetic spectrum from approximately 750nm to 400nm. Despite this, scattering and diffraction methods have extended the resolution limit of optical microscopy below 100nm. Smaller structures scatter light by the same mechanism as larger ones, except that their characteristic colours are composed of smaller wavelengths. We could theoretically focus a beam of small-wavelength light onto the nanostructure of interest and use suitable detectors to record and transform the resulting image into our visible spectrum, but as was detailed in §2.2.1 light in those wavelengths is energetic enough to break chemical bonds and destroy the subject of the portrait. In this case the answer is also to substitute a high energy photon with a massive particle.

### 2.4.1 Scanning electron microscopy (SEM)

Like neutrons, electrons hold a rest mass that binds a significant portion of their total energy, making their kinetic energy at a given wavelength much smaller, and therefore less damaging, than their photonic counterparts. Electrons are much more convenient than neutrons: because it requires less energy to free an electron than it does a neutron, an electron source housed in a benchtop unit can produce higher flux than a fission reactor can for neutrons.

Other advantages of electrons for imaging are the same that made them unsuitable for the scattering experiments described above. Firstly, electronic charge and spin permit them to be focussed by electrostatic and magnetic lenses. Secondly, image formation is dependent on interaction with the electronic orbitals of atoms in the sample, rather than the nuclei.

Scanning electron microscopes construct an image the sample surface by moving the beam across the surface in raster progression, recording one unit area of minimum resolution at a time<sup>80</sup>. The most common detector senses secondary electron emission: electrons emitted after excitation by interaction with the incident beam. The work function of the surface must be accessibly low for secondary electrons to be produced, thus dielectric materials are unsuitable for imaging by SEM. Biological samples are often first prepared by coating with gold.

Another detector may be placed to capture elastically-scattered primary electrons, a condition more likely for those that interact with large, high electron density atoms. Backscattering, as the effect is known, is therefore able to detect different metals in a sample. In combination with SEI, backscattering data can map the surface according to its surface material as well as topology for a richer image – one having hue as well as contrast.

Incident electron interactions also result in the emission of secondary x-rays by one of two processes. First, if the electron beam displaces a core electron in a sample atom, one or more electrons in higher orbitals will release a photon of energy equivalent to the difference in orbital energies. These values are characteristic and can be used to quantitatively ascertain the identities and prevalence of elements in the target area<sup>81</sup>. As with BSE, Energy dispersive x-ray analysis (EDAX) can also be mapped to the SEI image to correlate elemental data to location. Second, if the incident electron is inelastically scattered by slowing down due to the attraction of a nearby atom, it will emit an x-ray to shed energy around the curve, an effect known as bremsstrahlung. The random nature of low-energy bremsstrahlung emissions means that it is a source of noise rather than image information.

The SEI micrographs and EDAX spectra included in this work were produced with a Philips XL30 or FEI Quanta 250 SEM (Figure 31 only), both at RMCC with the assistance of Dr. Jennifer Snelgrove.

#### **2.4.2 Transmission electron microscopy**

As the name implies, the image is formed by the shadow cast by the sample as the primary electron beam is transmitted through the sample and onto the detector. As such, feature contrast is defined by sample thickness and electron scattering cross section rather than topology and work function. In this sense, the Beer-Lambert law (§2.2.1) is a good first-order approximation of the transmitted intensity at a given point<sup>80</sup>. TEM from 80-300 KeV produce electron probe beam wavelengths from 4.33-2.24 pm which may be focused to resolve sub-nanometer structures in thin films<sup>82</sup>.

Furthermore, phase shift between directly transmitted and diffracted electrons can affect the image formed according to Bragg's law. High resolution (HR) TEM

captures these intensity variations to produce images of objects as small as single atoms in a crystal plane normal to the incident beam.

### Selected area electron diffraction

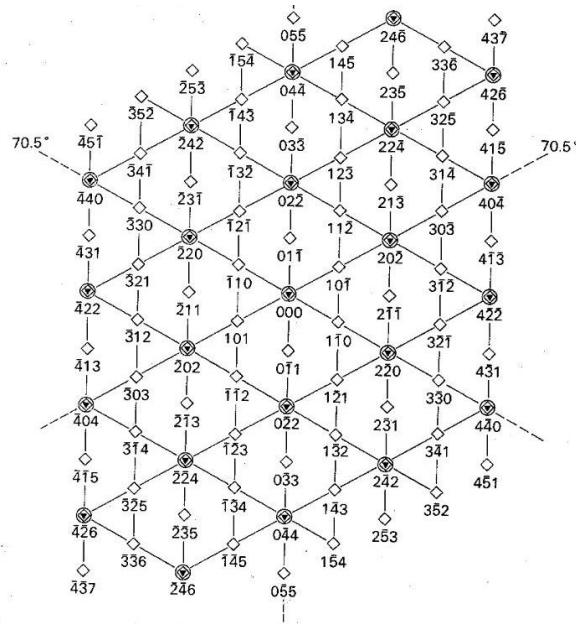
Taking the image at the back focal plane will instead produce a 2D diffraction pattern in radial reciprocal space by electron phase interference, *i.e.* points of high intensity are measured as 1/distance from the centre of the beam. The selected area electron diffraction (SAED) pattern can be interpreted according to standard crystallographic practice<sup>80</sup>. Single crystals produce points at distances and relative angles according to their interplanar distances and crystal structure. The results for permitted planes in each crystal structure have been tabulated and mapped. The relevant Miller indexed diffraction pattern maps for the (111) face centred cubic plane and the (0001) hexagonal close packed crystals are shown in Figures 17 and 18, respectively. Although hexagonal crystal patterns use a four character index, the **i** direction in {**hkil**} carries no extra information since **i** = **-(h+k)**. Miller indexed formulae to calculate the interplanar distances for the crystal patterns used in the current work are face-centred cubic:

$$d_{\{hkl\}} = \frac{a}{\sqrt{h^2 + k^2 + l^2}} \quad [ 2.4.1 ]$$

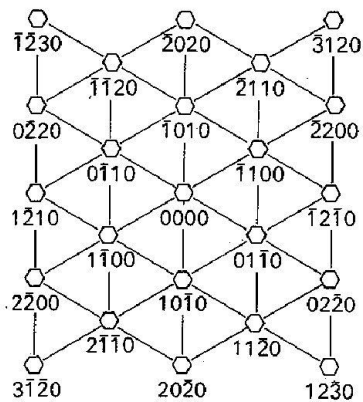
and hexagonal close packed:

$$d_{\{hkl\}} = \frac{1}{\sqrt{(4/3)[(h^2 + hk + k^2)/a^2] + (l/c)^2}} \quad [ 2.4.2 ]$$

where *d* is the interplanar distance and *a* and *c* are lattice constants. The locations of permitted peaks for each crystal structure have been tabulated and mapped as shown in Figures 23 and 24. Analysis of an SAED image therefore consists of matching the pattern and confirming the experimentally measured *d*-spacings against the calculated values<sup>80</sup>.



**Fig. 23** Map of electron diffraction points of the (111) crystal plane for face centred cubic (black triangles), diamond (diamonds), and body centred cubic (circles). Reprinted from Ref. 80.



**Fig. 24** Map of Miller indexed electron diffraction points for hexagonal close packed crystal structure. Reprinted from Ref. 80.

## 3 The SMA polymer template

Portions of this section were originally published as: McTaggart, M., Jugroot, M., Malardier-Jugroot, C. (2015). Self-assembled biomimetic nanoreactors I: Polymeric template. *Chem. Phys. Lett.* **636**, 216-220 (2015). doi: 10.1016/j.cplett.2015.08.014

*M.R.M. designed and performed the experiments and prepared the manuscript.*

### 3.1 Introduction

Some of the most exciting innovations of recent decades relate to molecular self-assembly and supramolecular catalysis<sup>83–85</sup>. Biomimicry is an attractive approach to dynamic nanomaterials given the ubiquity of stable, self-assembling nanoreactors in nature, yet the design and control of such materials for industrial use remains a formidable challenge<sup>85–88</sup>. Broadly speaking, mimicry is attempted either by replicating natural structures<sup>89</sup> or by reproducing the physical and chemical properties of the system by other means<sup>3</sup>. Given the sensitivity of bioreactors to harsh environmental conditions, the latter approach may permit the synthesis of robust analogues for application outside of biological pH, temperature, or ionic concentrations<sup>90</sup>.

Enzymes generate extremely high reaction rates partly by the concerted action of two complementary effects: catalysis and confinement. Biological catalysis consists of the forced geometric arrangement of substrates into relative position that minimizes activation energy. This is accomplished by the placement of complementary amino acids to bind intermediate reaction structures, the ‘lock and key’ of enzymatic catalysis, and, in cases of redox reactions, co-ordination with a metal centre<sup>91</sup>. In aqueous media, the confinement effect refers to the autonomous increase in effective molarity and compression of non-polar molecules within a nanoscale hydrophobic domain<sup>3</sup>. Increased substrate concentration at the reactive site increases electron density and reduces the entropic cost of reaction, resulting in an increased rate of reaction.

The material used for the development of a biomimetic system is poly(styrene-alt-maleic acid) (SMA). SMA is an alternating, amphiphilic copolymer whose chains self-assemble into a pH sensitive cylindrical micelle nanostructure in aqueous solution at neutral pH. Dynamic light scattering (DLS) in aqueous solution revealed that the hydrodynamic radius of the SMA association presented a maximum at pH 6.5; the size of the association is reduced as pH rises or falls<sup>41</sup>. This pH corresponds to the monodeprotonated form of the diacid which theoretical models showed to produce a linear chain conformation at pH 6.5 that does not appear at pH 3 or 12<sup>40</sup>. Individual chains then associate by  $\pi$ - $\pi$  interaction to form dynamic supramolecular nanotubes with 14 Å interior and 21 Å exterior radii<sup>92</sup>. The nanotubes were also found to be

insensitive to temperature variation between 15° and 75°C and to ionic strength at polymer to salt concentrations below 1/80<sup>42</sup>.

The hydrophobic interior of the SMA nanotubes was found to be capable of exploiting the confinement effect to promote otherwise unfavourable reactions. Indeed, pyrrole in 1% w/w SMA solution was observed to preferentially concentrate within the SMA nanostructure and spontaneously polymerize. Extensive investigation determined that the confined dimensions reduced pyrrole dynamics such that the reaction thermodynamics permitted thermal initiation<sup>44</sup>.

The importance of the polymer molecular weight on the nanoarchitecture is known to allow tuning of the thickness and stability of self-assembled block copolymers<sup>93</sup>. The importance of this factor on the self-assembly of the alternating copolymer, SMA, has however only been studied over a very narrow molecular weight range (1,600 - 40,000) and no change in nanostructure was observed<sup>41</sup>. Here, we present the in situ characterization using small angle neutron scattering and transmission electron microscopy of a novel nanostructure obtained by self-assembly at pH 7 of the pH sensitive alternating copolymer with a high molecular weight of 350,000. Molecular modeling was also performed to provide precise information on the atomic level polymeric structure. The nanoarchitecture provides a hydrophobic cavity optimal for confinement effect as observed in biological systems and is a very good candidate template for the synthesis of biomimetic nanoreactors.

## 3.2 Experimental

Poly(styrene-*alt*-maleic acid) sodium salt solution, 13% wt in H<sub>2</sub>O, 350 kDa average molecular weight (SMA, Sigma-Aldrich) was freeze dried and rehydrated according to each sample specification. Small angle neutron scattering (SANS) experiments were performed on the NG3 30 m Small-Angle Neutron Scattering instrument at the NIST Center for Neutron Research, Gaithersburg, MD. The incident wavelength ( $\lambda$ ) used during the experiments was 6 Å. The SANS experiments were carried out at a sample-to-detector distance of 1.00, 6.00, and 13.00 m, corresponding to a scattering vector range of  $0.003 \leq q \leq 0.40 \text{ \AA}^{-1}$  [ $q = (4\pi/\lambda) \sin(\theta/2)$ ]. The samples were loaded in quartz cells with a sample aperture of  $10 \times 10$  mm. To maximize the contrast between the polymer and the solvent, the polymer used was hydrogenated and prepared in deuterated water solution. The spectra obtained were corrected for electronic background and empty cell. The data were reduced at the NIST Center for Neutron Research using Igor Macros package developed by the NIST Center for Neutron Research. Analysis of the reduced data was performed using SasView 3.0.0 (<http://www.sasview.org>). The selected model is detailed in Section 3.3. The morphology of the polymeric template was studied by



Transmission Electron Microscopy (TEM) Experiments on a high resolution FEI HR-TEM/STEM Titan 80-300LB microscope operating at 300 kV. Solution samples were stained on carbon-coated copper grids and allowed to air dry. Molecular modeling was completed using Gaussian 09 software<sup>63</sup>.

### 3.3 Results and Discussion

A combination of molecular simulation and experimental characterization is critical to bridge the length scale needed for a complete structural characterization of nanostructures. The approach detailed herein allowed the characterization of polymeric templates to understand and improve the kinetics of reactions occurring within the confined environment of the nanoreactors.

The self-assembly of polymers can be characterized by different experimental methods ranging from dynamic light scattering for average large scale information on the hydrodynamic radius of the association, to very precise imaging methods such as transmission electron microscopy or atomic force microscopy usually performed with the polymer interacting with a surface and often in a dry state<sup>45,94</sup>. Small angle neutron scattering (SANS) provides a unique approach for the investigation of the association of polymers in solution because this method allows for characterization in solution. A very high contrast between the deuterated solvent and the hydrogenated polymer allows a precise form factor for the nanoarchitecture to be fitted with characteristic models to precisely determine its shape and uniformity. The pH sensitivity as well as the structure of the self-assembled structure of SMA with a low molecular weight were previously characterized by SANS<sup>41</sup>. A concentration dependent characteristic scattering peak was observed in the SANS spectra between 0.05 Å<sup>-1</sup> and 0.18 Å<sup>-1</sup> due to the nanotube structure of the self-assembled polymer in its low molecular weight range.

The high molecular weight polymeric samples used in this study were also analyzed by SANS. Information concerning the structures present in a SANS spectra is interpreted through the application of model form factors,  $P(q)$ , whose shape parameters are optimized by least-squares fit to the intensity curve. Indeed, the differential scattering cross section per unit volume can be given by the equation:

$$\frac{d\Sigma(q)}{d\Omega} = n_p P(q) \quad [ 3.3.1 ]$$

where  $n_p$  is the number density of particles and  $P(q)$  is the particle form factor.

The SANS spectrum obtained for the high molecular weight polymer at pH7 did not produce the characteristic peak for hollow cylinders that had been seen in low

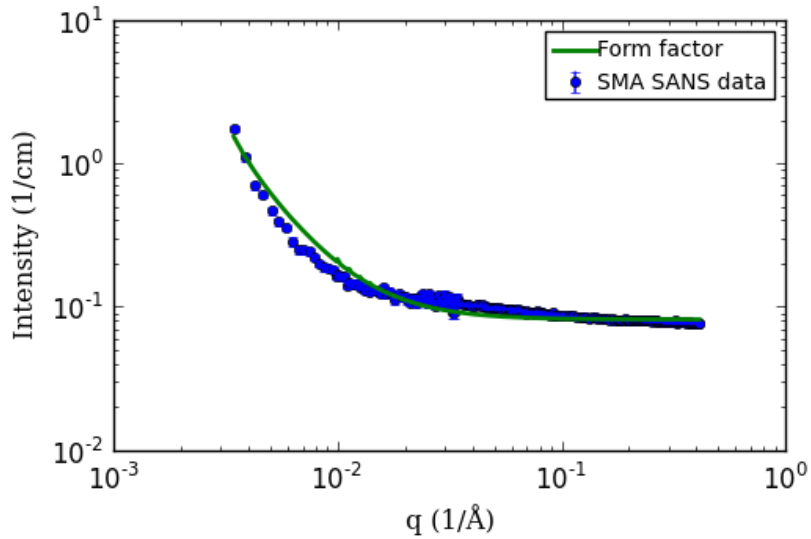
molecular weight samples. Several form factors including those for solid and hollow cylinders and rectangles were tested for fit against the spectra obtained for the high molecular weight polymer at pH7; the model that best fit the low intensity spectra with physically reasonable parameters is a stack of crystalline bi-layer lamella described by:

$$I(q) = 2\pi(\Delta\rho_m)^2\Gamma_m \frac{P_{bil}(q)}{q^2} Z_n(q) \quad [ 3.3.2 ]$$

where  $\Delta\rho_m$  is the difference in scattering lengths between the laminar material and its solvent per unit mass;  $\Gamma_m$  is the mass per unit area of bi-layer; scattering by a bi-layer of thickness  $t$  is approximated as:

$$P_{bil}(q) = \left( \frac{\sin\left(\frac{qt}{2}\right)}{\frac{qt}{2}} \right)^2 \quad [ 3.3.3 ]$$

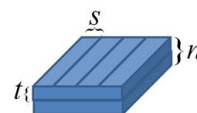
and  $Z_n(q)$  accounts for the interference of  $n$  layers. The fit to the experimental data is shown in Figure 25 and the parameters obtained from curve fitting are presented in Table 2.



**Fig. 25** Crystalline lamella model (line) fitted to SANS data of 1% SMA, pH 7.

**Table 2.** SANS model fitting parameters.

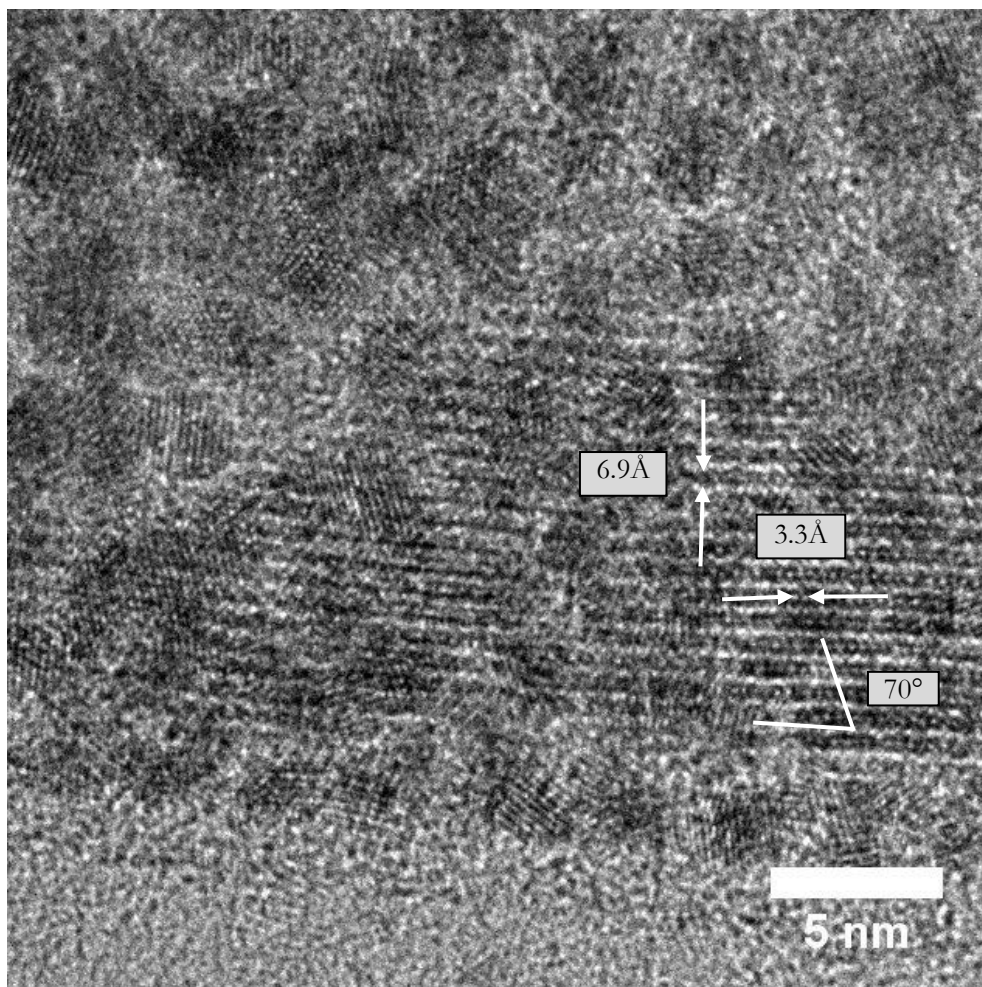
Parameter	SMA pH 7
SLD <sub>solid</sub> (Å <sup>-2</sup> )	1.87e-06
SLD <sub>solv</sub> (Å <sup>-2</sup> )	6.38e-06
Spacing $s$ (Å)	6.99
Thickness $t$ (Å)	12.34
Layers $n$ (N)	1.00
Quality of fit ( $\chi^2/n$ )	37.1



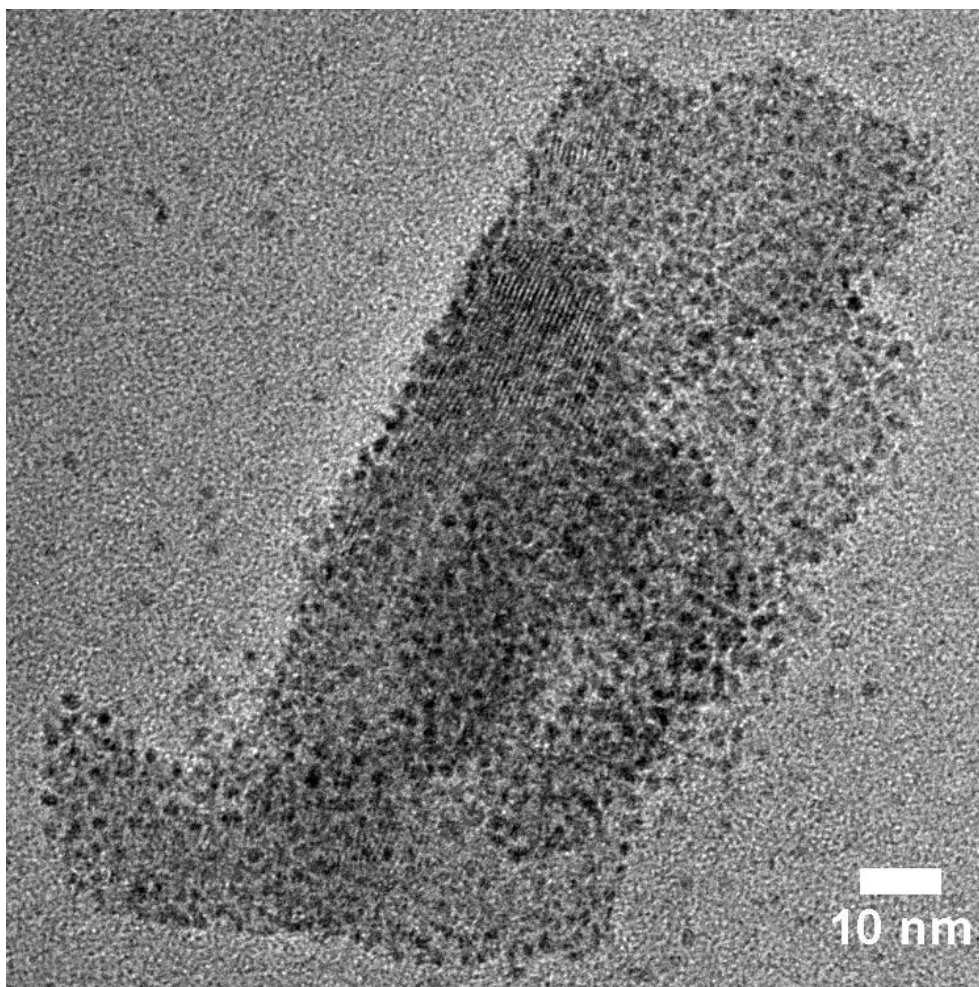
Low signal intensity is expected for very thin lamellar systems and impacts quality of fit, but as shown in Figure 25 a bi-layer laminar model adequately fits the 1% SMA experimental data. The model was optimized with a chain spacing of 7.0 Å, thickness of 12.3 Å and one bi-layer. This would provide a hydrophobic cavity inside the hydrophobic layer of about 2nm. The lamina model was also employed in subsequent SANS experiments of SMA-metal systems whose higher intensity signal further justified the choice of a bi-layer form factor (see §4.3).

Images of organic polymers by HR-TEM are not normally visible due to burn off by the intense electron beam. Fortunately in this case, the polymer nanostructures were very stable and observed on images of samples regardless of metal precursor or pH. Figure 26 clearly shows the SMA nanostructure in a sample prepared at pH 7; the parallel lines are individual SMA polymer chains organized into a sheet by the  $\pi$ - $\pi$  interactions observed at regular intervals between them. The spacing of the chains is 6.9, s.d.= 0.8 Å, the distance between sets of  $\pi$ - $\pi$  interactions 3.3, s.d.= 0.8 Å, and their progression angle relative to the polymer backbone is  $76 \pm 4^\circ$ .

The polymer shown contains embedded platinum nanoparticles, appearing as out-of-focus dark patches, synthesized according to the method described by Groves<sup>45</sup>. The beam was held in place for several minutes before the polymer disintegrated to reveal the platinum nanoclusters within, demonstrating the stability of the SMA-Pt system. Figure 27 provides an example of SMA organization at pH 5 shown at a larger scale. The polymer nanostructure remains plainly visible, demonstrating the pH stability of the SMA-Pt system.



**Fig. 26** Close up of TEM image, SMA-Pt system at pH 7 showing SMA supramolecular association into a bi-layer nanosheet. Regularly spaced points between chains indicate  $\pi$ - $\pi$  interactions.



**Fig. 27** TEM image of SMA-Pt system showing Pt nanocluster confinement to SMA sheets and their top-level organization. Scale bar is 10 nm.

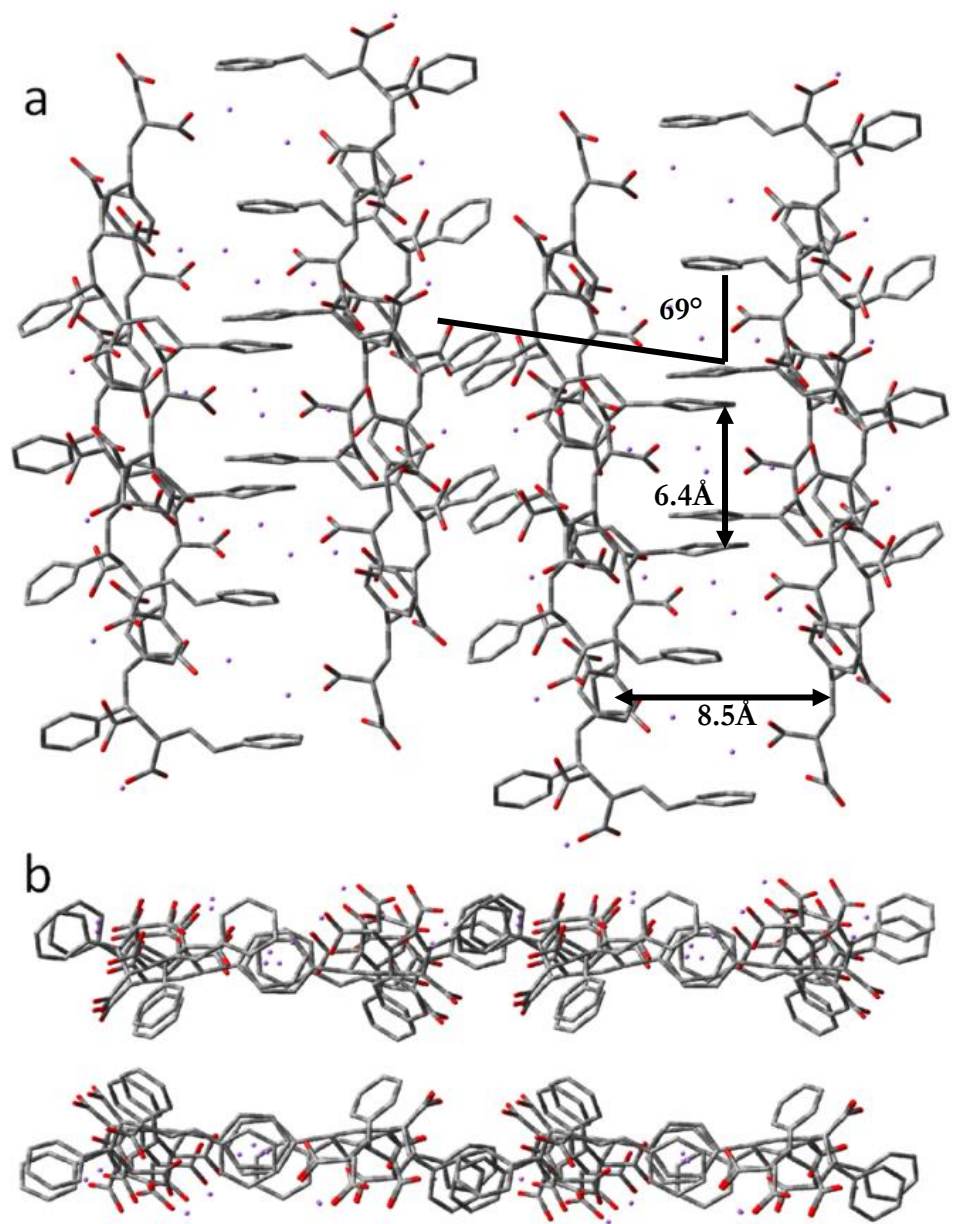
The pH dependence of the association of the low-molecular weight SMA was successfully predicted by molecular simulation in previous work which also explained the thermodynamically favoured association only at pH 7<sup>92</sup>. Specifically, the hydrolysis of one acid group at pH 7 provides the opportunity for very strong intramolecular hydrogen bonding to give a rigid, linear conformation to the polymer. This linearity favours the self-association of the chains by removing the otherwise high entropic cost that prevents association. It was shown for low molecular weight polymers that the association of eight polymer chains forms a nanotube with an internal diameter of  $\sim 3$  nm. Individual chains had been fully optimized using Density Functional Theory

(DFT) with the combination of functional/basis set B3LYP/6-31G. A conformational search as described in the literature was performed to ensure the optimization of the ground state on the polymer chain and to predict its thermodynamic behaviour<sup>92</sup>.

Using the same linear structure proven to be the most stable for individual polymer chains at pH 7, the self-assembly of the SMA chains was modelled as a supramolecular sheet. As shown in Figure 28, the association among optimized chains occurs with interaction between neighbouring styrene rings.

The chirality of the monoprotonated SMA polymer, determined by the direction of the styrene groups' progressive rotation along the chain, has been noted previously<sup>92</sup>. In the present predicted conformation, not only must the chains run antiparallel to form a single sheet, but also the chains composing paired sheets must be antichiral to one another. This structure demands a very high level of organization. The  $\pi$ - $\pi$  interactions between the styrene groups of two polymer chains are observed every 11.7 Å. Staggering two SMA sheets will place the separation between the  $\pi$ - $\pi$  interactions from the top-down view at 6.4 Å intervals. SMA chains of the top and bottom sheets coincide and are spaced 8.5 Å apart. Due to styrene rotation the line of bonds are not perpendicular to the chains but progresses, as illustrated in Figure 28a, at approximately 69° to the polymer backbone. Figure 28b reveals the primarily hydrophobic interior and hydrophilic exterior of the polymeric bi-layer. All of the above measurements closely correspond to those observed in TEM images.

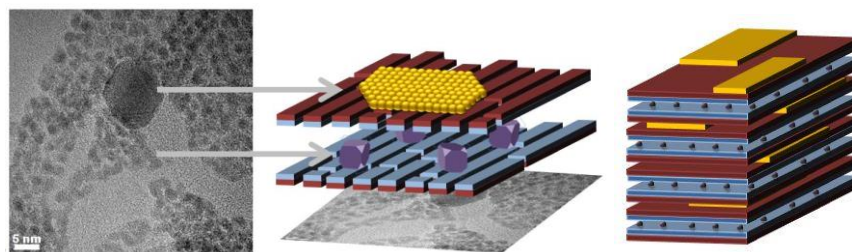
Hence, this careful characterization of the association of SMA chains in aqueous environment shows that the individual chain conformation remains the same as that observed in previous studies of SMA self-assembly but the supramolecular structure has changed from nanotube to nanosheet. The difference lies in the molar mass, with low molecular weight polymers favouring tubular nanostructures and high molecular weight polymers favouring nanosheet conformation<sup>41,42,92</sup>.



**Fig. 28** Bi-layer model of SMA. a) The top-down view, chains are aligned by  $\pi$ - $\pi$  bonding between styrene groups. b) the side view, hydrophilic groups (oxygen shown in red) are concentrated on the exterior surface, hydrophobic styrene groups to the interior.

### 3.4 Conclusion

The theoretical and experimental results provide evidence of a novel poly(styrene-alt-maleic acid) nanoarchitecture that self-assembles by  $\pi$ - $\pi$  interactions into highly organized lamina containing confined cavities. This result introduces tunability of the SMA superstructure for fine control over the dimensionality of its confined domains. The laminar structure is an ideal template for the synthesis of unsupported nanoreactors, as illustrated in Figure 29, due to the expected presence of both hydrophobic and hydrophilic confinement spaces located within and between the bilayers, respectively. This nanostructure opens new opportunities for the development of nanoreactors with different active centres, as well as possibilities for controlled reactions within hydrophilic and hydrophobic cavities of a single nanoreactor.



**Fig. 29** Schematic representation of the unsupported polymeric nanoreactor in aqueous environment. The tailored nanoreactors can contain hydrophilic (blue) or hydrophobic (green) active centers or a combination of hydrophilic and hydrophobic active centers. The size of the active center cavity is approximately 2nm.



## 4 Noble metal active centres

Portions of this section were originally published as: McTaggart, M., Jugroot, M., Malardier-Jugroot, C. Self-assembled biomimetic nanoreactors II: Noble metal active centres. *Chem. Phys. Lett.* **636**, 221-227 (2015). doi:10.1016/j.cplett.2015.08.015

*M.R.M. designed and performed the experiments and prepared the manuscript.*

### 4.1 Introduction

It was recently demonstrated that the hydrophobic salt platinum(II) chloride will reduce to platinum nanoclusters under 3 nm in dimension inside the SMA nanostructure without additional reducing agents<sup>45</sup>. The polymer-supported metal nanoparticles are well dispersed and stable in the aqueous solvent. This stability in aqueous environments represents a significant advantage over the colloidal approach which typically results in the precipitation of the nanocrystal-ligand complex due to its reducing agent<sup>45</sup>.

Herein we report the theoretical and experimental characterization of the structure, stability, and pH sensitivity of SMA-platinum and SMA-gold nanoreactors. First, metal nanocrystal growth was measured by UV/Vis spectroscopy, which revealed a difference in reaction rate and the crucial role of the polymer-metal interaction in the growth mechanism. Then the electronic interactions of the metal atoms with the SMA polymer were modeled by quantum mechanical methods. The nanostructures of the gold and platinum systems were investigated by transmission electron microscopy, the latter at different pH levels, and in situ by small-angle neutron scattering. These nanoreactors are obtained using a facile and environmentally friendly reaction path and produce very stable systems combining, like their biological counterpart, the effect of confinement with high catalytic efficiency. In addition, this study presents the first successful synthesis of stable, dispersible, atomically thin gold nanosheets.

### 4.2 Experimental

Poly(styrene-alt-maleic acid) sodium salt solution, 13% wt in H<sub>2</sub>O, 350 kDa average molecular weight (SMA, Sigma-Aldrich) was freeze dried and rehydrated according to each sample specification. Gold(I) chloride (AuCl, 99.9%, Sigma-Aldrich) and platinum(II) chloride (PtCl<sub>2</sub>, 98%, Sigma-Aldrich) were used as received. Unless otherwise specified, the synthesis method was common to all metal salt precursors. Dehydrated SMA polymer was added to 3mL of DI water and HCl or NaOH added to achieve a 1% wt/wt solution at pH 7 or, in the case of small-angle neutron scattering samples, D<sub>2</sub>O, DCl, and NaOD. Hydrophobic metal salts were then added to a 1:1 molar ratio between metal atoms and SMA monomers. Mixing was completed

by sonication for 0.5-1.5 hours. UV-visible light spectroscopy was carried out in a 1mm quartz cuvette in an Agilent 8453 PDA spectrometer and analyzed with ChemStation software v.B.04.02. Small angle neutron scattering (SANS) experiments were performed on the NG3 30 m Small-Angle Neutron Scattering instrument at the NIST Center for Neutron Research, Gaithersburg, MD, as detailed in §3.2. The selected models for each spectrum obtained are detailed in the results and discussion section. The morphology of the metal particles was also studied by transmission electron microscopy (TEM) on a high resolution FEI HR-TEM/STEM Titan 80-300LB microscope operating at 300 kV.

Molecular modeling was completed using Gaussian 09 software<sup>63</sup>. Interactions between platinum atoms and the SMA trimer employed a 3-part ONIOM model<sup>95</sup>. The outer monomers were included at the PM6 level to simulate the immediate chemical environment without high computational cost<sup>96</sup>. The central monomer and metal atoms were modeled by density functional theory using the B3PW91 hybrid functional<sup>64,97,98</sup> with the 6-31G basis set for the main group elements and LanL2DZ for platinum and gold, the latter with double- $\zeta$  type effective core pseudopotentials<sup>68</sup>. This arrangement has been shown to provide high quality results for simulating transition metal interactions with oxygen and benzene complexes<sup>70,99,100</sup>.

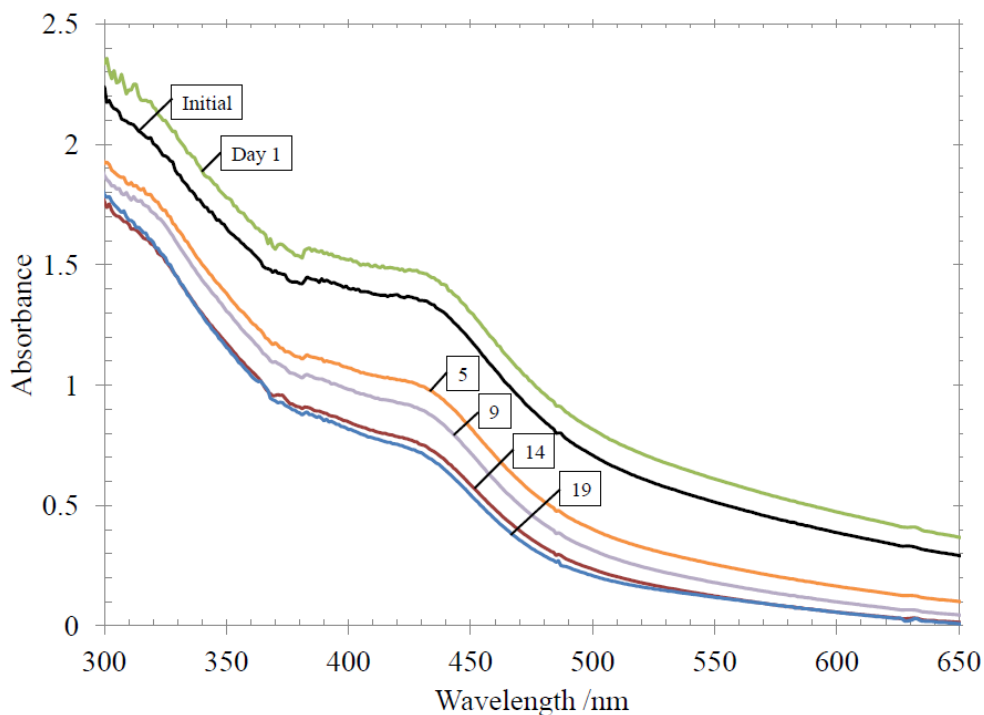
## 4.3 Results and Discussion

### 4.3.1 Platinum

As discussed in the introduction, to develop efficient and tailored nanoreactors that mimic biosystems, it is important to control the nature and the shape of the active centers to optimize their surface area and catalytic efficiency<sup>101</sup>.

#### UV/vis spectroscopy

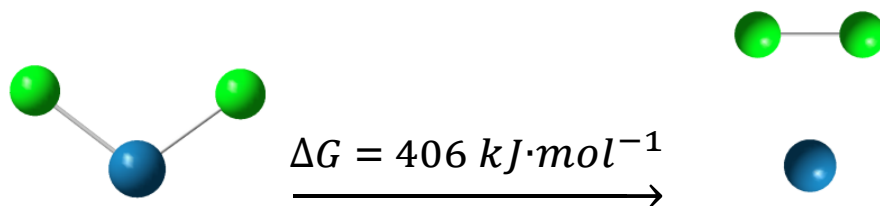
In the current study, nanocluster synthesis was monitored by UV/visible light spectroscopy over 19 days to follow the reduction process of PtCl<sub>2</sub> inside the confined environment of the polymeric template. The characteristic plasmon peak for platinum at 215 nm was hidden in the SMA absorption range so platinum reduction into nanoclusters was observed qualitatively by a change in solution colour from yellow to brown to black, shown in the spectra series of Figure 30 as the dissipation of the shoulder at 430nm<sup>102-104</sup>. Completion of the synthetic process was indicated by stabilization of the signal after 14 days.



**Fig. 30** UV/vis spectra of PtCl<sub>2</sub> added in 1:1 proportion to SMA monomers in 1% wt/wt SMA solution. Shoulder centred at 430 nm diminishes over time.

### DFT modeling

Platinum nanocrystals were previously observed at pH 7 embedded in the polymer matrix suggesting that the platinum salt used for their synthesis concentrates within SMA prior to its reduction<sup>45</sup>. It is important, therefore, to understand the metal-polymer interactions since these determine whether the metal crystal growth is more likely to occur under confinement in the hydrophobic interior or on the hydrophilic exterior of the SMA nanostructure. Despite the evidence of reductant-free nanocrystal formation, reduction of platinum(II) chloride to platinum(0) is not a spontaneous reaction. The Gibbs free energy of the platinum-chloride dissociation was calculated to be 406 kJ·mol<sup>-1</sup> by DFT - B3PW91/LANL2DZ. The reaction schematic is shown in Fig. 31. While the production of chlorine gas molecules makes the reaction entropy favourable, it is not enough to overcome the enthalpic requirement. This explains why a strong reducing agent such as sodium borohydride is typically required.



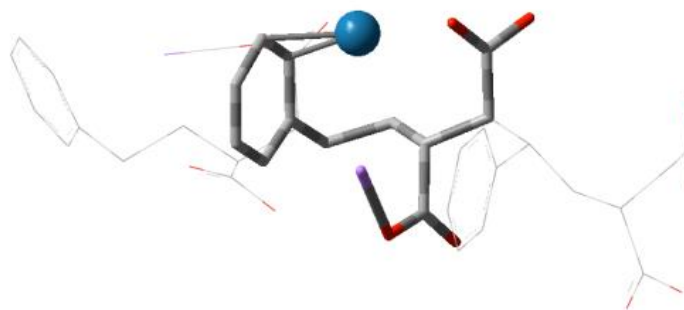
**Fig. 31** Dissociation of chlorine (green) from platinum (blue) leads to the reduction of the platinum atom and the production of one chlorine gas molecule.

When the reduced platinum atom is placed at equal distance from the styrene and carboxylic acid moieties of the SMA monomer in DFT simulation, it follows the slope in the energy surface towards the styrene and forms bonds across two carbons of the ring; Figure 32 shows its final geometry (hydrogen removed for clarity).

The metal-polymer bonding energy is calculated by the difference between the total system energy:

$$E_{bond} = E_{SMA-Metal} - (E_{SMA} + E_{Metal}) \quad [4.3.1]$$

Bonding energy of the SMA-platinum bond shown in Figure 32 is 2.64 eV (254.7 kJ·mol<sup>-1</sup>). The stability of the styrene-platinum bond suggests that this is the nucleation site for nanocrystal formation. The location of the platinum nanoclusters within SMA's hydrophobic interior is in keeping with their 3 nm growth limit and catalytic effect on pyrrole polymerization. Simulations also show that the inclusion of the metal atom does not alter the linearity of the SMA polymer chain and should therefore leave the self-assembled nanoarchitecture formed by SMA unchanged<sup>92</sup>.



**Fig. 32** ONIOM (DFT-B3PW91/LanL2DZ/6-31G, PM6) optimized molecular simulation of a platinum atom bonding to the styrene ring of a SMA trimer.

### Scanning electron microscopy

A sample of the SMA-Pt solution was allowed to dry into a film for examination by SEM and EDAX. The polymer superstructure is not conductive in this state and so provided a poor surface for imaging by this method. In spite of this, EDAX data indicate that the visible platinum is likely in the form of unreacted platinum chloride, consistent with expectation that platinum reduction and nanocrystal synthesis occurs inside the polymer bilayer. Chlorine amounts determined by EDAX do not correlate to sodium and point sampling revealed no sodium chloride crystals. It is known from DFT simulation and Groves' experimental work that platinum, and not platinum chloride, crystals form in the SMA solution and so despite unfavourable energy of reaction, the absence of sodium chloride crystals indicates that the reduction reaction most likely produces chlorine gas directly:



in which case the minimum free energy of confinement is given by the energy of the reduction found above, 406 kJ·mol<sup>-1</sup>. This value is on the order of water O-H bond dissociation (459 kJ·mol<sup>-1</sup>) is not trivially overcome in homogeneously room temperature and pressure water.

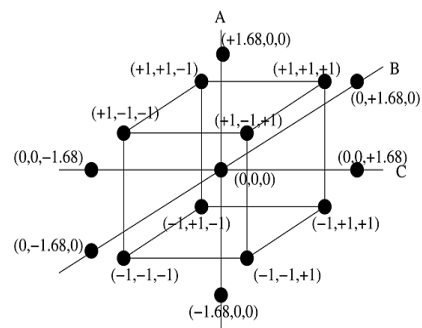
### Transmission electron microscopy

Samples of the SMA-Pt nanoreactor system were prepared at pH 3.6, 5, 7, and 9 and analyzed by HR-TEM. Concentration of PtCl<sub>2</sub> (0.016 – 0.185 M) and SMA (0.034 – 0.395 M) were also varied about a central condition to investigate dependencies. The 16 samples were prepared to fit the parameters of a response surface methodology central composite experimental design<sup>105</sup>. The values and schematic of the experimental design are shown in Table 3. Micrographs displayed the presence of monodisperse platinum nanoclusters in each sample, positively identified by the crystal *d*-spacing and consistency with the results reported at pH 7. Nanoparticle radius and diameter were determined from the area measured by circumscription within a circle using the ImageJ software package and analyzed with Microsoft Excel and the central composite design function within JMP statistical software.

Given the pH sensitivity of the supramolecular SMA template, it was expected that pH conditions would have the strongest effect on nanocluster growth within the template<sup>42,92</sup>. However, the TEM images shown in Figure 33 are typical of the images taken in that the SMA templated synthesis is not pH dependent.

**Table 3:** Experimental samples for central composite design.

Run	Coded values	pH	[PtCl <sub>2</sub> ] M	[SMA] M
1	(-1,-1,-1)	5	0.050	0.107
2	(1,-1,-1)	9	0.050	0.107
3	(-1,1,-1)	5	0.150	0.107
4	(1,1,-1)	9	0.150	0.107
5	(-1,-1,1)	5	0.050	0.322
6	(1,-1,1)	9	0.050	0.322
7	(-1,1,1)	5	0.150	0.322
8	(1,1,1)	9	0.150	0.322
9	(-1.682,0,0)	3.6	0.100	0.215
10	(1.682,0,0)	10.4	0.100	0.215
11	(0,-1.682,0)	7	0.016	0.215
12	(0,1.682,0)	7	0.185	0.215
13	(0,0,-1.682)	7	0.100	0.034
14	(0,0,1.682)	7	0.100	0.395
15	(0,0,0)	7	0.100	0.215
16	(0,0,0)	7	0.100	0.215

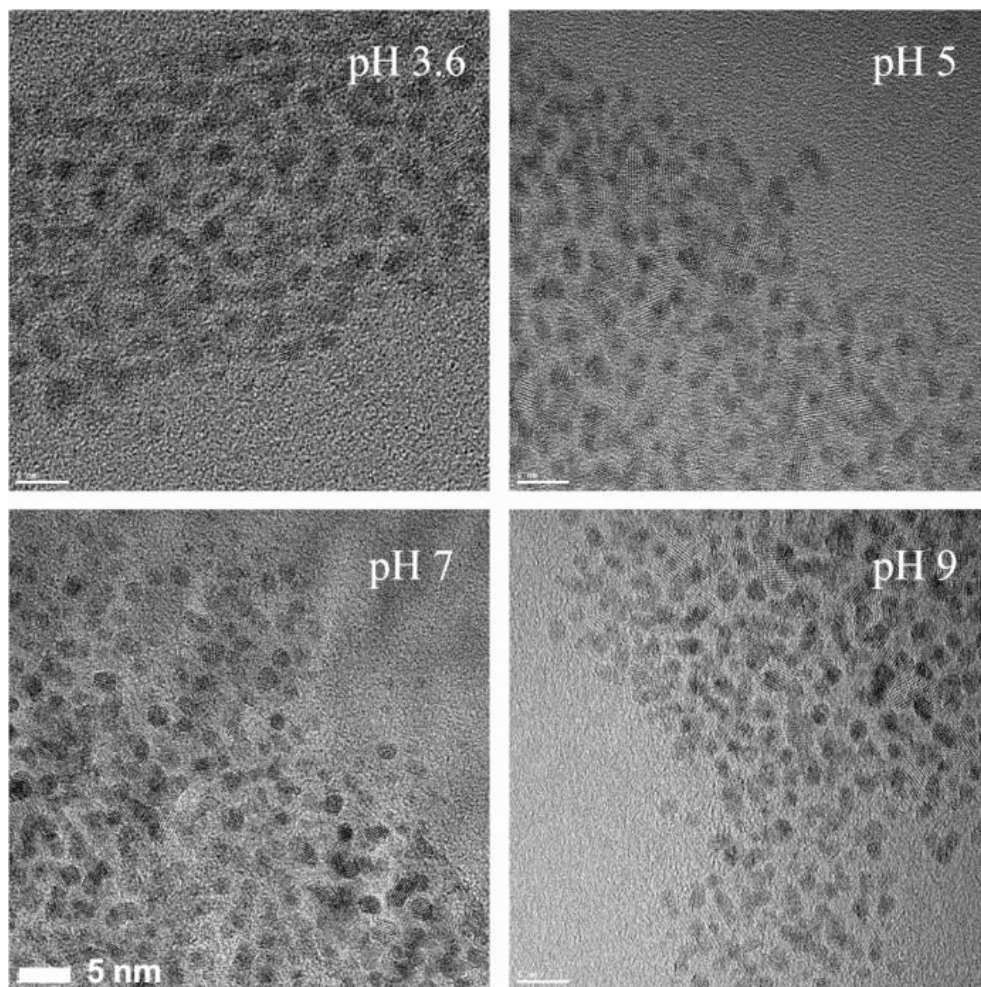


In fact, the only statistically significant dependence model that could be drawn from the bounds of the experimental set is:

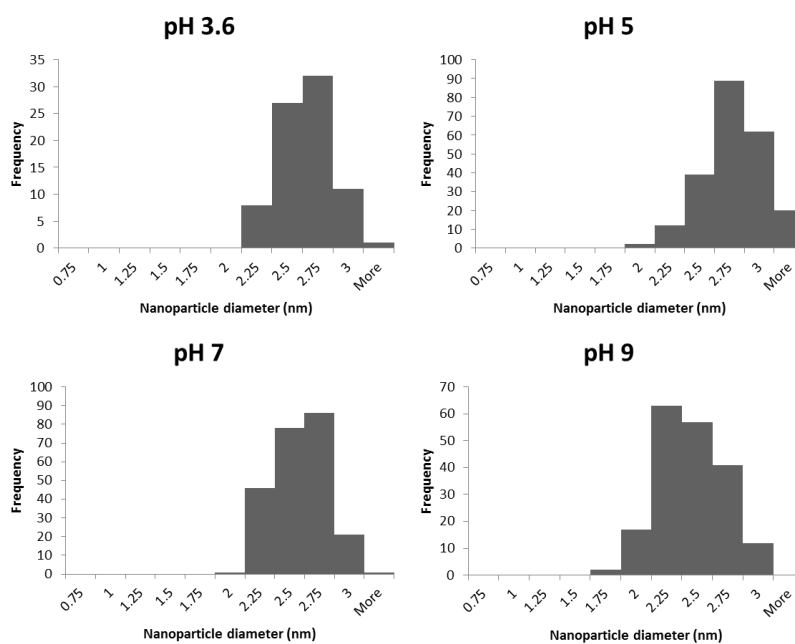
$$radius = 1.226 + [SMA](0.07[SMA] - 0.009[PtCl_2])nm \quad [4.3.3]$$

which only serves to demonstrate that the synthetic method is only very slightly sensitive to these reaction parameters generally, and pH independence in particular. Furthermore, the Platinum nanoclusters did not precipitate out of the SMA matrix in acidic conditions as would be expected for pH sensitive systems due to the separation of the self-assembled chains into individual chains at low or high pH, demonstrating increased stability of the nanoreactors over a broad pH range.

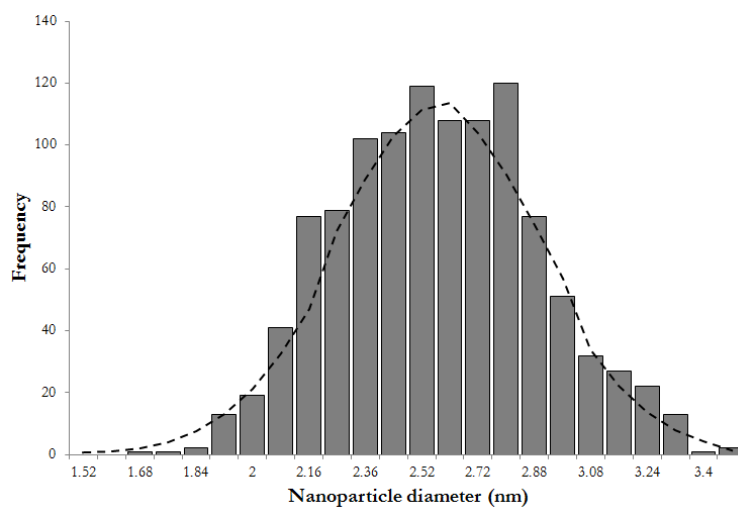
The size distributions shown in Figure 34 correspond to the images in Figure 33 and show no significant difference between the mean radius of samples prepared at pH 3.6 (1.26, s.d.= 0.10 nm; sample 9; n =79 ), pH 5 (1.25, s.d.= 0.12 nm; sample 1; n = 61), pH 7 (1.28, s.d.= 0.10 nm; sample 15; n = 140), or pH 9 (1.27, s.d.= 0.10 nm; sample 6; n = 83). The nanoparticles measured across all samples have a total mean diameter of 2.58, s.d = 0.32 nm; n = 1138 in an approximately normal distribution, shown in Figure 35.



**Fig. 33** HR-TEM images of SMA-Pt systems prepared at pH levels shown. Scale bar is 5 nm in all images.



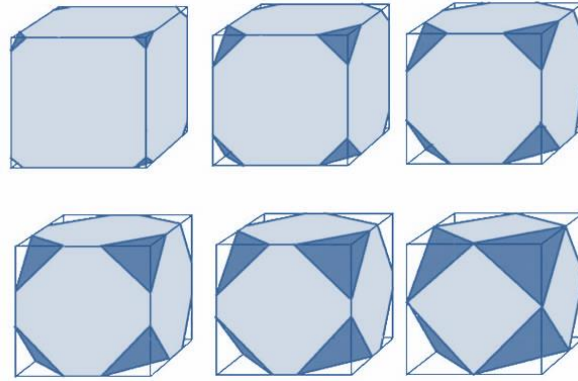
**Fig. 34** Diameter distribution of platinum nanoparticles prepared at pH values shown.



**Fig. 35** Diameter distribution of all platinum nanoparticles measured. Dashed line follows a normal distribution with mean and standard deviation equal to the sample set.



Fast fourier transform (FFT) analyses of the platinum crystal images form two rings at 0.19nm and 0.22nm. Using the literature value of platinum's lattice constant, 0.392nm, these spacing values correspond to the (200) and (111) crystal planes; these results agree with the x-ray diffraction spectrum reported by Groves *et al.* for the SMA-Pt system<sup>45</sup>. The dominance of these planes in conjunction with inspection of the crystal silhouettes seen on TEM indicate a truncated cubic or cuboctahedral crystal shape, illustrated in Figure 36.



**Fig. 36** Truncated cubic progressing to cuboctahedral solids top left to bottom right. Light blue represents the (200) and dark blue the (111) faces of the fcc platinum crystal. (Reproduced from <http://science.larouchepac.com>).

### Small-angle neutron scattering

To characterize the SMA nanoreactors with Pt active centres unsupported in aqueous solution, samples were analyzed by SANS. The lamellar model for the SMA structure<sup>2</sup> was combined with a triaxial ellipsoid form factor to model the metal nanocrystals as described in §2.2.4:

$$P(q) = \frac{scale}{V_{ell}} \int_0^1 \int_0^1 \phi^2 \left\{ q \left[ a^2 \cos^2 \left( \frac{\pi x}{2} \right) + b \sin^2 \left( \frac{\pi x}{2} \right) (1 - y^2) + c^2 y^2 \right] \right\} dx dy \quad [4.3.4]$$

where

$$\phi^2(x) = 9 \left( \frac{\sin x - x \cos x}{x^3} \right)^2 \quad [4.3.5]$$

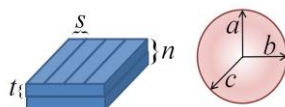
This model was applied to the SANS data for SMA-Pt systems at pH 5 and 7 with satisfactory results, as shown in Figure 37, demonstrating the pH stability of the polymer's nanosheet conformation. The triaxial ellipsoid model parameters obtained from the fit of the spectra of the SMA-Pt system at pH 7 and pH 5 give an average radius of 12.77 Å and 12.44 Å respectively, shown in Table 4, resulting in Pt nanocluster diameters of approximately 2.5 nm for both pH values. This value is in agreement with the nanocluster size observed by HR-TEM (Figures 34-35).

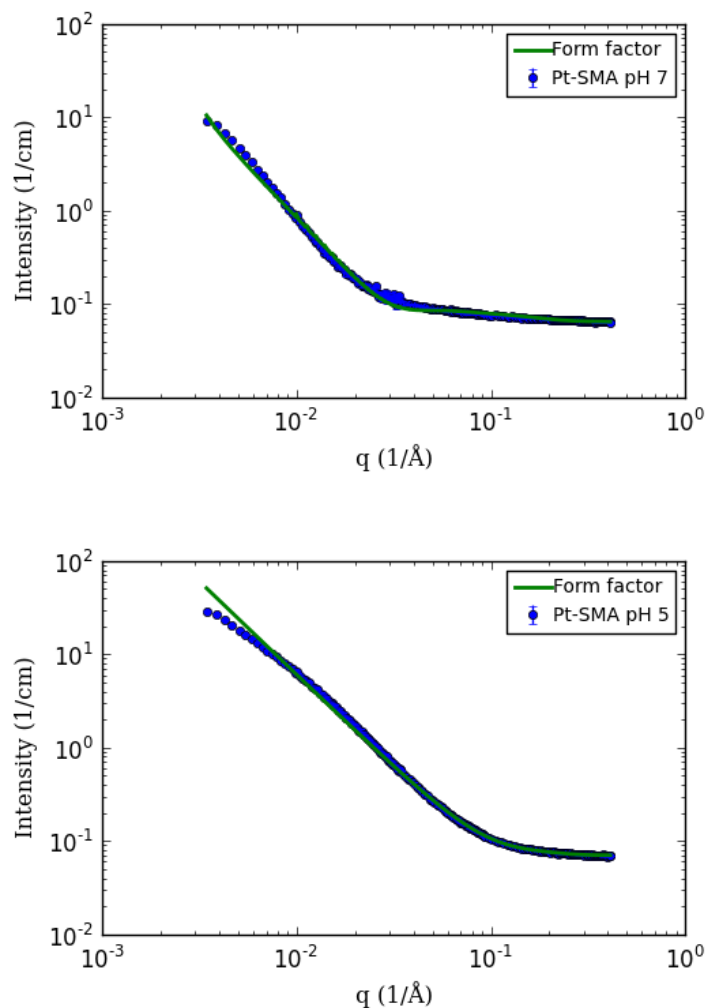
The quality of fit statistic ( $\chi^2/n$ ) quantifies how well the form factor describes the experimental data; a smaller value indicates a better fit. The quality of fit value could be made arbitrarily small by the inclusion of more parameters *ad infinitum*, however a physical model with lower fit quality is preferable to a non-physical, high fit quality model. The high value for SMA-Pt at pH 5 is due to the discrepancy between the data and fit in the very low Q range of the SMA-Pt systems, attributable to the lamina form factor's assumption of an infinite sheet where the SMA structures are finite within this range.

**Table 4.** SANS model fit parameters for the SMA, SMA-gold, and SMA-platinum at pH 7 and pH 5 systems in D<sub>2</sub>O.

	Parameter	SMA pH 7	SMA-Au pH7	SMA-Pt pH7	SMA-Pt pH5
Lamina	SLD <sub>solid</sub> (Å <sup>-2</sup> )	1.87e-06	1.87e-06	1.87e-06	1.87e-06
	SLD <sub>solv</sub> (Å <sup>-2</sup> )	6.38e-06	6.38e-06	6.38e-06	6.38e-06
	Spacing $s$ (Å)	6.99	8.04	6.66	6.30
	Thickness $t$ (Å)	12.34	95.64	14.59	12.61
	Layers $n$ (N)	1.00	7.23	1.01	5.38
Ellipsoid	SLD <sub>solid</sub> (Å <sup>-2</sup> )		4.66e-06	6.34e-06	6.34e-06
	SLD <sub>solv</sub> (Å <sup>-2</sup> )		6.38e-06	1.87e-06	1.87e-06
	Radius $a$ (Å)		2.68	16.76	7.97
	Radius $b$ (Å)		162.04	7.87	14.61
	Radius $c$ (Å)		266.78	13.69	14.74
Quality of fit ( $\chi^2/n$ )		37.1	3.7	18.5	85.8

Schematic representations of the form factors used in SANS fitting for lamina and tri-axial ellipsoid.





**Fig. 37** Lamella-ellipsoid fit (line) to SANS data of  $\text{PtCl}_2$  in 1:1 molar ratio with SMA monomers in 1% SMA solution at a) pH 7 and b) pH 5.

It is interesting to note that the scattering length density of platinum and  $\text{D}_2\text{O}$  are nearly identical, meaning that free platinum particles would have such low contrast to solution as to be invisible to SANS. In the fitted model, however, using SMA rather than  $\text{D}_2\text{O}$  as the solvent for the nanoclusters gives a better fit. This is in agreement with the quantum mechanical results showing platinum's preference for the hydrophobic region as well as the TEM series showing the nanoclusters embedded

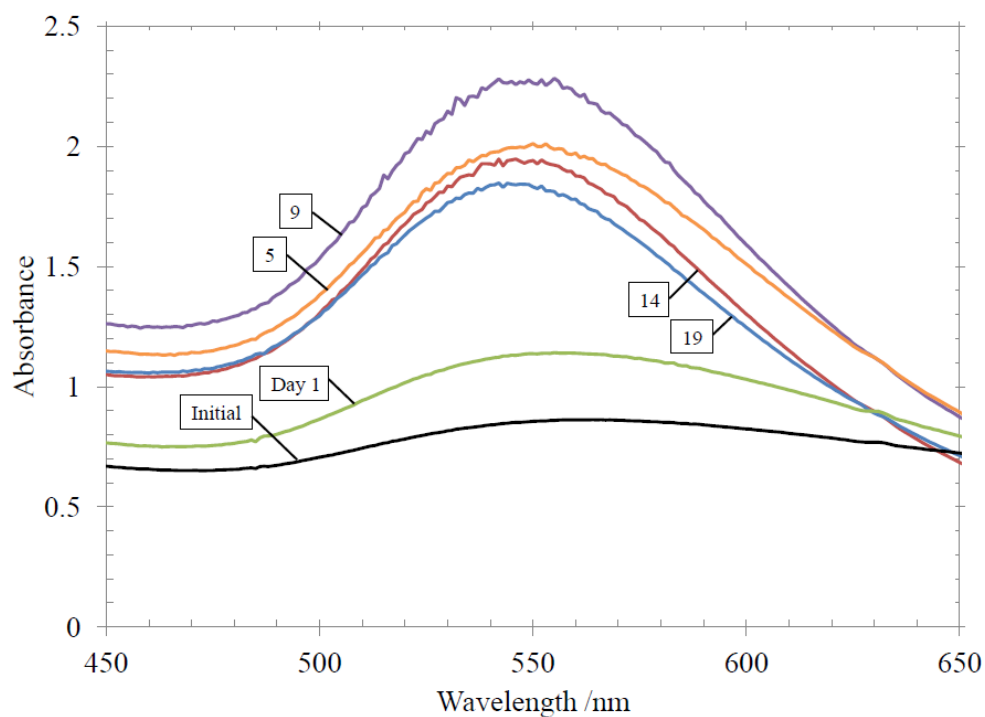
within the SMA structure, giving further evidence that platinum nanocluster synthesis occurs within the confined hydrophobic interior of the SMA structure.

#### 4.3.2 Gold

Gold is generally inert as a bulk material but nanocrystals under 5 nm have been found to demonstrate high catalytic activity<sup>106</sup>. The successful synthesis of platinum nanocrystals in this size domain encouraged expansion of the method to a hydrophobic gold salt.

##### UV/vis spectroscopy

Gold(I) chloride reduction and crystallization in the polymer template without reducing agents was monitored by UV/Vis, shown in Figure 38 by the growth of its characteristic peak at 547 nm. The peak is seen to increase for the first nine days and then settle slightly.

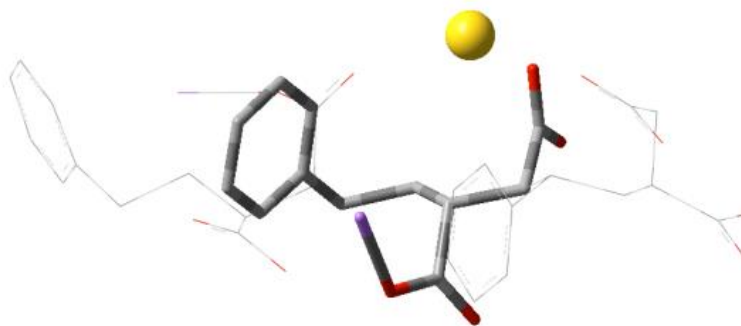


**Fig. 38** UV/vis spectra of AuCl added in 1:1 proportion to SMA monomers in 1% SMA solution. Peak centred at 547 nm increases for 9 days and becomes steady.

The diameter of spherical gold colloids in water can be closely estimated by the correlation of its radius to the wavelength of its plasmon band in accordance with Mie's theory<sup>72</sup>. Initial analysis by this method suggested a gold nanocrystal diameter of 77.7nm, far greater than SMA's 2.8 nm limiting inner cavity. This first suggested different reaction mechanisms and final structures for gold and platinum in SMA solution. The Mie-based radius calculation method assumes free spherical particles, conditions which we will find are not valid in this case.

### DFT modeling

Electronic structure calculations (DFT) were performed to predict the fine polymer-gold interactions. Beginning in identical position relative to the SMA polymer as the platinum atom, a free gold atom was found to preferentially associate with the polymer's oxygen-carrying functional groups. Energy minimization pulls gold away from the hydrophobic regions and toward the nearest oxygen for a binding energy of 0.21 eV (19.95 kJ mol<sup>-1</sup>), 1/10th the Pt-styrene association strength (Figure 39).



**Fig. 39** Optimized ONIOM model of a gold atom co-ordinated to the oxygen-rich maleic acid group of SMA. Simulation used DFT B3LYP/6-31G:LANL2DZ level of theory.

This indicates that gold nanocrystal formation should occur primarily on the hydrophilic surface of the polymer structure and gives further indication that platinum and gold salt reduction proceeds along different pathways. As with platinum, the gold atom does not disrupt the polymer chain's linear conformation and so should not affect SMA self-assembly.

### Scanning electron microscopy

The presence of gold crystals on the outer surface of the polymer bilayer made the SMA-Au system a more promising candidate for SEM and EDAX analysis than the SMA-Pt sample. Indeed gold was found in small quantities on the surface, as were

crystals of NaCl given the elemental ratios in Table 5. Since sodium acts as the counterion to the monoprotonated acid in solution, a higher concentration occurs on the hydrophilic outer surface. The presence of both gold metal and sodium chloride salt crystals provided evidence that the reduction of gold occurs on the exterior surface of the SMA bilayer structure.

Although the precise size and shape of the gold crystals could not be determined by this method, the findings obtained were consistent with the UV/vis spectroscopy data and quantum mechanical results indicating the formation of large crystals exterior to the SMA structure. Because the reaction does not take place within the confinement region, and because polymer solutions have previously been used to reduce and cap gold nanoclusters, it appeared possible that this reaction was independent of polymer nanostructure. Further analysis by transmission electron microscopy was necessary for complete characterization.

**Table 5.** EDAX elemental analysis of Gold-SMA thin film

Element	Wt %	At %
<b>C K</b>	11.64	28.80
<b>O K</b>	07.31	13.58
<b>NaK</b>	23.44	30.29
<b>ClK</b>	27.13	22.74
<b>AuL</b>	30.48	04.60

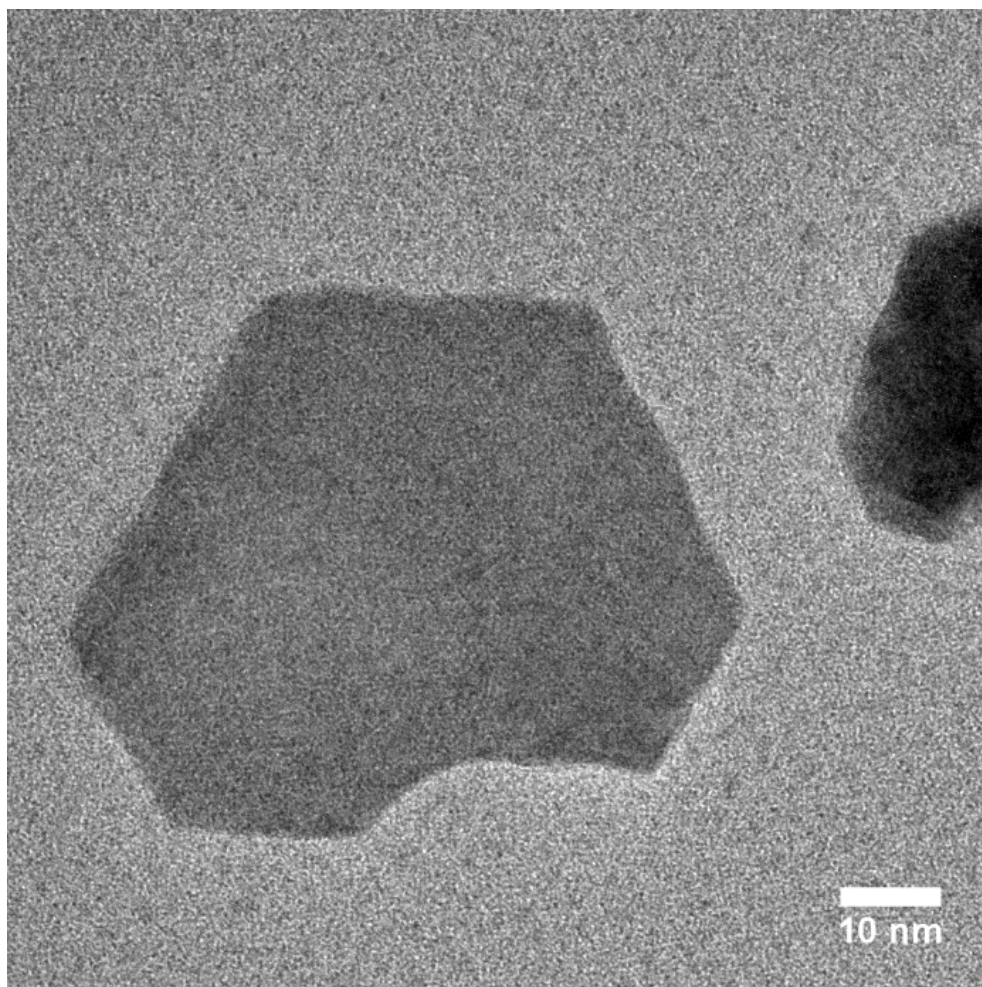
### Transmission electron microscopy

TEM images confirmed that gold chloride did reduce and form crystals in SMA solution and also revealed the size and crystal structure. Rather than the spherical, relatively uncoated colloids required by Mie's theory, the gold crystals discovered were ultrathin sheets that grew exclusively in contact with the surface of the SMA structure.

Gold nanosheets have been shown to form between layers of self-assembling surfactants<sup>107</sup>. Furthermore, gold with at least one dimension under 6 nm has a stable hexagonal close-packing (hcp) crystal structure that becomes dominant as that length decreases<sup>108</sup>. In this study, HR-TEM images of SMA-gold systems reveal that single crystal gold monolayers were produced, shown in Figure 40. A selected area electron diffraction (SAED) pattern taken from the crystal shown indexes to the (0001) hcp plane (Figure 41; compare Figure 24). Calculating the radial distance of the  $1\bar{2}10$  and  $1\bar{1}00$  points using the unit cell parameter  $a = 2.96\text{\AA}$ , in accordance with Huang<sup>108</sup>, places those points at  $7.94\text{ nm}^{-1}$  and  $4.20\text{ nm}^{-1}$  respectively – distances seen exactly on the SAED pattern. The  $d$ -spacing associated with these two points are  $0.14\text{nm}$  ( $1\bar{2}10$ ) and  $0.24\text{nm}$  ( $1\bar{1}00$ ), both of which are measurable in TEM images.

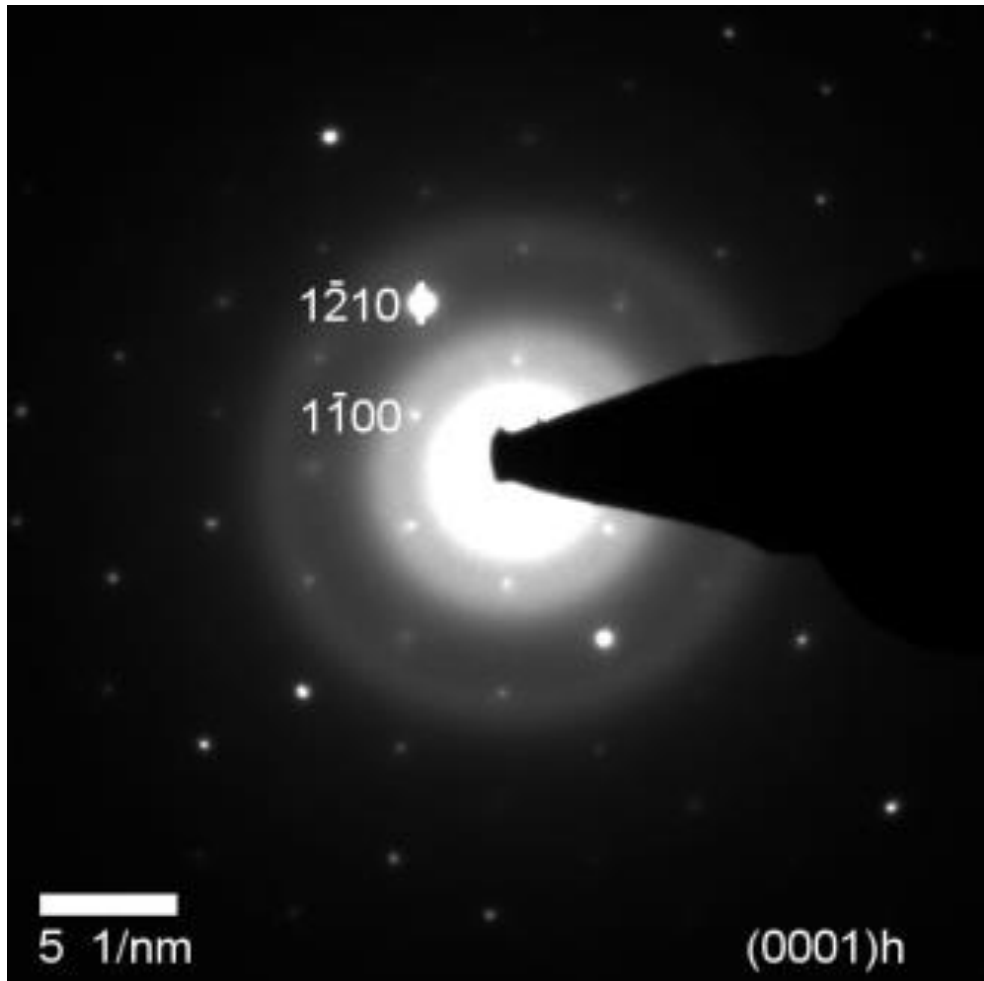
Unlike the previous study of hcp in gold nano-sheets<sup>109</sup>, our results do not show evidence of phase transition to face-centred cubic (fcc) under electron beam irradiation. Indeed, a nanosheet thickness on the order of single atomic layers explains their stability since (0001) hcp and the (111) fcc plane are identical at that scale. Their stability as independent monolayers is also evident by the appearance of Moiré fringe patterns where there is overlap of two monolayers, as shown in Figure 42. These interference patterns arise where one layer of parallel lines is visible through another. The distance  $d$  between peaks of Moiré fringes is  $d = s / \sin \alpha$  where  $s$  is the underlying line spacing and  $\alpha$  is the angle between them. In this case  $s = 0.24$  nm and  $\alpha = 14^\circ$ , making  $d = 1$  nm, equal to the band distance observed, giving strong evidence of the hexagonal crystal structure and therefore sheet thickness under three atomic layers.

There is a tendency, however, for the gold plates to cluster and aggregate, as seen in Figure 42. This could be an artefact of the drying process though it could also be evidence that SMA-Au association produces alternating layers of polymer and metal. This conformation would place islands of atomically thin and flat *hcp* gold within a hydrophilic confined space, an arrangement with exceptionally high potential for catalytic application.

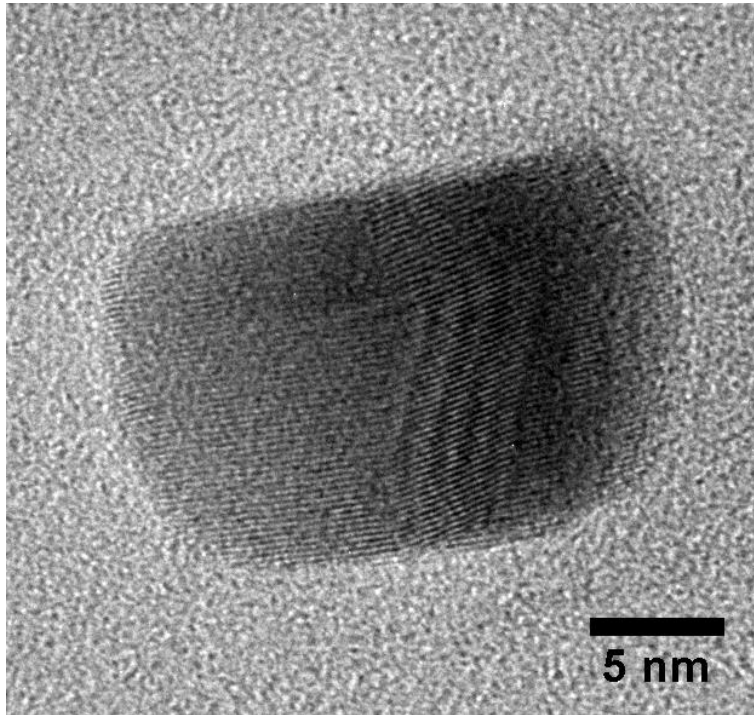


**Fig. 40** 2.6  $\mu\text{m}^2$  gold monolayer. Scale bar is 10 nm.



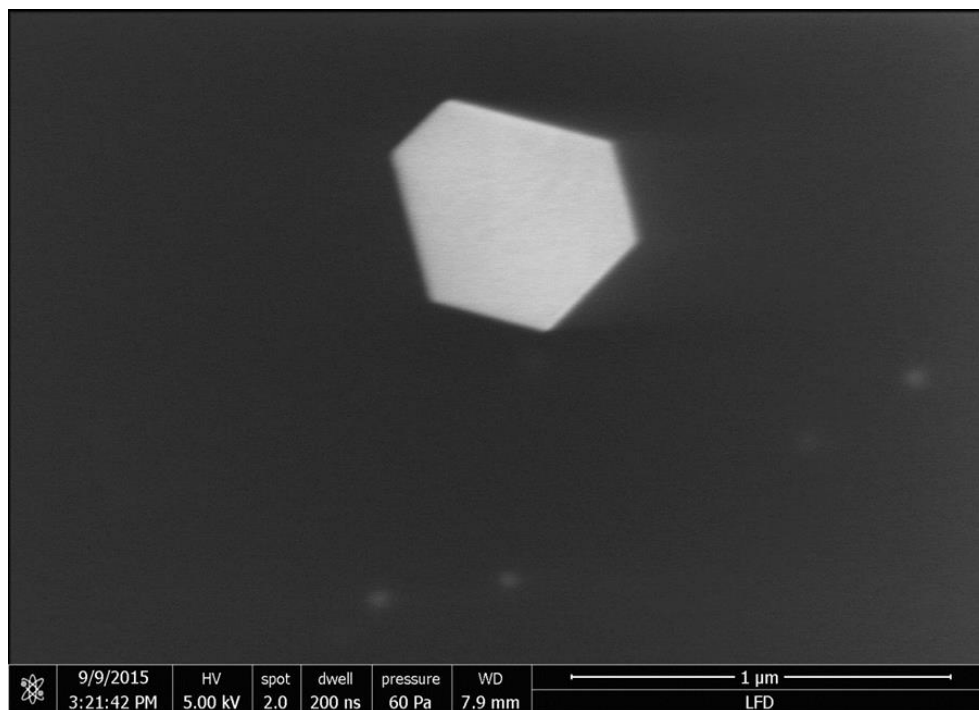


**Fig. 41** SAED of Fig. 40 consistent with hexagonal close-packing crystal structure.



**Fig. 42** Two discrete gold nanosheets producing a 1 nm Moiré fringe pattern by their overlap. Scale bar is 5 nm.

A further thin film sample was subjected to scanning electron microscopy on a higher resolution instrument. Gold nanosheets as large as 500nm were discovered on the polymer surface, an example of which is shown in Figure 43. These sheets displayed the hexagonal geometry seen under TEM, indicating that the *hcp* crystal structure and atomically thin dimension were retained. At this scale, top-down nanotechnology techniques such as etching may be applied to the gold crystal for advanced applications in electronics, plasmonics, and optics.



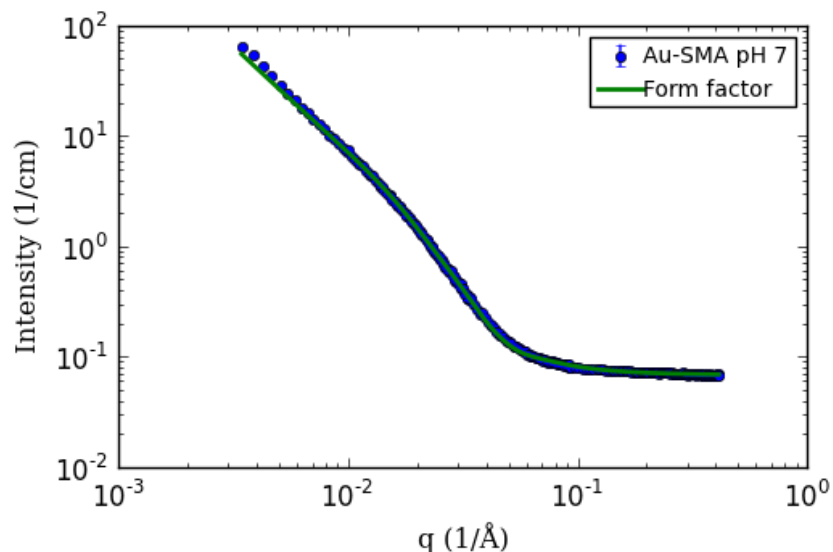
**Fig. 43** SEM image of gold crystal with chords >500nm.

### Small-angle neutron scattering

The SANS analysis performed provided further evidence of gold monolayer formation within the hydrophilic confinement space created by adjacent SMA bi-layers. The same lamella-ellipsoid model as was used for SMA-Pt was fitted to the SMA-Au system. The three radii parameterized by  $a$ ,  $b$ , and  $c$  fit well where  $a = 2.7 \text{ \AA}$ ,  $b = 16.2 \text{ nm}$  and  $c = 26.6 \text{ nm}$ , consistent with an atomically thin gold disk (Figure 44). These data confirm correspondence between the crystalline polymer sheets and gold monolayers seen under TEM with their existence in solution. The thickness parameter optimized to  $95.6 \text{ \AA}$  in 7 layers, supporting the hypothesis that the clustering of gold monolayers is due to SMA-Au layering in solution (§4.3.1, Table 4).

To the best of our knowledge, this is the first successful synthesis of stable, dispersible, atomically thin gold nanosheets in ambient conditions. Recently reported syntheses using  $\text{HAuCl}_4$  without additional reducing agent have produced gold nanosheets under  $10 \text{ nm}$  but none thinner than  $2.4 \text{ nm}$ <sup>107,108,110–112</sup>. The results presented here extend those findings to include a simple and environmentally-friendly synthesis of single atomic layer gold sheets by AuCl in SMA. This first successful

synthesis of pure atomically thin gold sheets holds great promise for advances in electronics, sensing, medicine and plasmonics<sup>113,114</sup>.



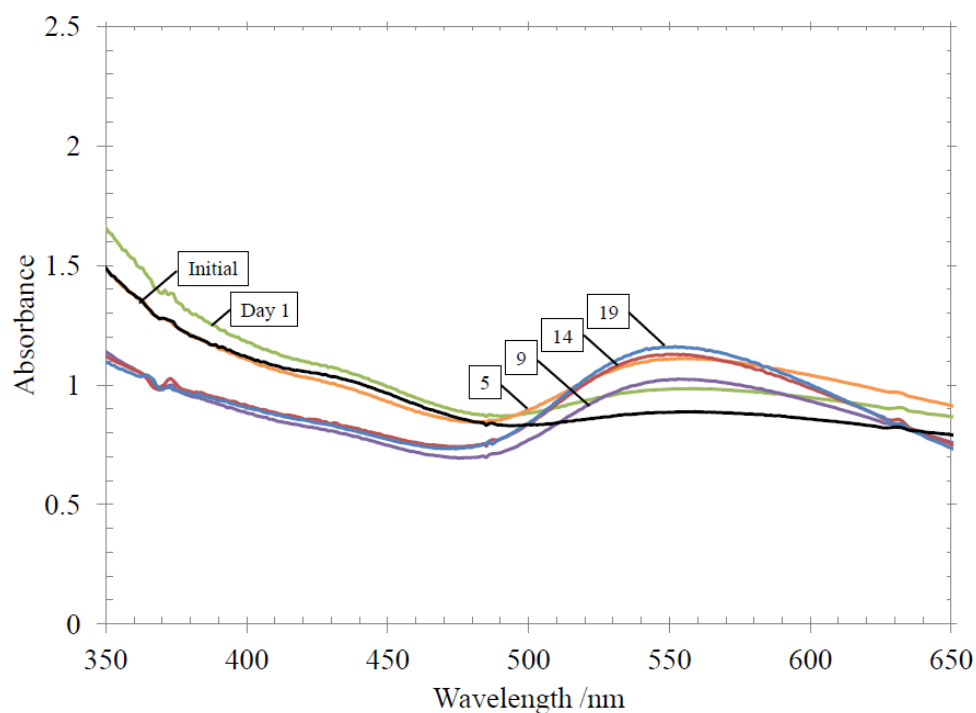
**Fig. 44** Lamella-ellipsoid model fitted to SANS data of AuCl in 1:1 molar ratio with SMA monomers in 1% SMA solution, pH 7.

#### 4.3.3 Platinum-gold combined system

To explore the interdependence of confinement domain and active centre metal, experimental sets were prepared to compare two methods of mixing gold and platinum salts together in SMA solution: one by mixing  $\text{PtCl}_2$  and AuCl together and adding the mixture to 3mL of SMA solution for a 1:1 molar ratio of metal atoms to SMA monomers (Method 1), the other by mixing  $\text{PtCl}_2$  in 1.5mL SMA solution and AuCl in 1.5mL solution and combining the two into a single container after sonication to again achieve a 1:1 ratio of total metal atoms to SMA monomers (Method 2).

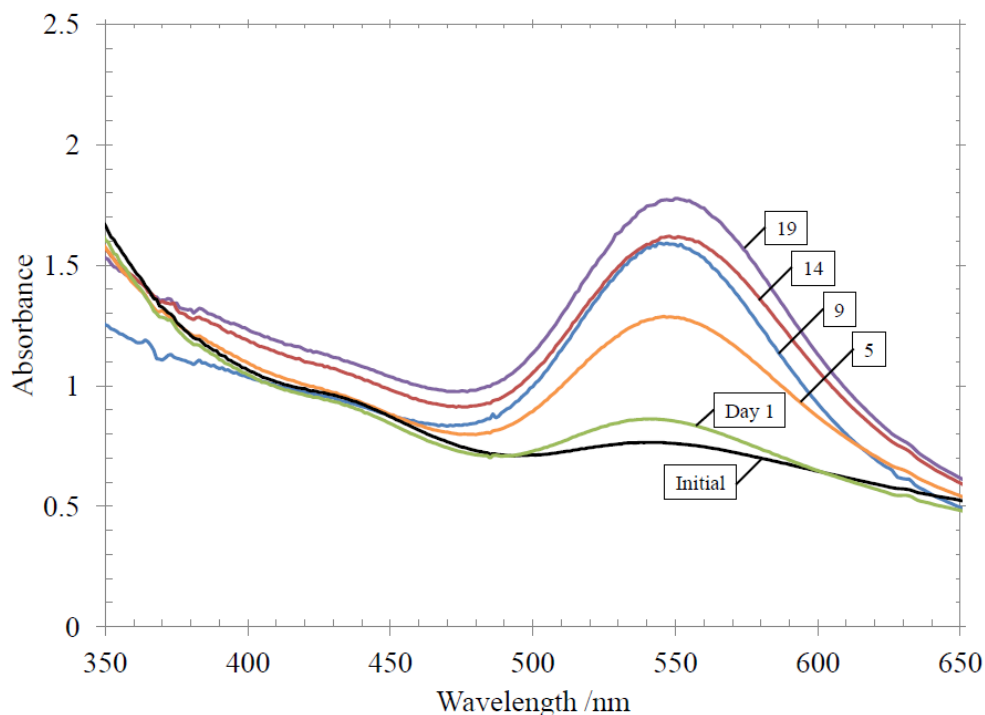
Following the evolution of synthesis of platinum and gold nanoparticles by UV/vis spectroscopy provided insight into mechanistic and structural differences specific to the metal salt species and mixing method. The UV/vis spectra obtained for Method 1, Figure 45, is not equivalent to a combination of those for platinum and gold shown in Figures 30 and 38 - instead it appears to produce some electronic interaction between the metal crystals. The decreased intensity of the gold peak and red-shift to 554 nm in Figure 45 is indicative of gold-platinum alloying or the formation of a gold-platinum

core shell structure<sup>115,116</sup>. A red shift greater than 20 nm combined with lower intensity has been reported for a 3:1 Au:Pt ratio<sup>115</sup>. The relative subtlety of the effect observed here means that there would be a very small amount of platinum in either arrangement. However, because the intensity of the gold peak is pulled downward by platinum reduction between day five and nine it is more likely that nanocrystal synthesis occurs independently for each metal and that they might interact indirectly through the polymer sheet.



**Fig. 45** UV/vis spectra of AuCl and PtCl<sub>2</sub> mixed in SMA by method 1. Shoulder at 430 nm diminishes and peak at 554 nm increases over time.

The last sample is a combination of separately prepared platinum and gold SMA systems mixed by Method 2. The spectrum in Figure 46 is a sum of the separate gold and platinum peaks (see Figures 30 and 38 for comparison) indicating independent crystal growth. It also suggests no exchange of metals between the SMA-Pt and SMA-Au systems will occur. This shows that SMA-metal association is rapid and that their bonds are highly stable once formed.



**Fig. 46** UV/vis spectra of AuCl and PtCl<sub>2</sub> mixed by method 2. Peak is centred at 547 nm and rises with time.

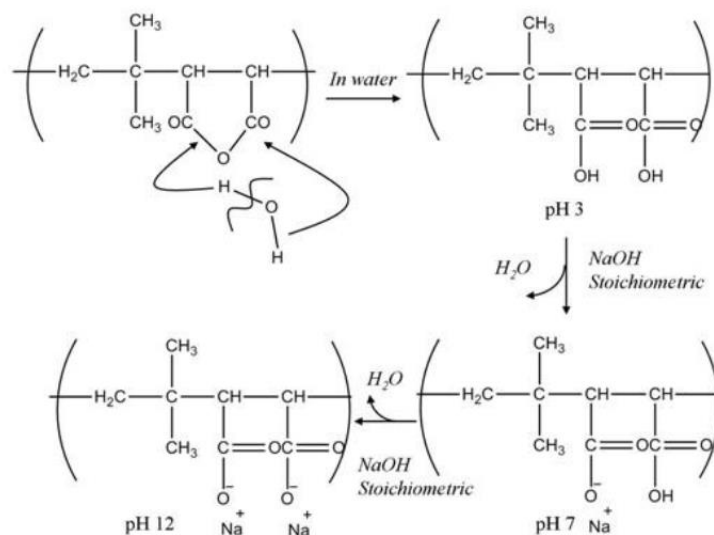
In the samples prepared with gold and platinum salts in solution, there was no evidence seen of alloy formation, although the possibility that some platinum atoms are included in the gold crystals cannot be ruled out. Since the size and shape of the platinum nanoclusters are unchanged, the two metals appear to crystallize independently of one another: platinum within and gold on the exterior surface of stacked SMA bi-layers.

This arrangement has a strong potential to produce a nanoreactor system capable of catalyzed and confinement-enhanced reactions of both polar and non-polar substrates. Controlling the hydrophobicity is a crucial parameter in optimizing a nanoreactor as it controls the physical properties of the solvent (diffusion, density, structure, transport properties)<sup>117</sup>. Therefore, being able to control reactions within confined cavities with different hydrophobicity and different active centers within a nanoreactor holds great promise for controlled reactions under environmentally friendly conditions. The affinity of gold toward the hydrophilic cavity and platinum to the hydrophobic cavity of SMA using hydrophobic precursors for the synthesis of the

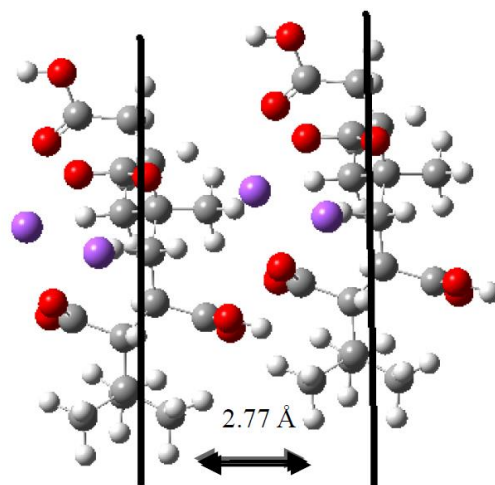
active centers (AuCl and PtCl<sub>2</sub> respectively) emphasizes the crucial role of the polymer-metal interaction for the optimization of the catalytic centre.

#### 4.3.4 IMA

Poly(isobutylene-*alt*-maleic anhydride), IMA, is a closely related molecule to SMA in primary and secondary structure, as shown in Figure 47. It too undergoes pH-dependent self-assembly in neutral aqueous solution into bilayer sheets containing a hydrophobic inner cavity<sup>43</sup>. Its self-assembly geometry was determined by modeling the electronic structure by quantum mechanical methods, shown in Figure 48. SANS characterization has shown its confinement space to be 2 nm, smaller on average than that of SMA. As described in §1.4.4, the spontaneous polymerization of pyrrole in IMA solution confirmed the polymer structure's ability to leverage the confinement effect to alter the dynamics of hosted reactions.



**Fig. 47** Schematic of IMA and its response to changes in solution pH (Reproduced from Ref. 43).

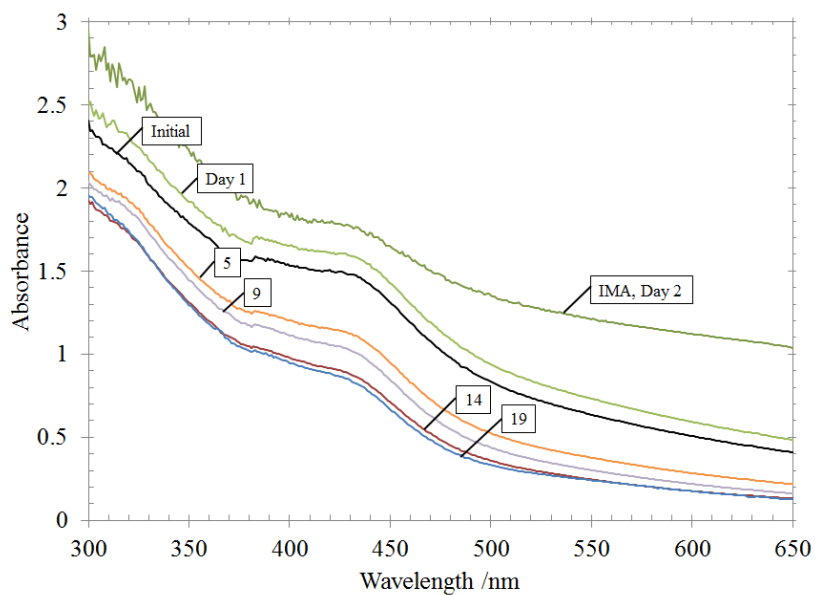


**Fig. 48** Simulation of the alignment of two IMA chains (Reproduced from Ref. 43).

A 1% wt/wt IMA solution was prepared by adding the polymer as received (Sigma-Aldrich, 6 kDa) to DI water. In accordance with Chan, sodium hydroxide was added to promote IMA solvation followed by hydrogen chloride to return to neutral pH<sup>43</sup>. As with the SMA samples, platinum(II) chloride was added at a 1:1 ratio with the IMA monomers.

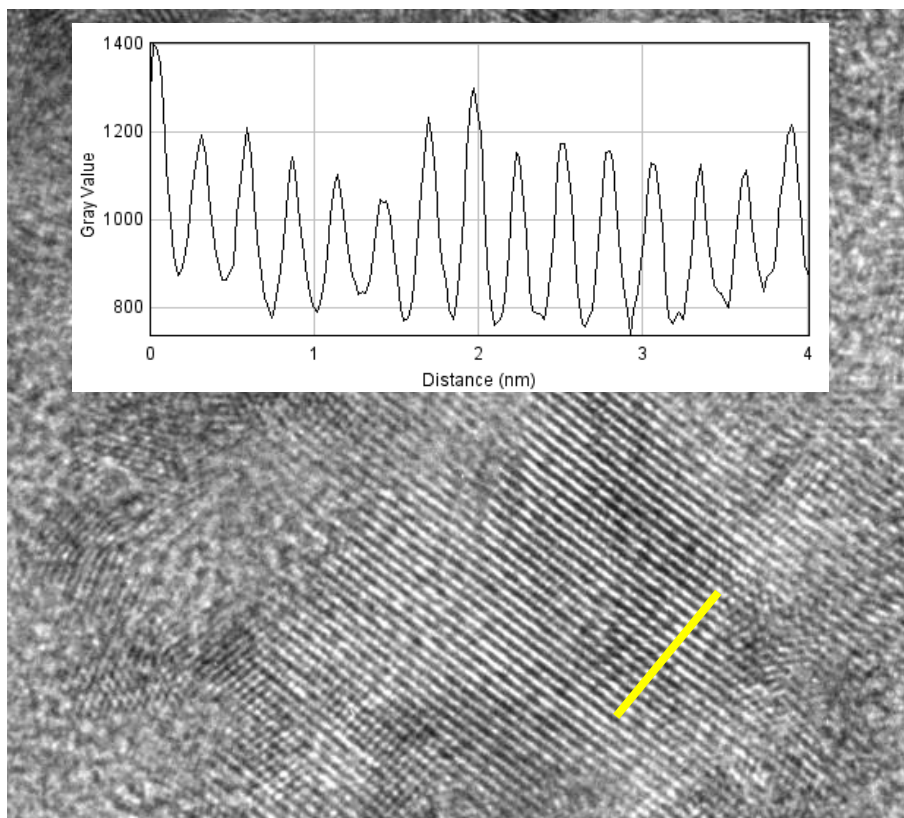
The reduction reaction was again followed by UV/vis spectroscopy. Rather than 14 days, however, the reduction reaction was complete after only two days, indicated by the change in solution colour from pale yellow to black. As with SMA, the rise of a platinum nanoparticle peak at 215 nm is obscured by broad absorbance by the polymer in the UV range, although the relative height above the baseline of the peak centred at 435 nm can be compared between the IMA-Pt spectrum and those of SMA-Pt in Figure 49.





**Fig. 49** UV/vis spectra of platinum reduction after two days in IMA (top line) and in SMA (days as marked).

High resolution transmission electron microscopy confirms the self-assembly of IMA into a bilayer sheet. In Figure 50, a profile plot was used to identify a crystalline region as the polymeric supramolecular structure. The average peak-to-peak difference was found to be 2.77 Å, exactly matching the predicted value (Figure 48) and previously reported TEM results. The line of points between the chain lines observed in the SMA image (Figure 26) are not seen in the IMA structure, again in concordance with the theoretically predicted structure. The images also confirm the presence of platinum crystals.

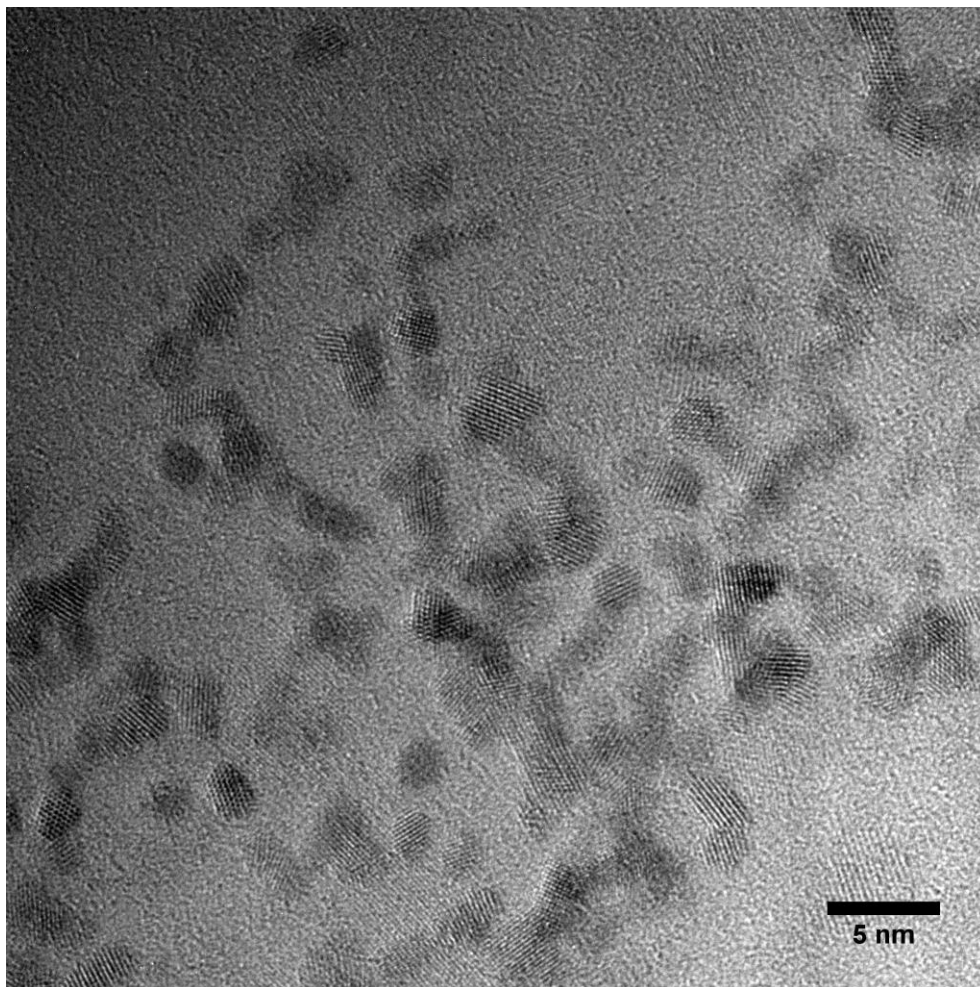


**Fig. 50** HR-TEM image of platinum nanocrystals in poly(isobutylene-alt-maleic acid) superstructure. Location of plot profile marked in yellow.

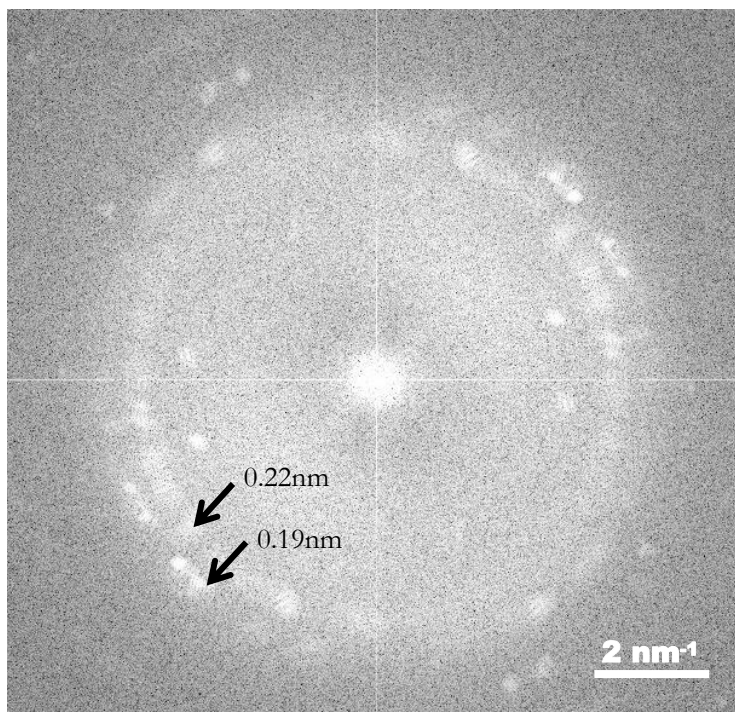
TEM images, and example of which is presented in Figure 51, show that the platinum nanocrystals form in IMA as in SMA. However, the average radius of the nanocrystals in IMA was found to be  $1.18 \text{ s.d.} = 0.13 \text{ nm}$ , approximately  $0.1 \text{ nm}$  smaller than the mean radius of nanocrystals formed in SMA.

Fourier transforms of the TEM images reveal interplanar spacings of the platinum crystals at  $0.19$  and  $0.22 \text{ nm}$  indicating the (200) and (111) planes according to Equation 2.4.1 (§2.4.2), shown in Figure 52. The presence of these planes may be confirmed by direct measurement on HR-TEM images such as Figure 51. This is consistent with the x-ray diffraction and FFT results obtained for the nominally cuboctahedral samples prepared in SMA.

The existing data is insufficient to describe the relationship, if any, that lies between the size of the confinement space, the size and shape of crystal that forms within, and the kinetics of crystal formation, but the correlations hinted at by this experiment justify further investigation.



**Fig. 51** HR-TEM image of platinum nanocrystals synthesized from  $\text{PtCl}_2$  added at 1:1 molar ratio with IMA monomers in 1% IMA solution.



**Fig. 52** Fast Fourier transform of Figure 52. High intensity rings at 0.19 and 0.22nm appear due to random orientation of (111) and (200) crystal planes, respectively. Scale bar is 2 nm<sup>-1</sup>.

#### 4.4 Conclusion

Platinum(II) chloride will preferentially concentrate within hydrophobic nanodomains of the SMA architecture to produce nanoclusters with a diameter <3nm. This reaction occurs over a very broad pH range through a simple, reliable, and environmentally-friendly synthetic method. When the same method is applied to gold(I) chloride, however, it generates pure, stable *hcp* monolayers through the preferential interaction of gold with the hydrophilic surfaces of the SMA nanostructure. This first successful synthesis of pure atomically thin gold sheets holds great promise for advances in electronics, sensing, medicine and plasmonics.

The self-assembled nanostructure of the template with alternating hydrophilic and hydrophobic nanodomains allows the development of a complex nanoreactor with Pt nanoclusters and Au nanosheets as active centres. The characterization of the properties and catalytic efficiency of the nanoreactors remains an active area of investigation.

The fact that the laminar SMA-metal nanoreactor remains stable in low pH conditions opens the possibility of tuning the polymer's conformation and pH sensitivity according to the application. The systems presented here offer efficient biomimetic nanoreactors for application in a range of environmental conditions, such as the acidic electrolyte of proton exchange membrane fuel cells or in the variable pH and ion strength of water detoxification.

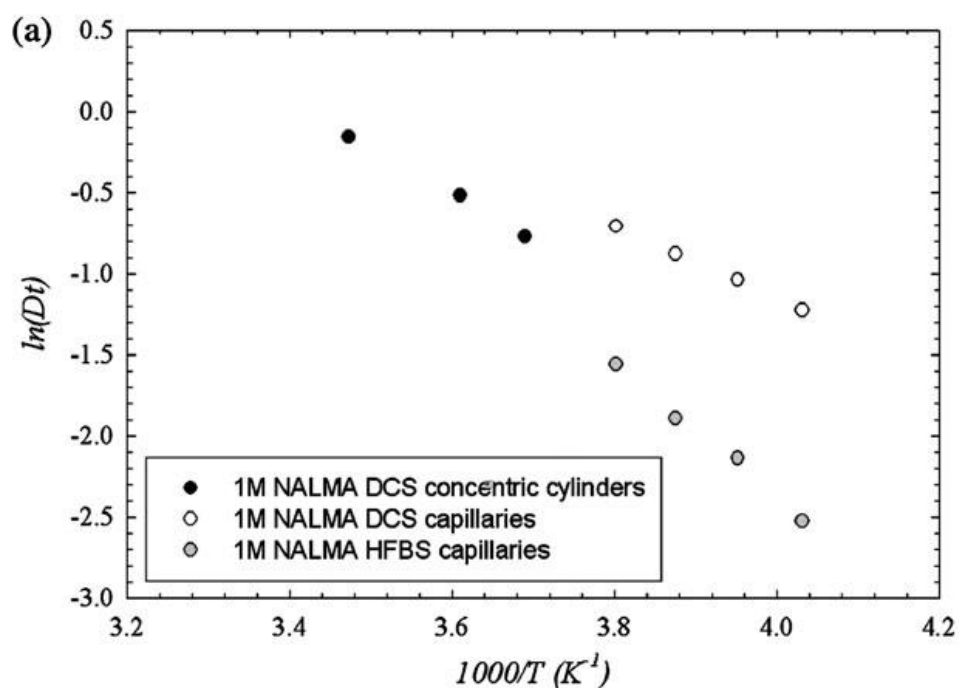
## 5 Implications for Theory

Progress towards the development of artificial nanoreactors capable of producing reaction rates comparable to their biological counterparts demands a general theory of the mechanism behind the confinement effect that can explain existing experimental observations as well as produce testable predictions. First, the effects of confinement on water will be offered in order to complement the experimental data for non-polar molecules and hydrophobic metal salts presented in previous chapters. Second, a proposed mechanism for the effects will be introduced. Third, a method for expanding classical thermodynamic theory to account for the confinement effect will be discussed. Lastly, an example of how existing experimental results may be explained by the present theory will be provided.

### 5.1 Confined water dynamics

Millennia of evolution have optimized the macromolecular structures of protein enzymes to maximize confinement effects for the promotion and control of reactions, so it is important to study the surface side group distribution and their solvation properties. Proteins *in vivo* exhibit nearly equal surface coverage of hydrophilic and hydrophobic amino-acid side chains<sup>118</sup>. Enzymes act exclusively in aqueous media and so the reason why these natural nanoreactors should include such a high proportion of low solubility groups has been the subject of extensive research.

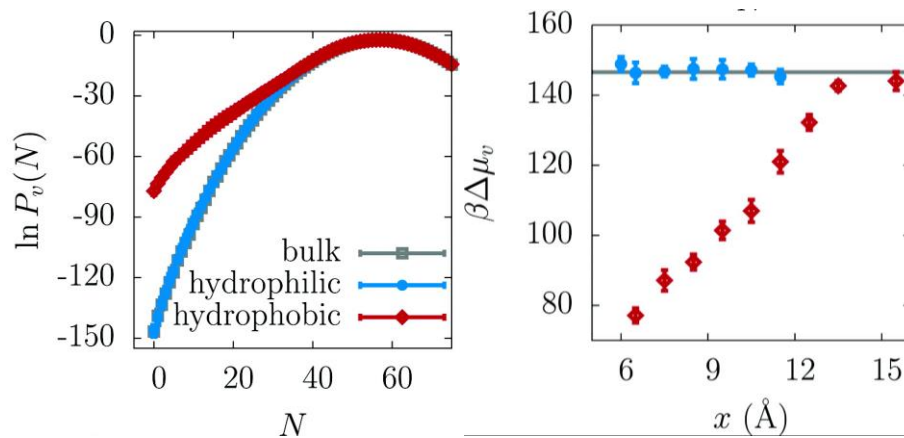
Beyond water's uses as a transport medium, thermoregulator, and reaction solvent, hydration is required for the structure and physiological function of almost all biological macromolecules<sup>119</sup>. Water translational dynamics are significantly altered under confinement near amphiphilic peptide surfaces as compared to purely hydrophilic peptides or bulk water<sup>120</sup>. Figure 53 shows splitting of temperature dependent water velocity in a sample confined with the amphiphilic peptide *n*-acetyl-leucine-methylamide (NALMA). The slower component is consistent with dynamics of supercooled bulk water. In comparison, a purely hydrophilic peptide, *n*-acetyl-glycine-methylamide (NAGMA) showed no anomalous temperature dependent dynamics. Molecular dynamics simulations were able to connect specific surface hydrophilities to their effects on water dynamics: water in contact with the hydrophilic areas were significantly slower than the more fluid molecules in contact with the hydrophobic side chain of the leucine<sup>121</sup>.



**Fig. 53** Water translational dynamics shown to split into fast (white circles) and slow (grey circles) under confinement in solution with an amphilic peptide (Reproduced from Ref. 119).

More recent molecular dynamics simulations complement these experimental and theoretical findings on the velocity of water molecules<sup>122</sup>. The probability of finding a number of oxygen atoms (as a proxy for water molecules) in a given sample volume was measured adjacent to hydrophobic and hydrophilic surfaces as well as in the bulk. Results in Figure 54 show a sharply reduced likelihood of finding water adjacent to a hydrophobic surface as compared to a hydrophilic surface or bulk water. The difference decreases linearly with distance from the hydrophobic surface until it is equivalent to the bulk at 15 Å.

The above studies indicate that the velocity and density of water molecules are significantly affected by their proximity to hydrophobic regions, and that the effect is strongest when heterogenous surfaces are in close relation. At minimum, a potential synthetic analogue to the protein macromolecule would need to be water soluble while providing a hydrophobic cavity for the attraction of non-polar substrate molecules. An amphiphilic structure would meet both of these requirements while possibly also harnessing the ability to direct water dynamics through surface effects described here.



**Fig. 54** The probability  $\ln P_v(N)$  of finding  $N$  water molecules at the hydrophobic surface is much lower than at a hydrophilic surface or in the bulk (coinciding in the left-hand graph). The difference diminishes linearly as  $x$  approaches  $15 \text{ \AA}$  (right hand graph). Water density is subsequently lower in hydrophobic-adjacent regions. (Reproduced from Ref. 120).

## 5.2 The mechanism of confinement

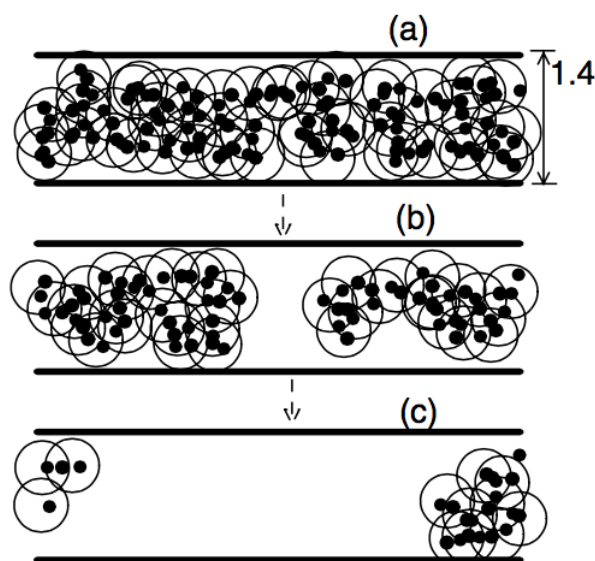
What remains to be shown is how the SMA nanostructure might be responsible for producing a net potential energy within its hydrophobic interior and how that would be expressed by the molecules within. Favourable interfacial energy could explain separation of pyrrole into the hydrophobic SMA interior, but does not explain why it would compress to a higher density than bulk pyrrole. Recall that separation but not compression was observed in the  $50 \text{ nm}$  micelles, in pure water, nor (by definition) in bulk pyrrole<sup>44</sup>. Also, if the attraction to the hydrophobic nanodomain is strong enough to pressurize the space, why should it compress the pyrrole and not expand the bi-layer into a thicker envelope instead? There is no indication in the quantum mechanical model of its electronic structure presented in §3.3 that the  $\pi$ - $\pi$  interactions responsible for self-assembly could withstand the classically equivalent pressure<sup>123</sup>.

Hydrophobic solutes present no hydrogen bonding sites and so disrupt the tetrahedral network of bulk neat water<sup>124,125</sup>. Small non-polar molecules (under  $1 \text{ nm}$ ) permit a restructuring of the hydrogen bonding network around it and so solubility is entropically determined<sup>126</sup>. Large molecules, alternately, offer a non-polar surface that denies neighbouring water molecules the possibility of a complete complement of hydrogen bonds and solubility is therefore enthalpy driven<sup>126–129</sup>. Subsequently,



solubility of small molecules scales with volume and large molecules with surface area<sup>128</sup>.

Water in contact with highly hydrophobic surfaces forms a 1-2 molecular layer thin vapour phase, as shown in Figure 55<sup>130</sup>. When two of these surfaces are in parallel proximity their combined effect can cause spontaneous drying of the confined interior region<sup>127,131</sup>. The pressure of the vapour phase being lower than that of the liquid, the two surfaces are pushed together – this is credited as the source of hydrophobic attractive force<sup>128,132</sup>.



**Fig. 55** Schematic representation of **a)** water molecules in a confined hydrophobic space **b)** formation of the vapour tube joining the surfaces and nucleating **c)** complete drying (Reproduced from Ref. 132).

Thermodynamically, this is possible at separations up to 100 nm but is kinetically limited to a critical distance around 2 nm<sup>133,134</sup>. The size and frequency of cavities in water (i.e. regions containing no water molecules) determines properties such as solvation free energies, compressibility, and permittivity<sup>131,132,135,136</sup>. The disruption of the water network in the confined region produced large density fluctuations that shift the cavity distribution to a larger mean<sup>124,125,135</sup>. The spontaneous drying event is nucleated by the formation of large cavities, wedges, and finally a vapour tube connecting one surface to the other<sup>132,134,137</sup>. The greater the surface hydrophobicity (or surface contact angle, equivalently) and smaller the separation distance, the more probable it becomes that the vapour tube will form.

Surfaces slightly less hydrophobic or further apart can suppress tube formation and therefore sustain a metastable liquid phase between them<sup>134,138</sup>. The larger mean cavity distribution in the confined phase means that it dissolves nonpolar molecules more readily, is less dense, has higher compressibility, and a lower dielectric constant than bulk water<sup>124,125,135</sup>. In other words, the confined phase has the properties of supercritical water. At a given separation, two relevant surface features can affect hydrophobicity and therefore surface wetting and confined phase stability: electrostatic polarity and surface roughness. A weak polarization of the surface can maintain wetting and suppress turnover into the vapour phase even at very short distances<sup>137,139</sup>. On the other hand, surface roughness increases hydrophobicity and promotes the phase change<sup>130</sup>.

### 5.2.1 Non-polar small molecules

SANS analysis indicates that the inner surfaces of the bilayer are not collapsed, suggesting the presence of metastable liquid water<sup>92,140</sup>. The ready dissolution of small hydrophobic molecules in this region supports this possibility<sup>44,45,140</sup>. The nanoreactors are soluble in water due to the external oxygen atoms: electrostatic sources potentially close enough to the confinement area to polarize its surfaces<sup>139</sup>. The change in cavity size distribution in the confined phase as a function of separation distance and polarity could be estimated through simulation. This distribution would provide a measure of solvation free energy, compressibility, and dielectric constant in the confinement region<sup>131</sup>.

The trajectory of dissolved non-polar solutes could be simulated in the confined space while monitoring density fluctuations and cavity formation. For a pyrrole-like model, if it is found that they tend to displace water against the hydrophobic surface, their concentration would act to increase surface roughness and distance from the electrostatic source. This would in turn increase hydrophobicity<sup>130</sup>, network disruption<sup>124</sup>, nonpolar molecule solubility<sup>135</sup> – a positive feedback loop that would ultimately enable vapour tube nucleation and drying of the confinement space<sup>137</sup>. Since the density of bulk pyrrole is lower than that of water, the compressive force that would arise may suffice to explain the decreased dynamics and increased polymerization reaction rate observed experimentally.

### 5.2.2 Metal salts

The internal pressure of a spherical bubble is inversely proportional to radius as given by the Young-Laplace equation:

$$\Delta P = \frac{2\gamma}{r} \quad [5.2.1]$$

where  $\gamma$  is the surface tension at the interface. For water at 293 K,  $\gamma \cong 0.073 \text{ Nm}^{-1}$ ; therefore a bubble formed inside the 3 nm SMA confinement space would carry an internal pressure of approximately 97 MPa or 2.74 N force per  $\text{nm}^{-2}$  surface area<sup>141</sup>. The energy associated with the formation and collapse of this bubble would be  $2.4 \text{ MJmol}^{-1}$  and amply able to provide the  $400\text{-}500 \text{ kJmol}^{-1}$  of energy required for the dissociation of metal chlorides or water<sup>140</sup>. If this is indeed the case it would explain the auto-reduction of metal salts in the confined water phase.

There is a growing body of literature describing the formation of very small, monodisperse metal and metal oxide crystals in supercritical water<sup>142</sup>. As a hydrophobic salt,  $\text{PtCl}_2$  would be highly soluble in the confined supercritical phase but would be less so as a free metal atom in solution<sup>142</sup>. When a nucleation site does form, as density functional theory simulations show can occur on the styrene ring of SMA, low solubility would drive metal ions to rapidly bind to that site rather than form another. This would produce a ‘catchment area’ that would define the ultimate size of the nanocrystal and, under one or two dimensional confinement, create regular spacing between crystals. All of these are in accordance with the monodisperse and evenly distributed platinum nanocrystals synthesized within SMA and IMA as viewed by TEM<sup>45,140</sup>. If the regular spacing between crystals is a factor in the growth patterns of polypyrrole, this would produce a preferred polymer length and, since length is correlated to absorbance maximum, explain why the UV/vis peak is sharper under platinum catalysis<sup>45</sup>. The chlorine gas that would also result from the reaction is only slightly soluble in water at room temperature but, like other gases, is miscible in supercritical or confined water<sup>143</sup>. The solubility difference would prevent re-oxidation of the metal.

Gold nanoplate formation does not proceed in the confinement space and so rapid metal phase separation in supercritical water cannot be responsible for the synthesis. It is clear that the metal species’ interactions with the polymer cannot be neglected while predicting potential outcomes. Gold association with the SMA exterior could be energetically favoured if its interaction with the oxygen groups is found to lower the potential energy of the confined water phase. Such anisotropic favourability would help explain the single-layer crystal morphology.

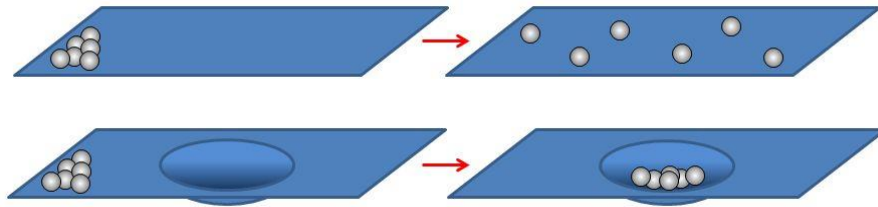
### 5.3 Confinement thermodynamics

The molecular dynamics studies cited in the preceding section note that discrete simulation is necessary because classical continuum theories fail. Simulation, on the other hand, is sensitive to the assumptions and empirical data that were used to construct the force-fields applied and may lead to incorrect results when the simulated system lies far from the optimized parameters. Assuming the model forces are correct,

each system must still be independently modeled and subjected to a series of simulation runs to amass the statistical data from which physical properties are determined. It can therefore require extensive effort and computational time to build a library of all the scenarios of interest. And so a continuum theory that is capable of correctly predicting thermodynamic behaviours under confinement would be valuable as the field continues to progress.

### 5.3.1 Potential energy

That random motion in a potential energy field can produce effects equivalent to externally applied pressure is a small but important observation. As an analogy, imagine a set of particles moving on a flat 2D plane in 3D space subject to a potential energy field applying downward acceleration (gravity). An illustration is shown in Figure 56. Over time, one would expect the particles to become and remain uniformly distributed across the plane: diffusion in accordance with equilibrium thermodynamics. However, if there was a depression in the plane whose depth was such that the velocity of random motion would be insufficient to overcome the downward acceleration, one would expect the particles to accumulate within the well and indeed to pack closer there than they would after diffusion on the flat surface.



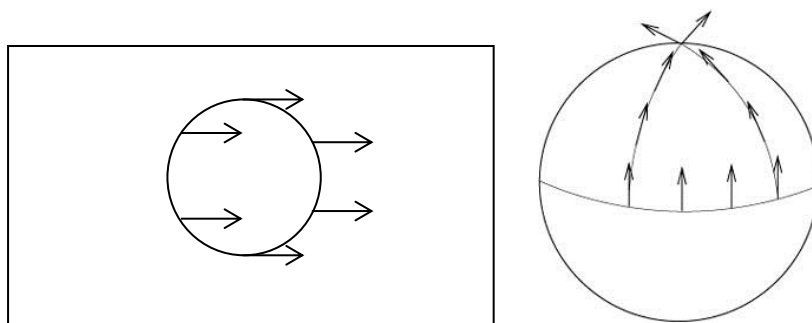
**Fig. 56** Diffusion on a flat surface (top) vs. diffusion on a curved surface (bottom).

By allowing a net potential to affect a curvature in the configuration space, random Brownian motion is able to reproduce the decreased intermolecular distance, increased compression, and decreased entropy and kinetics observed experimentally. In fact a curved space also meets the stronger requirements of energy and momentum conservation<sup>144</sup>. A geodesic line is the generalization to curved space of the straight line in flat space, *i.e.* the minimum distance between two points, and is defined as a curve  $x^\mu(t)$  in  $\mathbb{R}^n$  such that:

$$\frac{d^2 x^\mu}{dt^2} + \sum_{\sigma, \nu} \Gamma_{\sigma \nu}^\mu \frac{dx^\sigma}{dt} \frac{dx^\nu}{dt} = 0 \quad [5.3.3]$$

where  $\mu = \{1,2,3 \dots n\}$  and  $\Gamma_{\sigma\nu}^{\mu}$  is the Christoffel symbol describing the effects of parallel transport on the curved surface. In Euclidean (flat) space, the Christoffel symbols equal zero, and so the condition for the line simplifies to  $d^2x^{\mu}/dt^2 = 0$  which, given an initial position  $x^{\mu}$  and first derivative  $dx^{\mu}/dt$  gives a unique solution. In this notation it is easy to see the connection to Newtonian mechanics: a geodesic is the path of an object that experiences no acceleration.

Take for example two particles moving in parallel with no outside force acting on them so that they will undergo no change in energy or momentum. On a flat plane, these particles will never approach one another or, in the terms considered earlier, the intermolecular radius will never decrease. If, however, two particles begin moving in parallel on a sphere, their paths will approach one another without the action of an outside force, illustrated in Figure 57.



**Fig. 57** Initially parallel paths remain parallel on a flat surface (left image) but converge on a curved surface (right image). Also, the arrow remains parallel to itself as it is transported about a circle on the flat surface; the same is not true for curved surfaces, a difference accounted for by Christoffel symbols (Reproduced from Ref. 142).

We can therefore describe motion of pyrrole in bulk and confinement using the same physical principles if we specify that space is flat in bulk solution but curves under confinement. However, curvature is not enough, a potential field must also be specified (the role of gravity in the example above). In solution, the general potential field expresses zero effective force as anti-symmetrical potentials cancel each other out. If within the space there exists a volume element in which potentials do not cancel, then particle geodesics would converge at that site in a manner equivalent to acceleration, observable as particle accumulation and compression. A non-zero potential field is therefore congruous to spatial curvature: the concentration of energy is proportional to the local divergence from flat space. Prima facie, this presents a physical analogy to Einstein's field equations for general relativity<sup>144</sup>:

$$R_{\alpha\beta} - \frac{1}{2}g_{\alpha\beta}R + \Lambda g_{\alpha\beta} = -\frac{8\pi G}{c^2}T_{\alpha\beta} \quad [5.3.4]$$

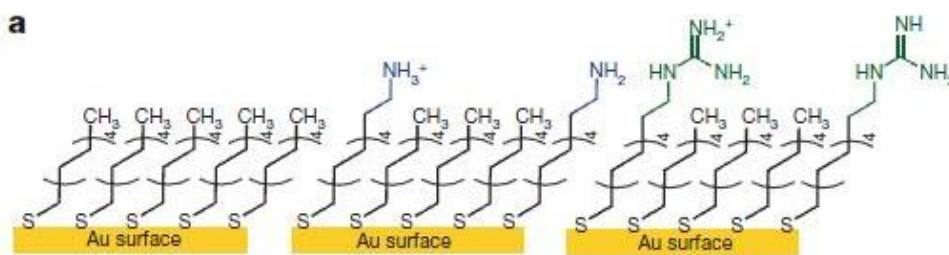
where the left hand side describes the curvature of the space according to the Ricci tensor  $R_{\alpha\beta}$ , scalar curvature  $R$ , metric tensor  $g_{\alpha\beta}$  and the cosmological constant  $\Lambda$  and the right hand side describes the concentration of energy by the stress-energy tensor  $T_{\alpha\beta}$ . Just as Einstein's equivalence principle states that there is no locally observable difference between an elevator car at rest Earth and one accelerating through empty space at  $9.8 \text{ m}\cdot\text{s}^{-2}$ , there is no local difference from the particle's perspective between following an adiabatic path in curved space and responding to externally applied pressure in equilibrium.

Classical thermodynamics are dependent on the same condition of zero net energy change that we demanded of our system, yet by also allowing for curvature of space we can incorporate effective acceleration through the distortion of geodesic lines from the Euclidean. It is therefore expected that a new general theory of thermodynamics could account for non-equilibrium systems and would reduce to the familiar equations of equilibrium thermodynamics at the zero net energy/zero curvature limit.

## 5.4 Application to experiment

If a geometric theory of thermodynamics accurately describes the confinement effect, it should be equally applicable to other non-polar molecules as it is to pyrrole. Furthermore larger non-polar molecules and polymers should also be subject to confinement effects. A self-assembled monolayer could therefore experience geodesic curvature as an attraction between its polymer tails in proportion to the charge concentration on its polar head.

This is exactly the result of a recent experimental measurement of the strength of hydrophobic interactions according to head group<sup>145</sup>. Placing a charge on the amine group by protonation (Figure 58, centre) doubled the hydrophobic attractive force from  $0.8 \pm 0.2 \text{ nN}$  to  $1.9 \pm 0.2 \text{ nN}$ . Replacing the head group with guanidinium (Figure 58, right) negated hydrophobic attraction. The study used a mixed solution of water and methanol because methanol is known to disrupt the structure of water near non-polar surfaces and decrease hydrophobic interactions<sup>146,147</sup>. While that paper did not suggest a reason why a more concentrated charge would strengthen hydrophobic interaction while a diffuse charge would eliminate it, it is an expected result of both the molecular and continuum theories outlined above.



**Fig. 58** The presence of an immobilized ion affects the compression of nearby non-polar polymers. The concentrated charge (centre) doubled the effect while a delocalized charge (right) negated it. (Reproduced from Ref. 145).

## 5.5 Conclusion

Water is susceptible to extreme phase changes near amphiphilic surfaces in a way that may be rare among solvents. The solubility of organic molecules and miscibility of gases in supercritical water eliminates the need for special solvents and solves the interphase transport problem but is currently difficult to exploit due to the extreme pressure and temperature necessary to maintain that bulk phase. Considering that biological nanoreactors surround nanoscale hydrophobic interior spaces with water soluble charged groups, biomolecular chemical reactors may control the local phase of water by the mechanisms described above to make energetically unfavourable reactions feasible, which would explain why all the processes of life are aqueous.

Molecular dynamics simulation is a promising method to study these systems. Cavity distribution statistics may reveal critical properties of confined water including solvation free energy, compressibility, changes in dielectric constant, potential energy of cavity formation and collapse, and the trajectories of non-polar solutes. This approach is limited by its requirement for a large number of computations to provide the statistical data necessary for quantitative calculations that would need to be repeated for each specific system. A geometric correction to classical thermodynamics would potentially permit analytical solutions for nanoscale, non-equilibrium systems.

These developments could lead to important advancements in chemistry, physics, and biology. By using geometric arguments to correct the assumptions that underlie existing methods, protein folding and drug interaction models could be vastly improved. Nanomaterial applications could open routes for biomimetic control over reactions common in nature but difficult for industry such as nitrogen and carbon dioxide fixing. Once the system of differential equations and proportionality constants are fully derived, this new general theory of thermodynamics has the potential to become a powerful tool for understanding far from equilibrium natural processes.

## 6 Conclusion and outlook

It is only recently that we have developed the tools needed to probe the structures and mechanisms of biological nanosystems tailored over millions of years of evolutionary optimization. Soft, responsive polymeric nanoarchitectures are well suited to adapt the lessons of nature to improve processes in medicine, science, and technology. Inherently conductive polymer fibre networks and hydrogels are able to model the extracellular matrix and cytosol. Self-assembling systems can create confined environments that improve the catalytic efficiency of enzymes or indeed mimic confinement within enzymes themselves.

Yet this project demonstrates that changes to reaction dynamics within nanoreactor confinement spaces are not merely catalytic – thermodynamic as well as kinetic properties are affected. This is a fundamentally new approach to the control of chemical reactivity. The reduction of platinum and gold chlorides are not energetically favoured reactions and normally require strong reducing agents to proceed; the salts' interaction with the amphiphilic co-polymer nanostructures described here remove that requirement to spontaneously produce monodisperse platinum nanocrystals or atomically thin sheets of crystalline gold. Likewise the spontaneous compression and polymerization of pyrrole indicates that these nanoreactors not only reduce the activation energy but reverse the favourability of the reaction.

Nanoreactors have the potential to replicate processes that are currently limited to high pressure and temperature reactors and so make such high energy, high capital, and high risk facilities obsolete. Iron catalyzed nitrogen fixing, for example, is accomplished within both large Haber process reactors and nanoscale nitrogenase enzymes. With the scale of the former and the efficiency of the latter it may be possible to meet global ammonia demand at a fraction of the current cost.

This research program should continue to develop along two fronts: the expansion of empirical reaction results and the development of a thermodynamic theory of confinement. Obvious candidate reactions for future nanoreactor experiments include the reduction of other metal salts and other polymerizations. The use of organic solvents could be greatly reduced if common organic processes such as the Diels-Alder reaction could be performed in water soluble nanoreactors. Also, experiments on reaction processes requiring high temperature or pressure to overcome thermodynamic barriers, such as Haber nitrogen fixation or Fischer-Tropsch carbon fixation, would produce high value results if successful. Finally, multiphase reactions and heterogeneous catalysis would benefit from the gas-liquid miscibility expected to exist within the nanoreactor's supercritical interior.



The presence of a polarizing charge next to a hydrophobic region seems to produce a standing potential energy field that produces a metastable, supercritical phase of water between the confinement surfaces. Current molecular dynamics models may be used to estimate some thermodynamic properties of confined spaces. Simulations currently underway will provide insight into the mechanisms of confined reactivity, although this method is limited by its inability to break and form bonds and by the need for long computation times. Generalization of the thermodynamic equations may make it possible to perform analytic calculation of the same processes by accounting for curvature of molecular geodesic pathways. Behaviours responsible for uniform pressure, temperature, and entropy distribution under equilibrium conditions would instead drive compression, temperature discontinuity, and increased organization within the high potential energy volume. These actions may be definable through a geometric correction to the Euclidean space assumed by current models. Incorporation of such a correction has the potential of producing a more general theory of thermodynamics and a powerful tool for understanding the assembly and activity of both biological proteins and biomimetic nanoreactors. Theoretical results could be validated by the concurrent growth of empirical data provided by the experimental systems while the advancement of theory could indicate new paths for experiment, reinforcing the complementarity of the two approaches.

Lastly, this work has shown that all previous reaction experiments occurred under 1-dimensional confinement in either SMA or IMA bi-layers. It appears probable that the nanostructure morphology of SMA may be tunable by control of the molecular weight of the polymer chains. The effect of dimensionality on confinement nanoreactors remains an open question and an important area for future work. Also, the analogous discovery of the tunable morphology of block co-polymers incited a growth of interest and the development of new nanofabrication techniques. It is expected that this work could likewise expand the field for alternating co-polymers.

Biomimetic polymer-metal nanoreactors are an important area for research, one which could impact applications as diverse as energy collection, storage, and use, toxic chemical remediation, and fine synthesis including pharmaceuticals. The possibility of closing the industrial carbon cycle for long-term energy security and climate management is alone enough to motivate development of the field. True artificial enzymes incorporating the selectivity, reaction rate, and regulatory functions of the naturally produced variety may remain out of reach, but the simple systems presented hold tremendous promise for the future of our economy and ecology.

## 7 Consolidated references

1. Whitesides, G. M., Mathias, J. P. & Seto, C. T. Molecular self-assembly and nanochemistry: a chemical strategy for the synthesis of nanostructures. *Science* **254**, 1312–1319 (1991).
2. Wendell, D. W., Patti, J. & Montemagno, C. D. Using biological inspiration to engineer functional nanostructured materials. in *Small* **2**, 1324–1329 (2006).
3. Raynal, M., Ballester, P., Vidal-Ferran, A. & van Leeuwen, P. W. N. M. Supramolecular catalysis. Part 2: artificial enzyme mimics. *Chem. Soc. Rev.* **43**, 1734–87 (2014).
4. Aida, T., Meijer, E. W. & Stupp, S. I. Functional Supramolecular Polymers. *Science* **335**, 813–817 (2012).
5. Kumar, D. & Sharma, R. C. Advances in conductive polymers. *European Polymer Journal* **34**, 1053–1060 (1998).
6. Guo, B., Glavas, L. & Albertsson, A.-C. Biodegradable and electrically conducting polymers for biomedical applications. *Prog. Polym. Sci.* **38**, 1263–1286 (2013).
7. Tyler McQuade, D., Pullen, A. E. & Swager, T. M. Conjugated polymer-based chemical sensors. *Chem. Rev.* **100**, 2537–2574 (2000).
8. Tokarev, I. & Minko, S. Multiresponsive, Hierarchically Structured Membranes: New, Challenging, Biomimetic Materials for Biosensors, Controlled Release, Biochemical Gates, and Nanoreactors. *Adv. Mater.* **21**, 241–247 (2009).
9. Lehn, J.-M. Toward complex matter: supramolecular chemistry and self-organization. *Proc. Natl. Acad. Sci. U. S. A.* **99**, 4763–4768 (2002).
10. Israelachvili, J. N., Mitchell, D. J. & Ninham, B. W. Theory of self-assembly of lipid bilayers and vesicles. *Biochim. Biophys. Acta* **470**, 185–201 (1977).
11. Guimard, N. K., Gomez, N. & Schmidt, C. E. Conducting polymers in biomedical engineering. *Progress in Polymer Science* **32**, 876–921 (2007).

12. Fonner, J. M. *et al.*. Biocompatibility implications of polypyrrole synthesis techniques. *Biomed. Mater.* **3**, 034124 (2008).
13. Lee, J. Y., Bashur, C. A., Goldstein, A. S. & Schmidt, C. E. Polypyrrole-coated electrospun PLGA nanofibers for neural tissue applications. *Biomaterials* **30**, 4325–4335 (2009).
14. Lehn, J. M. Dynamers: Dynamic molecular and supramolecular polymers. *Australian Journal of Chemistry* **63**, 611–623 (2010).
15. Jones, D. M., Smith, J. R., Huck, W. T. S. & Alexander, C. Variable adhesion of micropatterned thermoresponsive polymer brushes: AFM investigations of Poly(N-isopropylacrylamide) brushes prepared by surface-initiated polymerizations. *Adv. Mater.* **14**, 1130–1134 (2002).
16. Gabai, R. *et al.*. Characterization of the Swelling of Acrylamidophenylboronic Acid–Acrylamide Hydrogels upon Interaction with Glucose by Faradaic Impedance Spectroscopy, Chronopotentiometry, Quartz-Crystal Microbalance (QCM), and Surface Plasmon Resonance (SPR) Experiments. *J. Phys. Chem. B* **105**, 8196–8202 (2001).
17. Discher, D. E. & Eisenberg, A. Polymer vesicles. *Science* **297**, 967–973 (2002).
18. Lin, L., Yan, J. & Li, J. Small-molecule triggered cascade enzymatic catalysis in hour-glass shaped nanochannel reactor for glucose monitoring. *Anal. Chem.* **86**, 10546–51 (2014).
19. Minten, I. J. *et al.*. Catalytic capsids: the art of confinement. *Chem. Sci.* **2**, 358 (2011).
20. Wang, Q., Li, L. & Xu, B. Bioinspired supramolecular confinement of luminol and heme proteins to enhance the chemiluminescent quantum yield. *Chemistry* **15**, 3168–72 (2009).
21. Smitha, B., Sridhar, S. & Khan, A. A. Solid polymer electrolyte membranes for fuel cell applications—a review. *Journal of Membrane Science* **259**, 10–26 (2005).
22. Kudo, A. & Miseki, Y. Heterogeneous photocatalyst materials for water splitting. *Chem. Soc. Rev.* **38**, 253–278 (2009).
23. McEvoy, J. P. & Brudvig, G. W. Water-splitting chemistry of photosystem II. *Chemical Reviews* **106**, 4455–4483 (2006).

24. Kim, J. H., Lee, M., Lee, J. S. & Park, C. B. Self-assembled light-harvesting peptide nanotubes for mimicking natural photosynthesis. *Angew. Chemie - Int. Ed.* **51**, 517–520 (2012).
25. Benkovic, S. J. & Hammes-Schiffer, S. A perspective on enzyme catalysis. *Science* **301**, 1196–1202 (2003).
26. Eisenmesser, E. Z. *et al.* Intrinsic dynamics of an enzyme underlies catalysis. *Nature* **438**, 117–121 (2005).
27. Dong, Z., Luo, Q. & Liu, J. Artificial enzymes based on supramolecular scaffolds. *Chem. Soc. Rev.* **41**, 7890 (2012).
28. Koblenz, T. S., Wassenaar, J. & Reek, J. N. H. Reactivity within a confined self-assembled nanospace. *Chem. Soc. Rev.* **37**, 247–62 (2008).
29. Conn, M. M. & Rebek, J. Self-Assembling Capsules. *Chem. Rev.* **97**, 1647–1668 (1997).
30. Whitesides, G. M. & Grzybowski, B. Self-assembly at all scales. *Science* **295**, 2418–21 (2002).
31. Zhang, S. Fabrication of novel biomaterials through molecular self-assembly. *Nat. Biotechnol.* **21**, 1171–8 (2003).
32. Kirby, A. J. Enzyme Mechanisms, Models, and Mimics. *Angew. Chem. Int. Ed. Engl.* **35**, 706–724 (1996).
33. Li, M., Wong, K. K. W. & Mann, S. Organization of Inorganic Nanoparticles Using Biotin–Streptavidin Connectors. *Chem. Mater.* **11**, 23–26 (1999).
34. Okuda, M., Iwahori, K., Yamashita, I. & Yoshimura, H. Fabrication of nickel and chromium nanoparticles using the protein cage of apoferritin. *Biotechnol. Bioeng.* **84**, 187–194 (2003).
35. Lee, S., Gao, X. & Matsui, H. Biomimetic and Aggregation-Driven Crystallization Route for Room-Temperature Material Synthesis : Growth of -Ga<sub>2</sub>O<sub>3</sub> Nanoparticles on Peptide Assemblies as Nanoreactors. 2954–2958 (2007).

36. Izumi, Y. Recent advances in the photocatalytic conversion of carbon dioxide to fuels with water and/or hydrogen using solar energy and beyond. *Coord. Chem. Rev.* **257**, 171–186 (2013).
37. Kumar, B. *et al.*. Photochemical and photoelectrochemical reduction of CO<sub>2</sub>. *Annu. Rev. Phys. Chem.* **63**, 541–69 (2012).
38. Barton, E. E., Rampulla, D. M. & Bocarsly, A. B. Selective solar-driven reduction of CO<sub>2</sub> to methanol using a catalyzed p-GaP based photoelectrochemical cell. *J. Am. Chem. Soc.* **130**, 6342–6344 (2008).
39. Lim, C.-H., Holder, A. M., Hynes, J. T. & Musgrave, C. B. Reduction of CO<sub>2</sub> to Methanol Catalyzed by a Biomimetic Organo-Hydride Produced from Pyridine. *J. Am. Chem. Soc.* **136**, 16081–16095 (2014).
40. Malardier-Jugroot, C., van de Ven, T. G. M. & Whitehead, M. a. Characterization of a novel self-association of an alternating copolymer into nanotubes in solution. *Mol. Simul.* **31**, 173–178 (2005).
41. Garnier, G., Duskova-Smrckova, M., Vyhalkova, R., Van De Ven, T. G. M. & Revol, J. F. Association in solution and adsorption at an air-water interface of alternating copolymers of maleic anhydride and styrene. *Langmuir* **16**, 3757–3763 (2000).
42. Malardier-Jugroot, C., Van De Ven, T. G. M., Cosgrove, T., Richardson, R. M. & Whitehead, M. a. Novel self-assembly of amphiphilic copolymers into nanotubes: Characterization by small-angle neutron scattering. *Langmuir* **21**, 10179–10187 (2005).
43. Chan, A. S. W., Groves, M. & Malardier-Jugroot, C. Self-assembly of alternating copolymers and the role of hydrophobic interactions: characterisation by molecular modelling. *Mol. Simul.* **37**, 701–709 (2011).
44. Li, X. & Malardier-Jugroot, C. Confinement effect in the synthesis of polypyrrole within polymeric templates in aqueous environments. *Macromolecules* **46**, 2258–2266 (2013).
45. Groves, M. N., Malardier-jugroot, C. & Jugroot, M. Environmentally friendly synthesis of supportless Pt based nanoreactors in aqueous solution. *Chem. Phys. Lett.* **612**, 309–312 (2014).

46. Planck, M. Ueber das Gesetz der Energieverteilung im Normalspectrum. *Ann. Phys.* **309**, 553–563 (1901).
47. Einstein, A. Über einen die Erzeugung und Verwandlung des Lichtes betreffenden heuristischen Gesichtspunkt. *Ann. Phys.* **322**, 132–148 (1905).
48. De Broglie, L. Recherches sur la théorie des quanta. *Ann. la Fond. Louis Broglie* **17**, (1992).
49. Schrödinger, E. Quantisierung als Eigenwertproblem. *Ann. Phys.* **385**, 437–490 (1926).
50. Born, M. Quantenmechanik der Stoßvorgänge. *Zeitschrift für Phys.* **38**, 803–827 (1926).
51. Slater, J. C. Note on Hartree's Method. *Phys. Rev.* **35**, 210–211 (1930).
52. Ramachandran, K. I., Deepa, G. & Namboori P.K., K. *Computational Chemistry and Molecular Modeling*. (Springer Berlin Heidelberg, 2008). doi:10.1007/978-3-540-77304-7
53. Lowe, J. P. & Peterson, K. A. *Quantum chemistry. QMBook* (2006). at <[http://courses.chem.psu.edu/chem408/reading/old/ME\\_atoms\\_Levine\\_11.pdf](http://courses.chem.psu.edu/chem408/reading/old/ME_atoms_Levine_11.pdf)>
54. Hehre, W. J., Radom, L., Schleyer, P. V. R. & Pople, J. A. *Ab Initio Molecular Orbital Theory. Accounts of Chemical Research* **9**, (1986).
55. Hartree, D. R. The Wave Mechanics of an Atom with a Non-Coulomb Central Field. Part I. Theory and Methods. *Math. Proc. Cambridge Philos. Soc.* **24**, 89 (1928).
56. Fock, V. Näherungsmethode zur Lösung des quantenmechanischen Mehrkörperproblems. *Zeitschrift für Phys.* **61**, 126–148 (1930).
57. McWeeny, R. *Methods of Molecular Quantum Mechanics*. (Academic Press, 1992).
58. Parr, R. G. & Yang, W. *Density-Functional Theory of Atoms and Molecules. International Journal of Quantum Chemistry* **16**, (1989).
59. Thomas, L. H. The calculation of atomic fields. *Mathematical Proceedings of the Cambridge Philosophical Society* **23**, 542 (1927).

60. Fermi, E. Eine statistische Methode zur Bestimmung einiger Eigenschaften des Atoms und ihre Anwendung auf die Theorie des periodischen Systems der Elemente. *Zeitschrift für Phys.* **48**, 73–79 (1928).
61. Hohenberg, P. & Kohn, W. Inhomogeneous Electron Gas. *Phys. Rev.* **136**, B864–B871 (1964).
62. Kohn, W. & Sham, L. J. Self-consistent equations including exchange and correlation effects. *Phys. Rev.* **140**, (1965).
63. M. J. Frisch, G. W. Trucks, H. B. Schlegel, G. E. Scuseria, M. A. Robb, J. R. Cheeseman, J. A. Montgomery Jr., T. Vreven, K. N. Kudin, J. C. Burant, J.M.Millam, S. S. Iyengar, J. Tomasi, V. Barone, B. Mennucci, M. Cossi, G. Scalmani, N. Rega, G. A. Peters, C. G. and J. A. P. GAUSSIAN 09 (Revision B.02). *Gaussian, Inc., Wallingford CT* (2009).
64. Becke, A. & Becke, A. Density Functional Thermochemistry III The Role of Exact Exchange. *J. Chem. Phys.* **98**, 5648–5652 (1993).
65. Lee, C., Yang, W. & Parr, R. G. Development of the Colle-Salvetti correlation-energy formula into a functional of the electron density. *Phys. Rev. B* **37**, 785–789 (1988).
66. Paier, J., Marsman, M. & Kresse, G. Why does the B3LYP hybrid functional fail for metals? *J. Chem. Phys.* **127**, 1–11 (2007).
67. Hehre, W. J., Ditchfield, R. & Pople, J. A. Self—Consistent Molecular Orbital Methods. XII. Further Extensions of Gaussian—Type Basis Sets for Use in Molecular Orbital Studies of Organic Molecules. *J. Chem. Phys.* **56**, 2257–2261 (1972).
68. Hay, P. J. & Wadt, W. R. Ab initio effective core potentials for molecular calculations. Potentials for K to Au including the outermost core orbitals. *J. Chem. Phys.* **82**, 299 (1985).
69. Perdew, J. P. & Yue, W. Accurate and simple density functional for the electronic exchange energy: Generalized gradient approximation. *Phys. Rev. B* **33**, 8800–8802 (1986).
70. Kryachko, E. S., Arbuznikov, A. V. & Hendrickx, M. F. A. Modeling Chemisorption of Benzene and Its Hydrogenation on Platinum Surfaces. 1.

- Complexes of Benzene with Pt and Pt 2. *J. Phys. Chem. B* **105**, 3557–3566 (2001).
71. Beer, A. Bestimmung der Absorption des rothen Lichts in farbigen Flüssigkeiten. *Ann. der Phys. und Chemie* **162**, 78–88 (1852).
  72. Haiss, W., Thanh, N. T. K., Aveyard, J. & Fernig, D. G. Determination of Size and Concentration of Gold Nanoparticles from UV - Vis Spectra. **79**, 4215–4221 (2007).
  73. Higgins, J. S. & Benoit, H. *Polymers and Neutron Scattering*. (Clarendon Press, 1994).
  74. Sears, V. F. Neutron scattering lengths and cross sections. *Neutron News* **3**, 26–37 (1992).
  75. Hammouda, B. Introduction to Neutron Scattering. 16 (2012). at <[https://www.ncnr.nist.gov/programs/sans/pdf/part\\_i\\_introduction\\_to\\_neutron\\_scattering.pdf](https://www.ncnr.nist.gov/programs/sans/pdf/part_i_introduction_to_neutron_scattering.pdf)>
  76. Technology, N. I. of S. and. NGB 30m SANS - Small Angle Neutron Scattering. (2015). at <<http://www.nist.gov/ncnr/ng3-sans-small-angle-neutron-scattering.cfm>>
  77. Kline, S. R. Reduction and analysis of SANS and USANS data using IGOR Pro. *J. Appl. Crystallogr.* **39**, 895–900 (2006).
  78. Feigin, L. A. & Svergun, D. I. *Structure Analysis by Small-Angle X-Ray and Neutron Scattering*. (Springer US, 1987). doi:10.1007/978-1-4757-6624-0
  79. Bergström, M., Pedersen, J. S., Schurtenberger, P. & Egelhaaf, S. U. Small-Angle Neutron Scattering (SANS) Study of Vesicles and Lamellar Sheets Formed from Mixtures of an Anionic and a Cationic Surfactant. *J. Phys. Chem. B* **103**, 9888–9897 (1999).
  80. Murr, L. E. *Electron and ion microscopy and microanalysis : principles and applications*. (Marcel Dekker Inc, 1982).
  81. Cliff, G. & Lorimer, G. W. The quantitative analysis of thin specimens. *J. Microsc.* **103**, 203–207 (1975).



82. Reimer, L. *Transmission Electron Microscopy*. **36**, (Springer Berlin Heidelberg, 1984).
83. Müllner, M. *et al.*. Template-directed mild synthesis of anatase hybrid nanotubes within cylindrical core-shell-corona polymer brushes. *Macromolecules* **45**, 6981–6988 (2012).
84. Sebakhy, K. O., Kessel, S. & Monteiro, M. J. Nanoreactors to Synthesize Well-defined Polymer Nanoparticles: Decoupling Particle Size from Molecular Weight. *Macromolecules* **43**, 9598–9600 (2010).
85. Ahmed, S. R. & Kofinas, P. Controlled Room Temperature Synthesis of CoFe<sub>2</sub>O<sub>4</sub> Nanoparticles through a Block Copolymer Nanoreactor Route. *Macromolecules* **35**, 3338–3341 (2002).
86. Vriezema, D. M. *et al.*. Self-assembled nanoreactors. *Chemical Reviews* **105**, 1445–1489 (2005).
87. Arnold, F. H. Design by Directed Evolution. *Acc. Chem. Res.* **31**, 125–131 (1998).
88. Kang, J. & Rebek, J. Acceleration of a Diels–Alder reaction by a self-assembled molecular capsule. *Nature* **385**, 50–52 (1997).
89. Luthi, A. J. *et al.*. Tailoring of Biomimetic High-Density Lipoprotein Nanostructures Changes Cholesterol Binding and Efflux. *ACS Nano* **6**, 276–285 (2012).
90. Kirby, A. J. & Hollfelder, F. in *From Enzyme Models to Model Enzymes* 1–28 (RSC Publishing, 2009).
91. Zhang, X. & Houk, K. N. Why enzymes are proficient catalysts: beyond the Pauling paradigm. *Acc. Chem. Res.* **38**, 379–85 (2005).
92. Malardier-Jugroot, C., Van De Ven, T. G. M. & Whitehead, M. a. Linear conformation of poly(styrene-alt-maleic anhydride) capable of self-assembly: A result of chain stiffening by internal hydrogen bonds. *J. Phys. Chem. B* **109**, 7022–7032 (2005).
93. Ray, J. G., Johnson, A. J. & Savin, D. A. Self-assembly and responsiveness of polypeptide-based block copolymers: How ‘smart’ behavior and topological

- complexity yield unique assembly in aqueous media. *J. Polym. Sci. Part B Polym. Phys.* **51**, 508–523 (2013).
94. Vyhalkova, R., Xiao, L., Yang, G. & Eisenberg, A. Spherical Blackberry-type Capsules Containing Block Copolymer Aggregates. *Langmuir* **30**, 2188–2195 (2014).
  95. Svensson, M. *et al.*. ONIOM: A Multilayered Integrated MO + MM Method for Geometry Optimizations and Single Point Energy Predictions. A Test for Diels–Alder Reactions and Pt(P(t-Bu)<sub>3</sub>)<sub>2</sub> + H<sub>2</sub> Oxidative Addition. *J. Phys. Chem.* **100**, 19357–19363 (1996).
  96. Stewart, J. J. P. Optimization of parameters for semiempirical methods V: Modification of NDDO approximations and application to 70 elements. *J. Mol. Model.* **13**, 1173–1213 (2007).
  97. Perdew, J. P. *et al.*. Atoms, Molecules, Solids, and Surfaces - Applications of the Generalized Gradient Approximation For Exchange and Correlation (vol 46, Pg 6671, 1992). *Phys. Rev. B* **46**, 6671–6687 (1992).
  98. Perdew, J. P. & Wang, Y. Accurate and simple analytic representation of the electron-gas correlation energy. *Phys. Rev. B* **45**, 13244–13249 (1992).
  99. Li, T. & Balbuena, P. B. Computational Studies of the Interactions of Oxygen with Platinum Clusters. *J. Phys. Chem. B* **105**, 9943–9952 (2001).
  100. Shore, T. C., Mith, D., DePrekel, D., McNall, S. & Ge, Y. A B3LYP study on the C–H activation in propane by neutral and +1 charged low-energy platinum clusters with 2–6 atoms. *React. Kinet. Mech. Catal.* **109**, 315–333 (2013).
  101. Ruan, L. *et al.*. A Rational Biomimetic Approach to Structure Defect Generation in Colloidal Nanocrystals. *ACS Nano* **8**, 6934–6944 (2014).
  102. Deng, Q. Y., Yang, B., Wang, J. F., Whiteley, C. G. & Wang, X. N. Biological synthesis of platinum nanoparticles with apoferritin. *Biotechnol. Lett.* **31**, 1505–9 (2009).
  103. Huang, J. *et al.*. Formation and characterization of water-soluble platinum nanoparticles using a unique approach based on the hydrosilylation reaction. *Langmuir* **20**, 5145–8 (2004).

104. Liu, Z., Ling, X. Y., Su, X. & Lee, J. Y. Carbon-Supported Pt and PtRu Nanoparticles as Catalysts for a Direct Methanol Fuel Cell. *J. Phys. Chem. B* **108**, 8234–8240 (2004).
105. Myers, R. H., Montgomery, D. C. & Anderson-Cook, C. *Response Surface Methodology: Process and Product Optimization Using Designed Experiments*. Wiley series in probability and statistics (2009). doi:10.2307/1270613
106. Fujita, T. *et al.* Atomic origins of the high catalytic activity of nanoporous gold. *Nat. Mater.* **11**, 775–780 (2012).
107. Qin, H. L. *et al.* Thickness-controlled synthesis of ultrathin Au sheets and surface plasmonic property. *J. Am. Chem. Soc.* **135**, 12544–7 (2013).
108. Huang, X. *et al.* Synthesis of hexagonal close-packed gold nanostructures. *Nat. Commun.* **2**, 292 (2011).
109. Huang, X. *et al.* Synthesis of hexagonal close-packed gold nanostructures. *Nat. Commun.* **2**, 292 (2011).
110. Ataee-Esfahani, H., Wang, L., Nemoto, Y. & Yamauchi, Y. Synthesis of Bimetallic Au@Pt Nanoparticles with Au Core and Nanostructured Pt Shell toward Highly Active Electrocatalysts. *Chem. Mater.* **22**, 6310–6318 (2010).
111. Vargas-Hernandez, C., Mariscal, M. M., Esparza, R. & Yacaman, M. J. A synthesis route of gold nanoparticles without using a reducing agent. *Appl. Phys. Lett.* **96**, 213115 (2010).
112. Shang, Y. *et al.* Synthesis of gold nanoparticles by reduction of H<sub>2</sub>AuCl<sub>4</sub> under UV irradiation. *Solid State Sci.* **15**, 17–23 (2013).
113. Wong, C. *et al.* Multistage nanoparticle delivery system for deep penetration into tumor tissue. *Proc. Natl. Acad. Sci. U. S. A.* **108**, 2426–2431 (2011).
114. Manjavacas, A. & Abajo, F. J. G. De. Tunable plasmons in atomically thin gold. 1–30
115. Toshima, N. & Yonezawa, T. Bimetallic nanoparticles—Novel materials for chemical and physical applications □. 1179–1201 (1998).
116. Bahram, M. *et al.* Synthesis of gold nanoparticles using pH-sensitive hydrogel and its application for colorimetric determination of acetaminophen, ascorbic

- acid and folic acid. *Colloids Surfaces A Physicochem. Eng. Asp.* **441**, 517–524 (2014).
117. Trick, J. L., Wallace, E. J., Bayley, H. & Sansom, M. S. P. Designing a Hydrophobic Barrier within Biomimetic Nanopores. *ACS Nano* **8**, 11268–11279 (2014).
  118. Johnson, M. E., Malardier-Jugroot, C., Murarka, R. K. & Head-Gordon, T. Hydration water dynamics near biological interfaces. *J. Phys. Chem. B* **113**, 4082–4092 (2009).
  119. Pal, S. K. & Zewail, A. H. Dynamics of water in biological recognition. *Chem. Rev.* **104**, 2099–2123 (2004).
  120. Malardier-Jugroot, C. & Head-Gordon, T. Separable cooperative and localized translational motions of water confined by a chemically heterogeneous environment. *Phys. Chem. Chem. Phys.* **9**, 1962–1971 (2007).
  121. Malardier-Jugroot, C., Johnson, M. E., Murarka, R. K. & Head-Gordon, T. Aqueous peptides as experimental models for hydration water dynamics near protein surfaces. *Phys Chem Chem Phys* **10**, 4903–4908 (2008).
  122. Patel, a J. Fluctuations of Water near Extended Hydrophobic and Hydrophilic Surfaces. *J. Phys. Chem. B* 1632–1637 (2010).
  123. McTaggart, M., Malardier-jugroot, C. & Jugroot, M. Self-assembled biomimetic nanoreactors I: Polymeric template. *Chem. Phys. Lett.* **636**, 216–220 (2015).
  124. Lynden-Bell, R. M. & Debenedetti, P. G. Computational investigation of order, structure, and dynamics in modified water models. *J. Phys. Chem. B* (2005). doi:10.1021/jp0458553
  125. Bergman, D. L. & Lynden-Bell, R. M. Is the hydrophobic effect unique to water? The relation between solvation properties and network structure in water and modified water models. *Molecular Physics* (2001). doi:10.1080/00268970110041632
  126. Berne, B. J., Weeks, J. D. & Zhou, R. Dewetting and hydrophobic interaction in physical and biological systems. *Annu. Rev. Phys. Chem.* (2009). doi:10.1146/annurev.physchem.58.032806.104445

127. Huang, X., Margulis, C. J. & Berne, B. J. Dewetting-induced collapse of hydrophobic particles. *Proc. Natl. Acad. Sci. U. S. A.* (2003). doi:10.1073/pnas.1934837100
128. Lum, K., Chandler, D. & Weeks, J. D. Hydrophobicity at Small and Large Length Scales. *J. Phys. Chem. B* (1999). doi:10.1021/jp984327m
129. Patel, A. J., Varilly, P. & Chandler, D. Fluctuations of water near extended hydrophobic and hydrophilic surfaces. *J. Phys. Chem. B* **114**, 1632–1637 (2010).
130. Giovambattista, N., Rosky, P. J. & Debenedetti, P. G. Computational Studies of Pressure, Temperature, and Surface Effects on the Structure and Thermodynamics of Confined Water. *Annual Review of Physical Chemistry* (2012). doi:10.1146/annurev-physchem-032811-112007
131. Lynden-bell, R. M. & Head-gordon, T. Solvation in modified water models: towards understanding hydrophobic effects. *Molecular Physics* (2006). doi:10.1080/00268970601022727
132. Leung, K., Luzar, A. & Bratko, D. Dynamics of capillary drying in water. *Phys. Rev. Lett.* (2003). doi:10.1103/PhysRevLett.90.065502
133. Luzar, A. & Leung, K. Dynamics of capillary evaporation. I. Effect of morphology of hydrophobic surfaces. *J. Chem. Phys.* (2000). doi:10.1063/1.1290478
134. Leung, K. & Luzar, A. Dynamics of capillary evaporation. II. Free energy barriers. *J. Chem. Phys.* (2000). doi:10.1063/1.1290479
135. Lynden-Bell, R. M., Giovambattista, N., Debenedetti, P. G., Head-Gordon, T. & Rosky, P. J. Hydrogen bond strength and network structure effects on hydration of non-polar molecules. *Phys. Chem. Chem. Phys.* (2011). doi:10.1039/c0cp01701a
136. Head-Gordon, T. & Rick, S. W. Consequences of chain networks on thermodynamic, dielectric and structural properties for liquid water. *Phys. Chem. Chem. Phys.* (2007). doi:10.1039/b614742a
137. Luzar, A. Activation barrier scaling for the spontaneous evaporation of confined water. *J. Phys. Chem. B* (2004). doi:10.1021/jp0470703

138. Daub, C. D., Bratko, D. & Luzar, A. Nanoscale wetting under electric field from molecular simulations. *Top. Curr. Chem.* (2012). doi:10.1007/128-2011\_188
139. Vanzo, D., Bratko, D. & Luzar, A. Dynamic Control of Nanopore Wetting in Water and Saline Solutions under an Electric Field. doi:10.1021/jp506389p
140. McTaggart, M., Malardier-jugroot, C. & Jugroot, M. Self-assembled biomimetic nanoreactors II : Noble metal active centres *Chem. Phys. Lett.* **636**, 220-227 (2015).
141. Craig, V. S. J. Very small bubbles at surfaces—the nanobubble puzzle. *Soft Matter* **7**, 40–48 (2011).
142. Hayashi, H. & Hakuta, Y. Hydrothermal Synthesis of metal oxide nanoparticles in supercritical water. *Materials (Basel)*. **3**, 3794–3817 (2010).
143. Luzar, A. & Bratko, D. Gas Solubility in Hydrophobic Confinement. *J. Phys. Chem. B* **109**, 22545–22552 (2005).
144. Wald, R. M. *General relativity*. (University of Chicago press, 2010).
145. Ma, C. D., Wang, C., Acevedo-Vélez, C., Gellman, S. H. & Abbott, N. L. Modulation of hydrophobic interactions by proximally immobilized ions. *Nature* (2015). doi:10.1038/nature14018
146. Wang, J., Li, Z., Yoon, R.-H. & Eriksson, J. C. Surface forces in thin liquid films of n-alcohols and of water--ethanol mixtures confined between hydrophobic surfaces. *J. Colloid Interface Sci.* **379**, 114–120 (2012).
147. Hwang, S., Shao, Q., Williams, H., Hilty, C. & Gao, Y. Q. Methanol strengthens hydrogen bonds and weakens hydrophobic interactions in proteins--a combined molecular dynamics and NMR study. *J. Phys. Chem. B* **115**, 6653–6660 (2011).